

# Experimental Determination of Residual Stresses in Roll Expanded Joints in CANDU<sup>®</sup> Nuclear Reactors

by

**William J. Paley**

BASc., The University of British Columbia

A thesis submitted to the Faculty of Graduate and Postdoctoral Affairs in partial fulfillment of  
the requirements for the degree of

**Master of Applied Science**

in

**Mechanical Engineering**

Carleton University

Ottawa, Ontario

December 14, 2012

© Copyright

2012 - William J. Paley



Library and Archives  
Canada

Published Heritage  
Branch

395 Wellington Street  
Ottawa ON K1A 0N4  
Canada

Bibliothèque et  
Archives Canada

Direction du  
Patrimoine de l'édition

395, rue Wellington  
Ottawa ON K1A 0N4  
Canada

*Your file Votre référence*

*ISBN: 978-0-494-94275-8*

*Our file Notre référence*

*ISBN: 978-0-494-94275-8*

#### NOTICE:

The author has granted a non-exclusive license allowing Library and Archives Canada to reproduce, publish, archive, preserve, conserve, communicate to the public by telecommunication or on the Internet, loan, distribute and sell theses worldwide, for commercial or non-commercial purposes, in microform, paper, electronic and/or any other formats.

The author retains copyright ownership and moral rights in this thesis. Neither the thesis nor substantial extracts from it may be printed or otherwise reproduced without the author's permission.

#### AVIS:

L'auteur a accordé une licence non exclusive permettant à la Bibliothèque et Archives Canada de reproduire, publier, archiver, sauvegarder, conserver, transmettre au public par télécommunication ou par l'Internet, prêter, distribuer et vendre des thèses partout dans le monde, à des fins commerciales ou autres, sur support microforme, papier, électronique et/ou autres formats.

L'auteur conserve la propriété du droit d'auteur et des droits moraux qui protègent cette thèse. Ni la thèse ni des extraits substantiels de celle-ci ne doivent être imprimés ou autrement reproduits sans son autorisation.

---

In compliance with the Canadian Privacy Act some supporting forms may have been removed from this thesis.

While these forms may be included in the document page count, their removal does not represent any loss of content from the thesis.

Conformément à la loi canadienne sur la protection de la vie privée, quelques formulaires secondaires ont été enlevés de cette thèse.

Bien que ces formulaires aient inclus dans la pagination, il n'y aura aucun contenu manquant.

Canada

## **Abstract**

This thesis describes work undertaken to further the understanding of mechanically roll expanded joints in CANDU® nuclear reactor fuel channels. The residual stresses developed in the joints were investigated through experimental strain measurement during dismantling of joints of 6 and 10 mm walled tubes rolled over a range of wall reductions. Stresses in the rolled joint were calculated from the measured strains using the crack compliance method. A secondary objective was to evaluate the suitability of the crack compliance technique to predict stresses in rolled joints.

The wall thickness was found to have a larger effect on the stress state of the tube than did the amount of wall reduction. The crack compliance technique was found to be a useful tool to determine the residual stress distribution of tubes in mechanical roll expanded joints however the complexity of the technique prohibits application to many common problems.

## **Acknowledgements**

First and foremost I would like to thank my employer Atomic Energy of Canada Limited (AECL) for making it possible for me to pursue this degree. In particular, completion of this would not have been possible without the support and advice of my manager Dr. Gina Strati. I would also like to thank my thesis supervisors Dr. Robert Bell, and Dr. Xin Wang, and my section head and engineering mentor Dave Poff, P.Eng. I would also like to thank my colleague and friend Nick Simpson for his feedback and encouragement.

There are many others who have helped me along the way. To name a few: Carleton Ph.D. candidate Michael Bach, as well as Mike Banks, Howie Jessup, and Rob Steele in the Mechanical Equipment Development branch at AECL, Dr. Yingke Han in the Inspection Monitoring and Dynamics branch at AECL, Dr. Bill Diamond, and Dr. Metin Yetisir of the Fluid Sealing Technology branch at AECL, as well as the AECL Manufacturing Services.

## **Acronyms and Abbreviations**

2D	Two dimensional
3D	Three dimensional.
ACR	Advanced CANDU® Reactor
AECL	Atomic Energy of Canada Limited
AGS	Annulus Gas System
ANSYS	Commercially available Finite element software package
APDL	ANSYS® Parametric Design Language
CANDU® 6, C6	CANada Deuterium Uranium – 600 MWe reactor size
CRL	Chalk River Laboratories
CT	Calandria Tube
Gen-IV	Generation 4
ID	Inside Diameter
EC6	Enhanced CANDU® 600MW
EF	End Fitting
HCP	Hexagonal Close Packed
OD	Outside Diameter
PT	Pressure Tube
SHCS	Socket Head Cap Screws
TS	Tubesheet Plate
WEDM	Wire Electrical Discharge Machining
WR	Wall Reduction
YSZ	Yttria Stabilized Zirconia

## List of Symbols

$A$	Coefficient Vector
$b$	Substitution variable
$C$	Compliance matrix
$D$	Diameter [mm]
$D_{RI}$	Rolled-in tube diameter [mm]
$D_{TS}$	Diameter of as-machined tubesheet [mm]
$E$	Young's modulus [GPa]
$F$	Force (with no subscript)
$F_{()}$	Substitution variable (with subscript)
$G$	Shear Modulus [GPa]
$i$	Index variable
$j$	Index variable
$l$	Tube length
$LT$	Substitution variable
$n$	Index variable
$P_{()}$	Polynomial, order indicated by subscript
$p$	Pressure
$r$	Tube radius
$r_i$	Inside radius of tube
$r_o$	outside radius of tube
$t$	tube wall thickness [mm]
$WR$	Nominal wall reduction

$X_{edm}$	Cut depth in coordinates of the WEDM
$X_W$	Cut depth in wall coordinates
$\alpha$	Inner radius (of tube)
$\beta$	Outer radius (of tube)
$\Delta D$	Diametral expansion of the inside tube diameter
$\epsilon_{()}$	Strain, direction indicated in subscript
$\theta$	Direction index
$\lambda$	Substitution variable
$\mu$	Coeffieicnt of static friction
$\nu$	Poisson's ratio
$\sigma_r$	Stress normal to the radial direction
$\sigma_{xy}$	Stress on the plane normal to the $x$ -direction, acting in the $y$ - direction
$\sigma_\theta$	Stress normal to the $\theta$ direction
$\tau$	Shear stress
$\psi$	Substitution variable

## Definitions

Annulus Gas System	A system that maintains carbon dioxide gas in the space between the calandria tube and pressure tube in a CANDU <sup>®</sup> fuel channel.
Calandria Tube	Tube spanning the CANDU <sup>®</sup> reactor core separating the annulus gas system from the moderator.
End Fitting	Structure into which pressure tubes are terminated.
Iron-out	Rotation of the expansion tool with constant roller extension for the purpose of smoothing out the tube surface.

Nip-up	Initial expansion of the tube to take-up the nominal tube-tubesheet clearance.
Pressure Tube	Tube spanning the core in a CANDU® reactor forming the pressure boundary between the fuel channel and the annulus gas system.
Spring-back	Elastic contraction of the joint on removal of the roll expansion tool.
Tubesheet	Plate into which calandria tubes are terminated.
Wall Reduction	A measure of the amount of deformation imparted to the tube in mechanical roll expansion.

## Table of Contents

<b>Abstract</b> .....	<b>i</b>
<b>Acknowledgements</b> .....	<b>ii</b>
<b>Acronyms and Abbreviations</b> .....	<b>iii</b>
<b>List of Symbols</b> .....	<b>iv</b>
<b>Definitions</b> .....	<b>v</b>
<b>Table of Contents</b> .....	<b>vii</b>
<b>List of Tables</b> .....	<b>xiii</b>
<b>List of Figures</b> .....	<b>xiv</b>
<b>Chapter 1 Introduction</b> .....	<b>1</b>
1.1 Background.....	3
1.1.1 The CANDU® Fuel Channel .....	4
1.1.2 The AECL Gen-IV Fuel Channel .....	7
1.2 Motivation .....	8
1.3 Objectives.....	9
1.4 Methodology.....	9
1.5 Thesis Overview .....	10

<b>Chapter 2</b>	<b>Literature Review of the Mechanics of a Rolled Joint .....</b>	<b>11</b>
2.1	Process of Forming a Mechanical Expansion Joint.....	11
2.2	Simplified Mechanics of Rolled Joints.....	14
2.3	Roller / Tube Line Contact .....	17
2.4	Tube-to-Tubesheet Interface Pressure.....	19
2.5	Joint Quality.....	20
2.6	Simplifications of the Rolled Joint.....	21
2.6.1	Elastic Expansion of a Thick Cylinder Under Internal Pressure.....	22
2.6.2	Torsion on Inside of Thick Cylinder – Fully Restrained on Outside .....	22
2.6.3	Expansion of the Tube End: Axisymmetric Bending.....	23
2.6.4	Axial Extrusion of the Tube .....	24
2.7	Analytical Modeling.....	25
2.7.1	Nadai: Assumptions and Simplifications, and Agreement with Experiment .....	26
2.7.2	Results and Predictions of the Nadai model .....	28
<b>Chapter 3</b>	<b>Calculation of Residual Stresses .....</b>	<b>29</b>
3.1	Surface Stresses on Disassembly of Joint.....	29
3.2	Approximation of Tube / Tubesheet Interface Pressure .....	30
3.3	Calculation of the Average Stresses from Cutting.....	34
3.4	Calculation of the Stress Distribution: The Crack Compliance Method .....	35

3.4.1	The Forward Solution for the Crack Compliance Technique.....	37
3.4.2	The Inverse Solution for the Crack Compliance Technique.....	39
<b>Chapter 4</b>	<b>Implementation of the Crack Compliance Technique .....</b>	<b>41</b>
4.1	Computing the Forward Solution: Finite Element Analysis.....	41
4.1.1	Automation of Compliances Computation .....	44
4.2	Implementation of the Inverse Solution .....	44
4.3	Strain Measurements .....	45
4.4	Validation of the Implementation of the Crack Compliance Technique .....	45
4.4.1	Validation of the Forward Solution .....	46
4.4.2	Validation of the Implementation of the Crack Compliance Method .....	50
4.4.3	Testing the Limits of the Crack Compliance Technique.....	52
4.4.4	Summary of the Validation .....	58
4.4.5	Limitations of the Crack Compliance Method .....	58
<b>Chapter 5</b>	<b>Experimental Setup and Procedure .....</b>	<b>59</b>
5.1	Experimental Procedure .....	59
5.2	Experimental Setup.....	59
5.2.1	Test Pieces.....	59
5.2.2	Specifications of Tube Specimens .....	60
5.2.3	Specification of Tubesheet Plate Specimens .....	62

5.3	Rolling Equipment and Fixturing.....	63
5.4	Joint Assembly.....	67
5.4.1	Setup .....	67
5.4.2	Wall Reduction .....	68
5.4.3	The Joint Rolling Process.....	70
5.4.4	Joints Assembled .....	70
5.5	Release of Stresses in Rolled Joints .....	71
5.6	Measurement of Strains.....	72
5.6.1	Strain on Joint Disassembly .....	76
5.6.2	Strain on Cutting of the Freed Tube.....	77
5.7	Hardness Measurement .....	78
<b>Chapter 6</b>	<b>Results and Discussion.....</b>	<b>79</b>
6.1	Roll Expansion of Tubes into Tubesheets .....	79
6.2	Joint Disassembly .....	82
6.2.1	Strains Measured on Joint Disassembly.....	82
6.2.2	Residual Stresses Released on Joint Disassembly .....	89
6.2.3	Tube-to-Tubesheet Interface Pressure.....	91
6.3	Determining Residual Stress on Tube Slitting.....	94
6.3.1	Measured Strains on Slitting of Free Tubes .....	95

6.3.2	Residual Stress on the Tube Surface Released in Cutting of the Tubes.....	99
6.3.3	Residual Stress Distribution in the Tubes Post-Disassembly.....	101
6.3.3.1	Convergence and Selection of Polynomial Order.....	102
6.4	Surface Hardness.....	111
<b>Chapter 7</b>	<b>Summary &amp; Conclusions and Recommendations.....</b>	<b>113</b>
7.1	Summary & Conclusions.....	113
7.2	Recommendations.....	115
	<b>References.....</b>	<b>116</b>
	<b>Appendices.....</b>	<b>120</b>
	Appendix A : The Nadai Model.....	121
A.1	Overview of Derivation.....	121
	Appendix B : Implementation of Interface Pressure Calculation.....	129
	Appendix C : Strain Gauge Locations.....	132
C.1	Tube 10mm-8.3%WR.....	133
C.2	Tube 10mm-6.8%WR.....	134
C.3	Tube 10mm-5.0%WR.....	135
C.4	Tube 6mm-7.9%WR.....	136
	Appendix D : Annotated Strain Gauge Installation Photos.....	137
D.1	Tube 10mm-8.3%WR.....	138

D.2	Tube 10mm-6.8%WR .....	139
D.3	Tube 10mm-5.0%WR .....	140
D.4	Tube 6mm-7.9%WR .....	141

## List of Tables

Table 5-1: Mechanical material properties of tubes and tubesheet plates .....	61
Table 5-2: Summary of joint specimens .....	71
Table 5-3: Identification key for strain gauges .....	75
Table 6-1: Joint rolling parameters .....	80
Table 6-2: Measured strain on joint disassembly .....	82
Table 6-3: Change in diameter on joint disassembly .....	83
Table 6-4: Strains on the inside tube surface resulting from diametral expansion, axial contraction, and axial bending effects .....	84
Table 6-5: Surface stresses on joint disassembly.....	89
Table 6-6: Calculated interface pressure.....	92
Table 6-7: Residual stress released on cutting freed tube.....	100
Table A-1: Predictions of the Nadai model	125

## List of Figures

Figure 1-1: Illustration of CANDU® 6 fuel channel.....	5
Figure 1-2: CANDU® 6 fuel channel joint .....	6
Figure 1-3: Commonwealth #60 tube expander.....	7
Figure 1-4: AECL Gen-IV concept fuel channel.....	8
Figure 2-1: Cut-away illustration of rolling.....	12
Figure 2-2: Roller motion .....	13
Figure 2-3: Conceptual plot of radial loading vs radial expansion.....	15
Figure 2-4: Extrusion begins in zones of low axial restraint .....	16
Figure 2-5: Pentagonalizing of tube and reverse bending caused by simultaneous line contacts .....	18
Figure 2-6: Tube rotation within bore <sup>8</sup> .....	18
Figure 2-7: Illustration of force on tube and resultant plastic flow .....	24
Figure 2-8: Discolored rollers.....	25
Figure 2-9: Interface pressure vs. wall reduction.....	28
Figure 3-1: Geometry of interface pressure relation.....	31
Figure 3-2: Illustration of the principle of superposition.....	36
Figure 3-3: The shifted Legendre polynomials.....	39

Figure 4-1: Meshed geometry shown with a cut midway through the wall thickness.....	42
Figure 4-2: Example of compliance of outside diameter gauge .....	43
Figure 4-3: Example of inside diameter gauge compliance.....	43
Figure 4-4: Geometry of beam model.....	46
Figure 4-5: Simulated strain as compared published values for a rectangular beam [34]	48
Figure 4-6: Variation in strain response of the FEA model to various mesh densities ....	49
Figure 4-7: Function $\sin(y)$ validating the implementation of the crack compliance technique .....	51
Figure 4-8: Function $\cos(y)$ validating the implementation of the crack compliance technique .....	52
Figure 4-9: Polynomial fits to step function input .....	53
Figure 4-10: Individual polynomial fits to step function input (Alternate presentation to Figure 4-9) .....	54
Figure 4-11: Polynomial fits to square wave input .....	56
Figure 4-12: Individual polynomial fits to square wave input (Alternate presentation of Figure 4-11) .....	57
Figure 5-1: Tube details (10 mm wall) .....	61
Figure 5-2: Tube details (6 mm wall) .....	62
Figure 5-3: Split tubesheet plate .....	63

Figure 5-4: Commonwealth # 60 rolling tool .....	64
Figure 5-5: Sweep of skewed rollers <sup>8</sup> .....	64
Figure 5-6: Motion of roller relative to mandrel <sup>8</sup> .....	64
Figure 5-7: Photo of one individual roller .....	65
Figure 5-8: Rolling setup viewed from inboard side, nip-up clamp removed .....	66
Figure 5-9: Roll-expansion setup.....	67
Figure 5-10: Illustration of loading of upper tubesheet plate .....	68
Figure 5-11: Steps in releasing stresses in tubes.....	72
Figure 5-12: Illustration of strain gauge locations on tube inside diameter .....	75
Figure 5-13: Tube 10mm-8.3%WR in WEDM prior to cutting .....	77
Figure 6-1: Deviation of actual wall reduction from nominal wall reduction .....	81
Figure 6-2: Strain on release of tube from joint.....	83
Figure 6-3: Assumed shear stress acting to restrain axial contraction.....	85
Figure 6-4: Ratio of axial strain to hoop strain .....	88
Figure 6-5: Surface stresses on joint disassembly .....	90
Figure 6-6: Interface pressure as function of wall reduction .....	93
Figure 6-7: Axial strain in 10 mm tubes on slitting.....	96
Figure 6-8: Hoop strain in 10 mm tubes at bore midpoint on slitting.....	97

Figure 6-9: Hoop and axial strain in 6 mm tubes at bore midpoint on slitting .....	99
Figure 6-10: Residual stress released in cutting freed tube .....	100
Figure 6-11: Tube 10mm-6.8%WR through thickness hoop stress distribution at A1 location based on gauge on the outside diameter.....	103
Figure 6-12: Comparison of predictions based on gauges on the inside and outside surfaces .....	104
Figure 6-13: Illustration of error resulting from modeling plastically deformed material as perfectly elastic .....	105
Figure 6-14: Stress distributions at the A1 location for tube 10mm-8.3%WR.....	107
Figure 6-15: Through thickness stress distributions at bore midpoint (A1 location) .....	108
Figure 6-16: Through thickness stress distribution outboard of bore midpoint (B2 location) .....	109
Figure 6-17: Hardness of tube inside surface .....	111
Figure 6-18: Hardness of tube outside surface <sup>32</sup> .....	112
Figure A-1: Predicted contact pressure with pressure applied on inside surface .....	126
Figure A-2: Interface pressure after spring-back .....	127
Figure B-1: Implementation of interface pressure calculation in Microsoft Excel .....	130
Figure B-2: Sample calculation of interface pressure.....	131

## Chapter 1 Introduction

Nuclear power is an important part of the mixture of energy sources in many countries. The CANada Deuterium Uranium, or CANDU<sup>®</sup>, reactor is a nuclear power reactor developed by Atomic Energy of Canada Limited (AECL). The CANDU<sup>®</sup> reactor is a heavy water cooled design with pressurized fuel channels within an unpressurised moderator vessel. There are 29 CANDU<sup>®</sup> power reactors worldwide in 900 and 600 MW<sup>1</sup> sizes. The reactors each have slight differences, such as the number of fuel channels and geometry of the calandria tubesheet grooves. However, the calandria tube (CT) and pressure tube (PT) rolled joints are similar between reactors and experience the same conditions during operation, shutdown, and cooldown. As a result of these similarities, all CANDU<sup>®</sup> reactors can be treated as equivalent for the purpose of this study.

The CANDU<sup>®</sup> reactor core consists of a short cylinder approximately 6 m in diameter and 6 m long, with its axis of symmetry oriented horizontally. The cylinder is filled with heavy water at near atmospheric pressure and ambient temperatures which serves as a moderator. An array of fuel channels (380 to 460, depending on the reactor design) spans the calandria between the cylinder ends. The outermost component of the fuel channel is a thin-walled tube in direct contact with the moderator and sealed to a tubesheet at each end; these tubes are called calandria tubes. Installed inside the void created by the calandria tubes are thicker-walled tubes that form the pressure boundary for the hot heavy water coolant; these tubes are called pressure tubes. The pressure tubes contain fuel bundles which are sealed to end fittings (EF) at each end to form part of the primary heat transport system. A gap is maintained between the hot pressure tubes and the cooler calandria tubes by garter springs called annulus spacers. Gas flows in this gap as part of a system to monitor for fuel channel leaks, called the Annulus Gas System (AGS).

---

<sup>1</sup> Nominal generating capacity electric.

In the pursuit of a safe and secure energy supply for Canadians, Atomic Energy of Canada Limited continues to advance the state of nuclear technology, one aspect of which is the development of the next generation of nuclear power reactor, the “Gen-IV reactor”. The AECL concept for the Gen-IV reactor is a supercritical water cooled reactor [1]. This new reactor concept imposes a different set of conditions on the fuel channel in general, and the pressure tube joint in particular, as compared to the conventional CANDU® 6 design. Key differences include the higher temperatures and pressures of the supercritical fluid contained in larger in diameter pressure tubes.

The ongoing development of the Gen-IV reactor highlights a need to re-evaluate, and if possible extend the understanding of, tube-to-tubesheet joining technology, which introduces the consideration of residual stresses. Residual stresses are internal elastic stresses that remain within a component after the part has been plastically deformed through the application of a load (e.g. applied pressure of rollers, or thermally induced deformation). Since these residual stresses cannot be measured directly, they are calculated from the strains measured on the release of these stresses. The residual stress states in the joint components are fundamental to the function of the rolled joint. Experimental work was undertaken in this study to characterize these stresses. This was accomplished through measurement of strains in the tube joint, with the intention of determining the through thickness hoop stress distribution in the tube wall. While the Gen-IV fuel channel has not been designed in detail, the experimental work described in this thesis was performed using a tube geometry that fits the general geometry suggested for a Gen-IV PT based on consideration of nuclear physics, heat transfer, and tube axial strength. Using this tube geometry as the backdrop of the experimental results, the intention is to comment on the applicability of the body of existing rolled joint research to the Gen-IV fuel channel geometry.

## 1.1 Background

There exist a number of methods to join tubes. Some joining techniques rely on the formation of atomic bonds between the joined components. Two prominent examples of such joining techniques are welding and brazing. These techniques are reliant on a chemical compatibility between the joined components. A second set of techniques rely on residual stress to maintain a contact pressure between the components and do not require chemically compatible materials. Examples of such joining techniques include threading, shrink-fitting, and mechanical expansion. In the case of a threaded joint, the residual stress is imparted in the form of pretension, and is typically controlled by means of an installation torque. In the case of shrink-fitting, the residual stress is imparted by exploiting the phenomenon of thermal expansion. In the case of mechanical expansion, the residual stress is imparted by a tool stressing the joint components into the plastic zone such that residual elastic stresses maintain contact pressure after removal of the applied forces.

The material selection for pressure tubes in CANDU® reactors is dominated by considerations for neutron physics, such as minimizing the neutron absorption, and secondarily for mechanical properties. Zirconium alloys such as Zr 2Nb or Zr 2.5Nb are principally used. Mechanical expansion has been conventionally used to join pressure tubes to end fittings, as well as calandria tubes to tubesheet (TS) plates<sup>2</sup>, since steel and zirconium alloys are incompatible for welding. Mechanical roll expansion is the method used to achieve the expansion. A thorough understanding of these joints is of strategic importance, and consequently much research has been undertaken to that end [2]. In particular, the pressure tube joint has undergone much study [3]. The performance of

---

<sup>2</sup> The fuel channel components are explained in detail in Section 1.1.1.

pressure tube to end fitting joint design employed in existing CANDU<sup>®</sup> power reactors is evident by decades of service.

### 1.1.1 The CANDU<sup>®</sup> Fuel Channel

Common to CANDU<sup>®</sup> style reactor designs (CANDU<sup>®</sup> 6, Enhanced CANDU<sup>®</sup> 6 (EC6), Advanced CANDU<sup>®</sup> Reactor) are pressure tubes forming a pressure boundary in the calandria vessel between the primary heat transport system and the annulus gas system, and calandria tubes forming the boundary between the annulus gas system and the moderator. Figure 1-2 illustrates the basic CANDU<sup>®</sup> 6 and Advanced CANDU<sup>®</sup> Reactor (ACR) designs. The inboard side of the joint is the inside of the calandria vessel, and hence the joint is formed by inserting the expansion tool from the outboard side. Both end fittings and tubesheet plates contain circumferential grooves into which tube material flows under the mechanical expansion forces. In the case of CANDU<sup>®</sup> 6 and ACR fuel channel designs, the pressure tube to end fitting joint is a two-piece joint (i.e. the tube rolled directly into end fitting), while the calandria tube-to-tubesheet plate joint is a three-piece joint (i.e. the tube is sandwiched between an insert and the tubesheet). One particular Gen-IV concept fuel channel includes large diameter pressure tubes rolled directly into the tubesheet, and does not include calandria tubes [1]. Since the end fitting and tubesheet plate serve the same role in forming joints, these terms are used interchangeably in this thesis. In the cases of CANDU<sup>®</sup> 6 and ACR joints, the mechanical deformation is applied by roll expansion using a custom tube expander (see Figure 1-3). The radial compressive stress between the tube and the restraint forms an interface leak-tight with respect to heavy water (moderator in the case of the calandria tube/tubesheet joint and the primary heat transport system in the case of the pressure tube end fitting joint).

CANDU 6 Fuel Channel

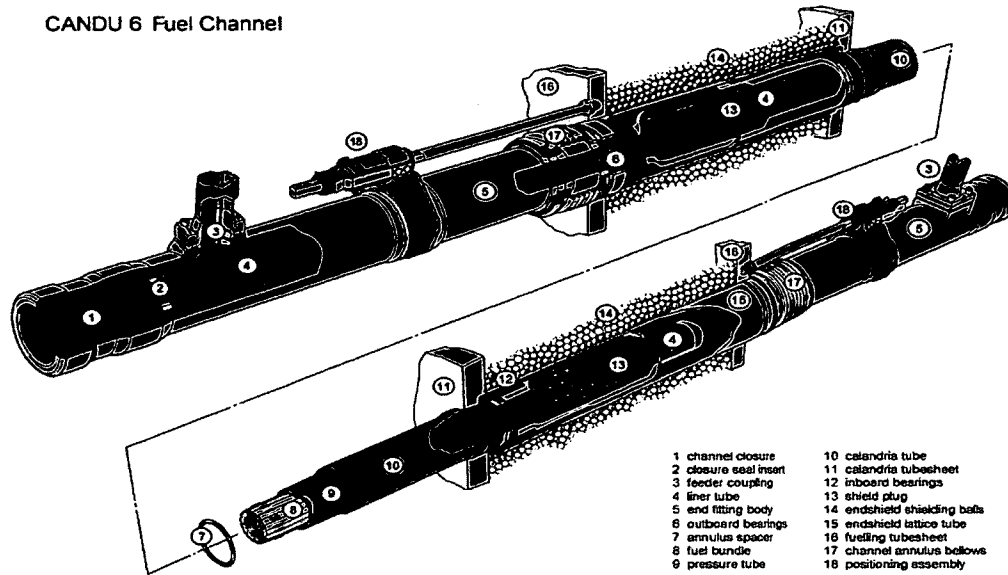


Figure 1-1: Illustration of CANDU® 6 fuel channel<sup>3</sup>

<sup>3</sup> Image retrieved from [www.canteach.candu.org](http://www.canteach.candu.org)

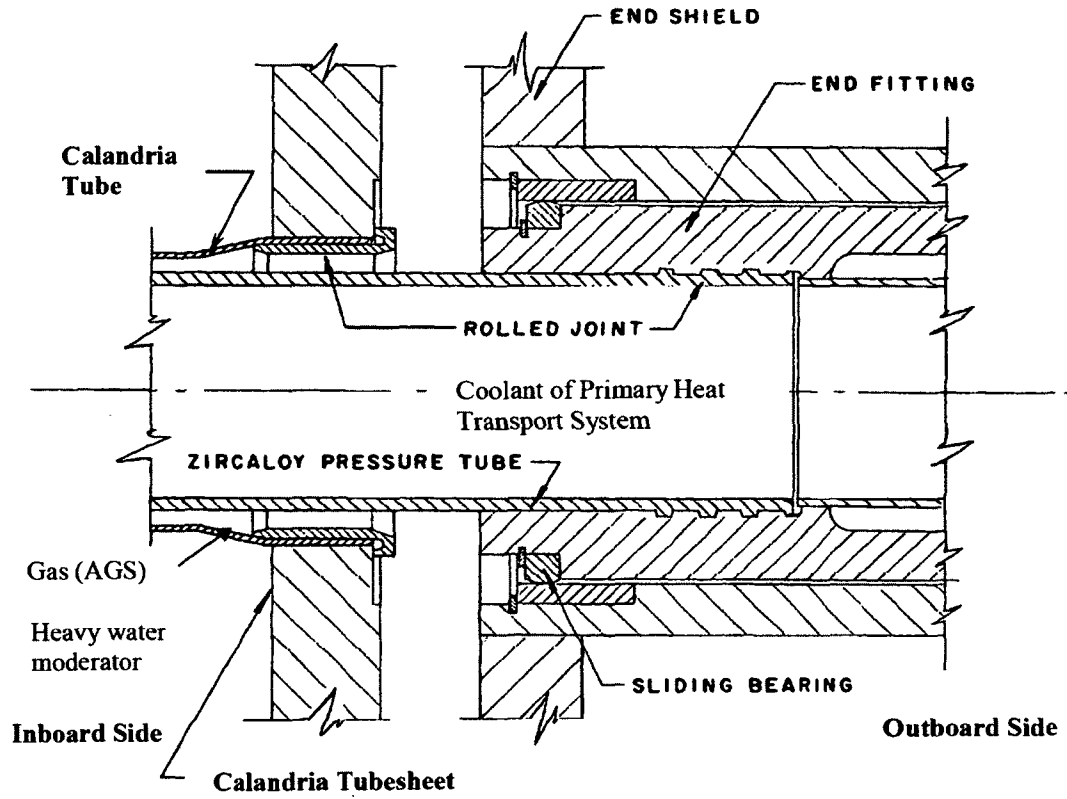


Figure 1-2: CANDU® 6 fuel channel joint <sup>4</sup>

---

<sup>4</sup> Figure adapted from [43]

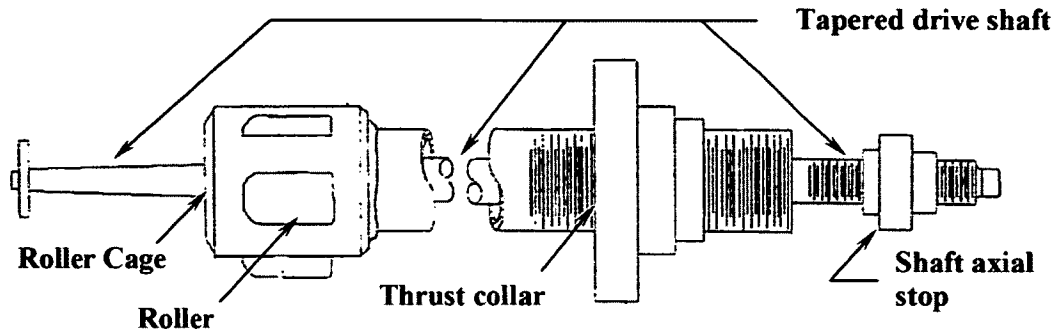


Figure 1-3: Commonwealth #60 tube expander

### 1.1.2 The AECL Gen-IV Fuel Channel

The AECL concept for the Gen-IV fuel channel, as shown in Figure 1-4, is a large diameter (~ 160 mm diameter), thick-walled (~10 mm wall) pressure tube made from a zirconium alloy such as Zr-4 or Zr-2.5Nb. In service, the outside of the pressure tube is in direct contact with the moderator fluid (heavy water, D<sub>2</sub>O) at nearly atmospheric pressure (~101 kPa). The pressure tube is somewhat protected from the high temperature of the light water coolant (>380°C) flowing through the channels and over the fuel bundles by an insulating insert such as the Ytria Stabilized Zirconia (YSZ) insert [1]. This isolation is required because of the strength requirements to contain the high pressure coolant (22 MPa), and the drastic reduction in yield strength exhibited by zirconium alloys at high temperatures [4].

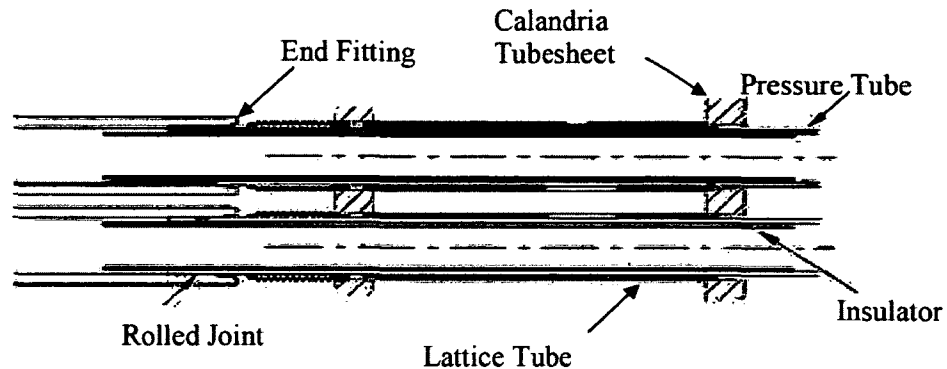


Figure 1-4: AECL Gen-IV concept fuel channel<sup>5</sup>

## 1.2 Motivation

The use of zirconium pressure tubes in CANDU<sup>®</sup> reactors necessitated the development of specialized joining technology to build a robust reactor. The drive to continue to advance safe nuclear solutions for Canadians suggests taking another look at technologies that perform satisfactorily in existing reactor designs. Changes to the fuel channel are a likely outcome of changes to the reactor core physics. Thus the current work aims to further the understanding of rolled joints.

Proper function of a rolled joint is normally judged by leak-tightness of the joint against leakage across the pressure boundary (liquid heavy water coolant in the case of CANDU<sup>®</sup> 6 and ACR, and supercritical water in the case of Gen-IV) as well as pull-out strength from the rolled in component. For a joint produced by roll expansion to be leak-tight it is essential for compressive residual stress to exist in the radial direction between the tube (pressure tube or calandria tube) and bore (end fitting or tubesheet) after the forming operation. The magnitude of this stress is accepted as a measure of the joint quality,

<sup>5</sup> Figure adapted from [1].

which in turn is determined by the residual stress profile in the tube [5]. However, in the literature reviewed, the hoop stress distribution through the wall thickness has not been determined experimentally.

### 1.3 Objectives

The first objective of this thesis is to understand the state of residual stress that exists in the tube after being rolled into a joint. More specifically, the objective is to understand the distribution of hoop stress through the wall thickness and the effect of wall thickness and wall reduction on this distribution. While previous work has shed much light on this topic [6] [7] [8] [9] [10], the present work differs from previous work by experimentally determining the distribution of the hoop stress through the tube wall thickness.

A secondary goal of this thesis is to evaluate the crack compliance method as a tool for the experimental investigation of the residual circumferential stress state of the tube joints formed through roll expansion. This technique was pioneered in the 1970's under M. Prime and Hill, Finnie, etc [11]. There have been numerous previous applications of this technique including residual stress state of friction stir welding of butt-welded aluminium plates [11] [12].

### 1.4 Methodology

Large diameter, thick-walled tubes (153 mm inside diameter, 6 and 10 mm wall) were rolled into custom-designed split tubesheet plates with varying amounts of wall reduction to form test joints that could be disassembled without cutting the tube. Experimental data were gathered via strain measurements of the tube on disassembly of the rolled joint. The strain measurements were taken using strain gauges applied to the inside of the tube. Additional gauges were then applied to the outside of the tube. An axial cut was

introduced into the tube with a wire electrical discharge machining (WEDM) operation, and successively extended while measuring the strain resulting from the stress released at each increment of slot extension. The surface stress released on cutting was then obtained from the measured strain. The crack compliance method allows calculation of the hoop stress distribution using the strains measured at each increment of slot extension.

### **1.5 Thesis Overview**

Discussed in this thesis are rolled joint technology in general, and the pressure tube rolled joint technology specifically. Chapter 2 presents the literature review of the current understanding of the mechanics of rolled joints including a theoretical description of the joint rolling process and predictions of existing models. Chapter 3 presents the calculations used to obtain stresses from the measured strains. Chapter 4 presents the method of implementing the crack compliance method to obtain the through-thickness stress distribution.

The experimental methods employed are presented in Chapter 5. This includes the details of the joints fabricated for testing, of the method for disassembling the joint, and of the method used for data collection. The details of the crack compliance method are also described in this section.

Chapter 6 presents the results obtained from testing and from the subsequent calculations using the methods detailed in Chapter 5.

The conclusions drawn from the present work are presented in Chapter 7, along with recommendations for further study.

## **Chapter 2 Literature Review of the Mechanics of a Rolled Joint**

This section presents a description of the process of forming a rolled joint through roll expansion, along with various models that can be used to gain insight into the rolling process. The limitations and simplifications of these models are briefly discussed.

### **2.1 Process of Forming a Mechanical Expansion Joint**

Fundamental to the understanding of rolled joints is consideration of the forming process. A rolled joint is essentially an interference fit between a tube and tubesheet plate. The sizing of the tube and tubesheet plate, as manufactured, allows for free assembly. The tube is expanded by an applied load on the inside diameter to induce fully plastic deformation such that on removal of the loading tool, an interference fit exists where the relaxed state of the joint maintains residual stress across the tube/tubesheet interface [13] [5]. Residual stresses remain in both the tube and tubesheet plate and consequently at the tube-tubesheet plate interface. The pressure at this interface is termed “interface pressure”. The magnitude of the hoop stresses are expected to be as high as two thirds of the yield strength (0.2% strain basis) [14].

Hydraulic expansion and mechanical roll expansion techniques have both been used to produce mechanically expanded joints. One advantage of hydraulic expansion is that it stiffens the tubesheet during expansion, allowing for a relatively compact pitch spacing of tubes, for a given hole diameter [13]. Alternatively, roll expansion is advantageous in inducing a higher degree of strain hardening of the inner shells of the tube resulting in joints less prone to fatigue failure [13]. The method of interest in the present work is mechanical roll expansion using a pneumatically actuated rolling tool that consists of five rollers driven by a tapered mandrel and held in position by a roller cage (see Figure 1-3 and Figure 2-1).

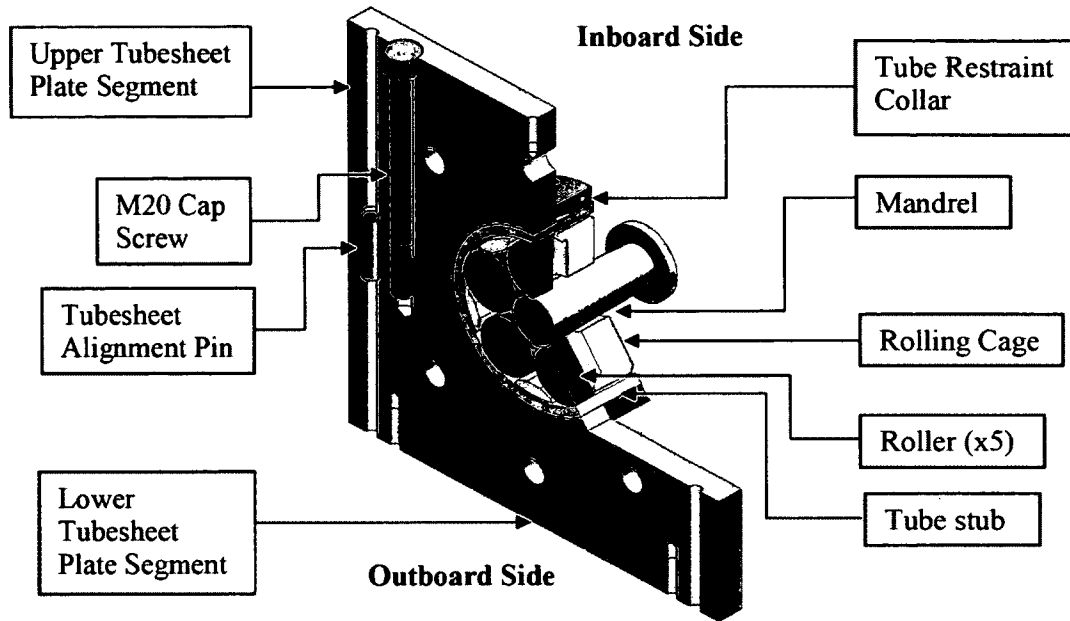


Figure 2-1: Cut-away illustration of rolling

From the perspective of the operator assembling a rolled joint, there are four phases to the process after the free assembly of the components:

1. Nip-up: The tube is positioned in the tubesheet plate or end fitting and the expanding tool is inserted from the outboard side. As the mandrel rotates the rollers move in the same direction, rotating in the opposite direction, as shown in Figure 2-2. The tube is expanded until the outside diameter of the tube contacts the inside diameter of the tubesheet plate. The amount of expansion required is calculated to be equal to the nominal radial gap between the components.

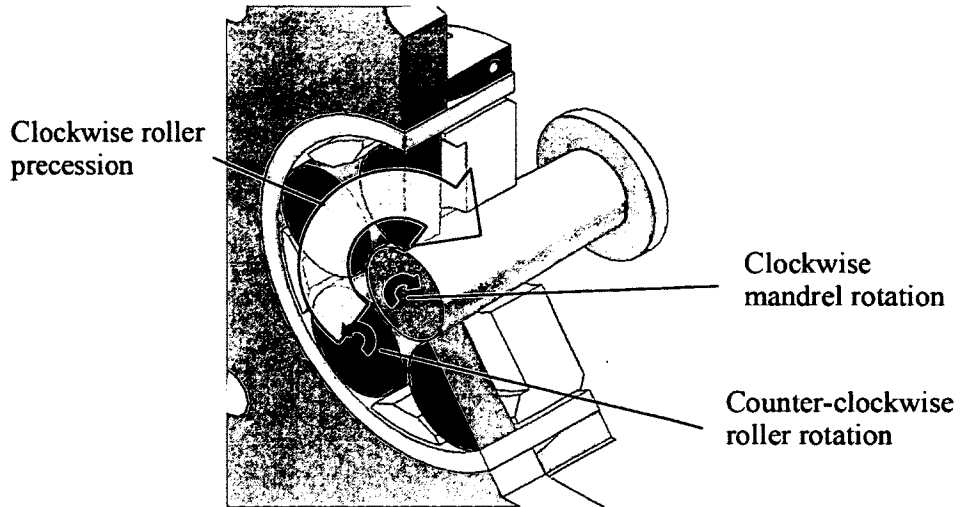


Figure 2-2: Roller motion

2. Expansion: the tube is further expanded until the target diameter (i.e. the target percent wall reduction) is reached. The target roller expansion to achieve this point is set by adjustment of the shaft axial stop (see Figure 1-3).
3. Iron-out: The mandrel rotation is continued a prescribed number of rotations without further roller expansion. By continuing the rotation with a constant radial roller position, the tube inside diameter is smoothed out.
4. Retraction: the direction of the mandrel is reversed and the rollers retract into the mandrel cage and the mandrel is removed. If the actual joint diameter is below the target diameter, the mandrel is reinserted, the shaft axial stop is adjusted outwards, and a further expansion and iron-out is performed. Joints once-rolled are thought to behave identically in service to twice-rolled joints.

Since it is not practical to measure the parameters known to be critical to joint performance in-situ (ie. leak rate, pull-out strength, or interface pressure) determination of the quality of a joint is not always straightforward. In many instances the quality of

the joint is determined by cross referencing measurable parameters of the formed joint (e.g. percent nominal wall reduction, location of the burnish mark, etc.) against those of reference joints prepared in the laboratory. In this work the amount of rolling is quantified by the nominal percent wall reduction.

## 2.2 Simplified Mechanics of Rolled Joints

A complex stress state exists in the tube in a tube-to-tubesheet joint formed through mechanical roll expansion [15]. Simplifying the mechanics of forming a rolled joint provides a conceptual picture of what is happening during the rolling of the joint and can provide the foundation to understand the analysis discussed later in this thesis.

Considered in the following subsections are the steps leading to the development of final stress state in a rolled joint.

The final stress state in the joint is developed in the seven steps that follow (adapted from [16]). The changes in radial loading that accompany the radial displacement are illustrated in Figure 2-3.

1. The components of the joint are freely assembled in a stress free state. The rollers advance radially as they are driven around the circumference of the tube inside diameter. The tube expands with elastic stresses developing in the tube.
2. Extremely high stresses develop under each of the rollers and zones (one per roller) such that plastic deformation is initiated in the tube, and possibly the tubesheet plate. The local yielding in these regions of high stress alters the geometry of the contacting surfaces, thereby altering the contact pressure distribution; however, more critical stress states may exist under the surface [17]. It is typical (but not necessary) for the tube to be fully plastic before the tubesheet bore is contacted [15]. The deformation is confined to the radial and circumferential directions. Axial extrusion of material under the roller is restrained by adjacent tube material. The plastic strain in the circumferential

direction is equal and opposite to the sum of the elastic compression of the tube material and the small tensile elastic strain of the hub at its inner boundary.

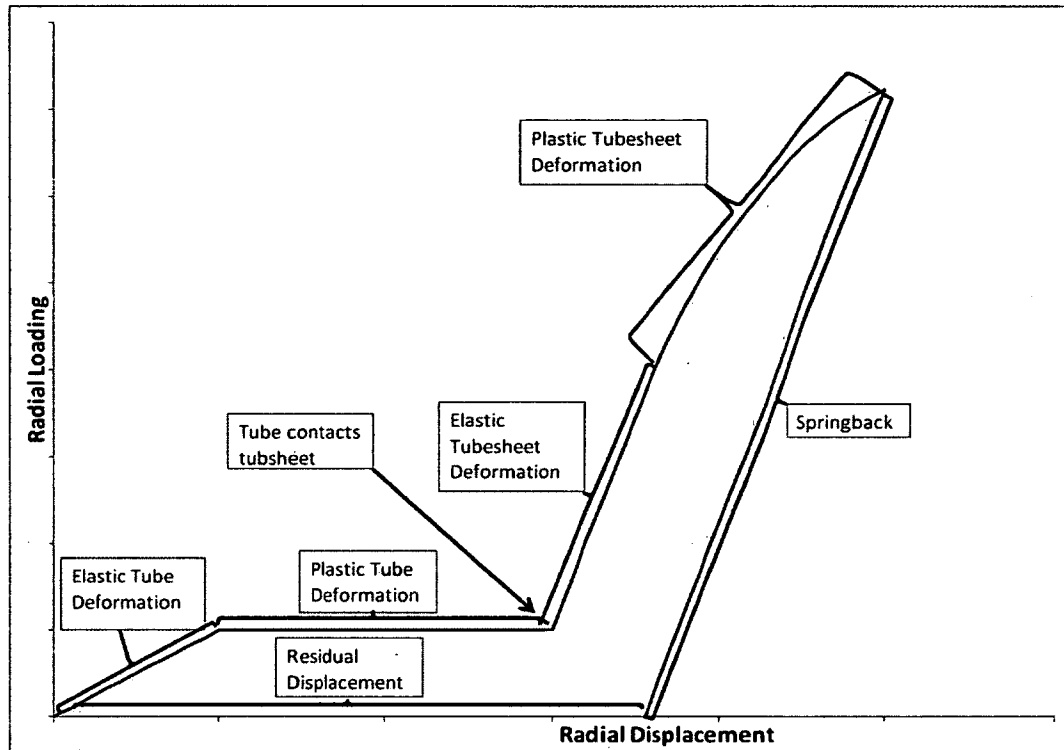


Figure 2-3: Conceptual plot of radial loading vs radial expansion<sup>6</sup>

3. Axial extrusion of the tube begins at locations of high compressive radial and hoop stress and low axial stress (ie. near the inboard and outboard edges of the tubesheet), as shown in Figure 2-4.

<sup>6</sup> Figure adapted from [20].

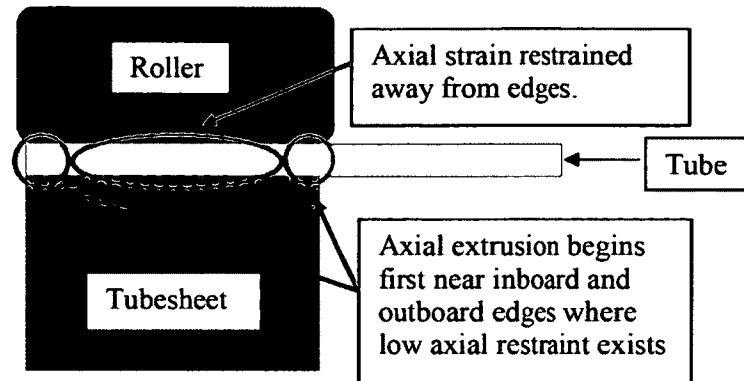


Figure 2-4: Extrusion begins in zones of low axial restraint

4. Plastic deformation of the tube begins in the radial and circumferential directions at locations under the roller of high restraint in the axial direction (i.e. away from the tubesheet edges). The restraint to axial extrusion of the tube by adjacent material creates a 3D compressive stress state, resulting in residual compressive stresses imparted in the tube. The difference between steps 3 & 4 is that plastic compressive strains in the remainder of the tube are introduced in step 4 [16]. During this step there will be a small amount of tube axial deformation.
5. Significant axial extrusion (i.e. approximately 10%) is imparted in this step. The transition to this phase occurs after the interface pressure has approached its maximum<sup>7</sup>. As a consequence, the large axial extrusion is an indication that the joint expansion is sufficient for the interface pressure to have developed.
6. Expansion of the rollers stops and the rollers bring the entire circumference into the same uniform diameter, effectively smoothing out the bore. This smoothing operation is referred to as “Iron-out”.
7. The rollers are reversed out of the tube; the roller forces are gradually reduced to zero. Both the tube and tubesheet spring-back. Since the tubesheet carries most of the load of the rollers by backing the tube, the spring-back of the tubesheet will

<sup>7</sup> The concept of maximum interface pressure is explored via the Nadai model, detailed in Section 2.7.

tend to effect an elastic or elasto-plastic compression of the tube. It has been observed that the spring-back effect in fact increases the contact pressure when the modulus of elasticity of the tubesheet is larger than the modulus of elasticity of the tube [5].

### 2.3 Roller / Tube Line Contact

With roll expansion, each roller applies a loading over a narrow line of contact with the tube's inner surface. The line contact between the roller and tube occurring during roll expansion is a distinct difference from expansion under hydrostatic (quasi-static load application) pressure. Hydrostatic loading is uniform over the tube surface, without localized stress concentrations caused by the tube / roller interfaces. The localized high stress region is important when modelling the joint rolling process including strain hardening of the material. Initially the roller / tube area of contact is essentially zero, resulting in infinitely high contact pressure. In practice however, the tube deforms elastically, increasing the contact area. The resultant shape of the contact is an area approximately rectangular. The normal stress distribution at the surface is highest at the midpoint across the contact area width, and reduces to zero at the edge of the contact area. Being elastic, this deformation corresponds with a decrease in the tube length and wall thickness by the Poisson effect [13]. Continued expansion of the rollers begins to deform the tube plastically.

The simultaneous line contacts of the five rollers of the rolling tool cause some degree of pentagonalizing of the tube, and to a lesser extent the backing tubesheet (or end fitting) [14]. The segments of the tube between the line contacts is in reverse bending (bending inwards), with the resultant stresses increasing with decreasing wall thickness. This effect is illustrated in Figure 2-5. Additionally, the localized contact of the rollers causes the tube to rotate in the bore in the same direction as the mandrel rotation. This motion, as illustrated in Figure 2-6, is the effect of elastic deformation in front of the roller and spring-back behind the roller.

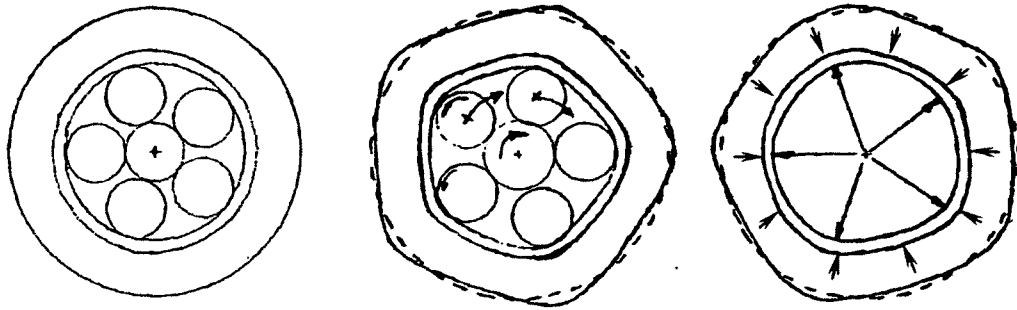


Figure 2-5: Pentagonalizing of tube and reverse bending caused by simultaneous line contacts<sup>8</sup>

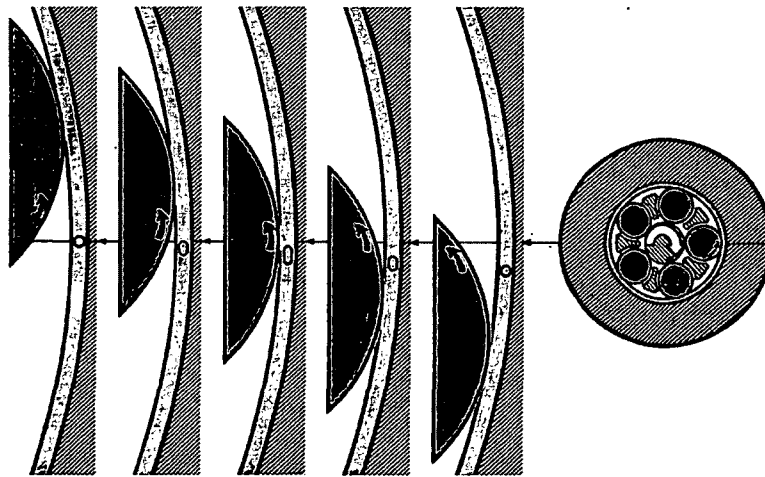


Figure 2-6: Tube rotation within bore<sup>8</sup>

---

<sup>8</sup> Figure adapted from [14].

The stress in the tube is very high immediately under the roller because of the small contact area. However, the maximum von Mises stress occurs below the surface of the tube [17]. As the ratio of the surface shear stress to normal stress increases, the maximum stress migrates closer to the tube surface [18]. The total load applied to the inside diameter of the tube is partially taken up by the hoop stress developed in the tube, and partially by the tubesheet. While the highest stresses occur in the tube, the stiffness of the tubesheet plate results in a relatively small proportion of the load being taken by the tube. As a result, when the roller loads are removed, the spring-back of the tubesheet corresponds to the unloading of a larger fraction of the applied load. Consequently, elastic or elasto-plastic compression of the tube results. If sufficient stress has not been imparted into the tube through yielding by the rolling process, the hub spring-back may increase the residual loading [16]. It is expected that with increasing tube wall thickness the proportion of the load taken up by the hoop stress in the tube increases, and thus less spring-back of the tubesheet occurs after release of the load.

As the rollers advance, an element in the tube is subjected to a cyclic load of increasing magnitude. The degree of yielding in the tube following expansion will depend, in part, on the strain softening or hardening characteristics of the material. The situation in the case of mechanical roll expanded joints is complicated in that strain softening or hardening behavior of a particular material under cyclic loading, in some instances, differs depending on the magnitude of the cyclic loads applied [19].

#### **2.4 Tube-to-Tubesheet Interface Pressure**

The desired outcome of roll expanding a tube into a tubesheet plate is to deform the tube and tubesheet such that after relaxation of the tube and tubesheet on removal of the expanding tool, residual stress (referred to as “interface pressure”) remains at the location of the tube-tubesheet interface [13]. The magnitude of this interface pressure is understood to be an indication of the quality of the joint [20]. The effect of various

design parameters was investigated by Kalnius [20] using an analytical model built under the simplification of zero axial stress (i.e. plane stress). This assumption of plane stress is not consistent with the rolling process as described in Section 2.1. However, these predictions can be used as the baseline from which to build a conceptual understanding of the influence of various design parameters.

The Kalnius model predicts that the maximum contact stress is obtained for rolling to a wall reduction of 3 to 6%. This is approximately consistent with the prediction of the Nadai model, discussed in Section 2.7.2. Another prediction from Kalnius is that the contact pressure will be proportional to the ratio between wall thickness of the tube to its outer diameter. This conclusion is consistent with the work of Sutcliffe and Hayes [21], which indicates that a minimum ratio of tube wall thickness to tube bore limits the ability to form a conventional (2 piece) joint. The Sutcliffe report presents specific values of this ratio for Zr-2.5Nb tubes and 410 stainless steel end fittings. Beyond this limit a sandwich type joint (3 piece joint) is recommended.

Kalnius predicts that interface pressure increases with increasing value of the ratio between the yield strength of the tubesheet to the yield strength of the tube [20]. This assertion is consistent with the design recommendation in the Sutcliffe report to use end fittings with higher hardness, an indication of higher yield strength, for rolling of tubes with higher hardness.

## 2.5 Joint Quality

The quality of a formed rolled joint is typically judged against two primary criteria: pull-out strength and leak tightness. In the case of CANDU<sup>®</sup> fuel channels, the joint is designed to have a minimum pull-out load at least as large as the theoretical load required to yield a tube of nominal geometry. This parameter is related to both ensuring sufficient joint strength and controlling the pressure tube failure mechanism. The pull-out strength of a particular joint design is qualified experimentally using a test rig that destructively pulls test assemblies to failure. The pull-out strength is dependent on the friction

resultant from the contact pressure between the tube and the tubesheet, and by the circumferential grooves in the tubesheet. However, the load is primarily carried by the grooves and the majority of the load is carried by the most inboard groove [22]. The mechanism for transferring load to the grooves is related to the axial extrusion of the tube, however the effects of the joint grooves are outside of the scope of this thesis.

The degree of leak tightness of the joint is important in maintaining the pressure boundary. However, joint leak tightness is often paid disproportionate attention because it is seen as an indication of the quality of the joint that can be quantified non-destructively. In the case of calandria tube and pressure tube rolled joints, helium leak testing is used, with the leak rate criteria being set based on historical results, or empirical relationships.

## **2.6 Simplifications of the Rolled Joint**

Discussed in this subsection are four simplistic deformations of thick-walled cylinders: elastic expansion of a thick-walled cylinder, torsion transmitted through the wall thickness of a tube, axisymmetric bending of a tube, and axial extrusion of the tube wall. Each of these deformations omits important characteristics of the rolled joint. However, each explains a mechanism relevant to the formed rolled joint.

### 2.6.1 Elastic Expansion of a Thick Cylinder Under Internal Pressure

Elastic expansion of a thick-walled tube through application of pressure to the inside surface will result in compression in the radial direction, and tension in the hoop direction. In the elastic regime the radial and hoop stresses ( $\sigma_r$  and  $\sigma_\theta$ , respectively) at a given radius ( $r$ ) are derived by Chakrabarty [23] giving the relations in Equations 5-1 and 5-2.

$$\sigma_r = -p \cdot \left( \frac{\beta^2/r^2 - 1}{\beta^2/\alpha^2 - 1} \right) \quad (5-1)$$

$$\sigma_\theta = p \cdot \left( \frac{\beta^2/r^2 + 1}{\beta^2/\alpha^2 - 1} \right) \quad (5-2)$$

where:  $\alpha$  and  $\beta$  are the inner and outer radii, respectively, and  $p$  is the applied pressure. These equations indicate that the magnitudes of both stresses are highest on the inner surface and decrease moving radially outward.

When the tube is restrained on the outside surface (i.e. increasing expansion pressure beyond the point where the tube has expanded to the diameter of the tubesheet bore), the radial pressure begins to be transferred to the restraint.

### 2.6.2 Torsion on Inside of Thick Cylinder – Fully Restrained on Outside

A thick-walled tube that is loaded in such a manner as to rotate the inside diameter relative to the outside diameter is loaded in torsion. The elastic shear stress in this loading is in the circumferential direction on the radial face and the complementary stress is in the radial direction on the circumferential face. While the shear stress ( $\tau$ ) is elastic,

the shear stress at a given radius ( $r$ ) is a function only of the applied shearing stress ( $\tau_i$ ), the inside radius ( $r_i$ ), and of radial position ( $r$ ). The distribution through the thickness is given by Equation 5-3.

$$\tau(r) = \tau_i \cdot \frac{r_i^2}{r^2} \quad (5-3)$$

In the case of a tube with 165 mm inside diameter and 10 mm in wall thickness, the ratio of shear stress on the inside surface to that on the outside surface is approximately 1.2.

The rolling process could produce such a loading via the following mechanism; as the rollers travel around the tube inside diameter, the material immediately in front of the roller is at a radius equal to the radius to which it was expanded by the previous roller pass less some amount of spring-back. As the roller advances, the force applied by the roller consists of a radial component plus a tangential component. This torsion effect would be the cumulative result of the five rollers each forcing the tube inside diameter in the tangential direction.

### 2.6.3 Expansion of the Tube End: Axisymmetric Bending

Expansion of the end of a tube (i.e. “bellling” the end) develops a zone where the tube diameter transitions from the undeformed diameter to the expanded diameter. This transition is the result of the tube being in a state of axisymmetric bending. The stresses in this transition zone are of particular relevance to pressure tube design since tensile stresses can lead to stress corrosion-cracking or delayed hydride cracking [24]. There are two factors that contribute to the axisymmetric bending: the net extrusion of the tube wall while restraining the pressure tube/tubesheet interface, and the changing diameter between the rolled-in section on the rolled-in portion of the tube. The first effect results from elongation of the inside of the tube in axial direction (extrusion of the tube wall) while restraining the outside surface of the tube at the pressure tube/tubesheet interface. This effect was investigated by, among others, Van Wissen and Cashen, who concluded

that a large tangential bending stress can exist in the tube, with the tensile stress on the inside, and that this bending stress seemed to be higher in the thin-walled tubes than in thick-walled tubes [25].

#### 2.6.4 Axial Extrusion of the Tube

Axial extrusion of the tube material occurs in the later steps of joint rolling (steps 4 and 5, in Section 2.1). Once the stress state in the tube reaches the yield criterion of the material, by definition, the tube begins to extrude plastically. Under the pressure of the roller, the tube material flows axially, in both outboard and inboard directions. The tube material at the tube/tubesheet interface is restrained to some degree due to friction. Tube material at the roller/tube interface experiences comparatively less restraint because the rollers apply pressure cyclically as the rollers advance around the tube inner diameter. Additionally, the surface of the rollers is lubricated, reducing the sliding friction. The consequence of the axial extrusion and asymmetry of frictional restraint of tube inside and outside diameters is a distribution of the amount of plastic flow through the tube wall. This is illustrated in Figure 2-7.

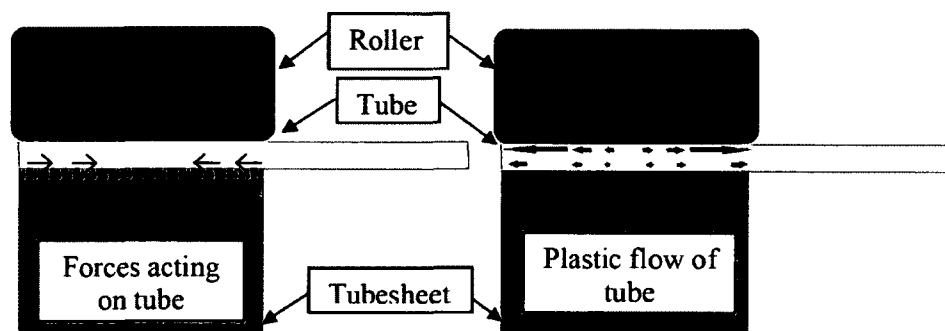


Figure 2-7: Illustration of force on tube and resultant plastic flow

The self-advancing nature of the expander acts to pull the inside diameter surface of the tube. As a consequence, there is more extrusion in the outboard direction than in the

inboard direction. There are three regions of tube material flow; where the net extrusion is outboard, nearly zero, and inboard, are evidenced by the discoloration of the roller following a rolling operation (see Figure 2-8).

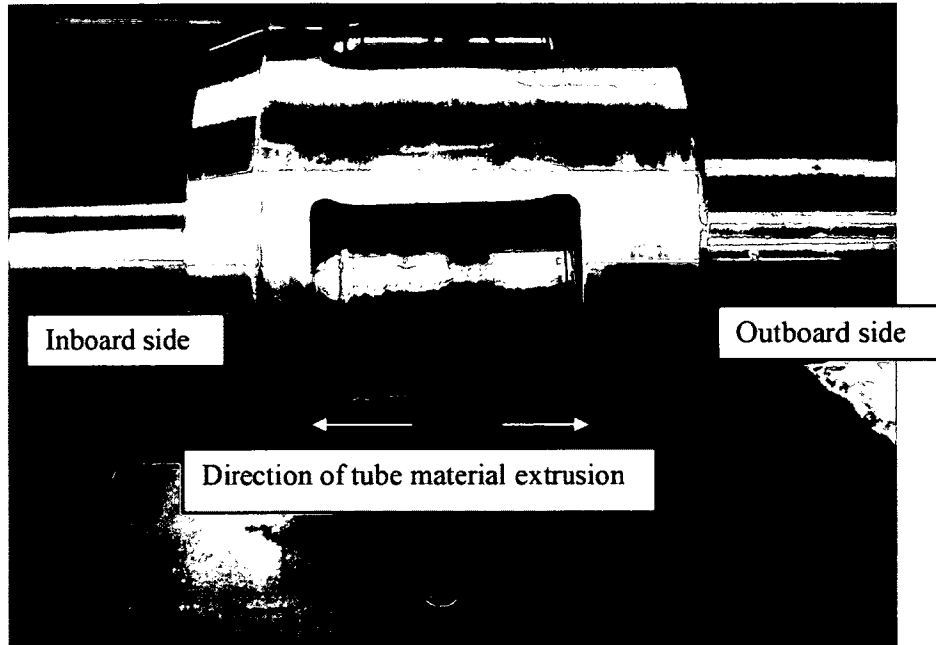


Figure 2-8: Discolored rollers

## 2.7 Analytical Modeling

An analytical model of a rolled joint would be highly desirable as it would allow for detailed optimization of joint properties before committing to an experimental testing campaign. As a result, several attempts have been made to develop an analytical model describing the rolling of a joint. Development of such a model necessitates simplification of some aspects of the joint forming process. Several sets of assumptions have been used to develop such a model with the hope that the particular assumptions and simplifications will only have a minor influence on the joint characteristics. Four noteworthy models are:

- **Nadai Model:** Based on hub of infinite thickness, stress is developed by loading with a uniform pressure where yielding occurs according to the von Mises criterion, and spring-back occurs when the deforming pressure is released [26].
- **Hydrostatic model :** Based on a finite-thickness hub, loading occurs uniformly and yielding occurs according to the Tresca criterion [27].
- **Linning-Hatton Model:** The loading is identical to the Hydrostatic model. Plastic deformation in unloading is accounted for [27].
- **Singh-Soler Model:** Allows for elasto-plastic behaviour at any forming stage, and the large deformation, allows plastic deformation during any stage [27].

The accuracy of these models in predicting interface pressures and residual stresses has been evaluated by comparison with experimental results [27]. The comparison concludes that none of the models mentioned above satisfactorily predicts the interface pressure, pullout strength and residual stresses in the expanded zone. This conclusion leads to the suggestion of finite element modeling as the most promising route to modeling of the joint rolling process. However, the predictions of the Nadai model are useful in developing a conceptual understanding of the joint rolling process. The Nadai model is discussed below, and described in detail in Appendix A.

### **2.7.1 Nadai: Assumptions and Simplifications, and Agreement with Experiment**

Nadai developed an analytical model to predict the interface pressure in formed joints [26]. This model assumes

1. plane strain;
2. no clearance between the tube and tubesheet prior to rolling (i.e. nip-up is not required);
3. uniform loading pressure;
4. perfectly plastic material behaviour;
5. the material yields according to the von Mises criterion; and,

#### 6. isotropic material behavior.

In practice, axial extrusion is observed (step 3 in the rolling process described in Chapter 2), which contradicts the first assumption. Contrary to the second assumption, a nominal clearance exists in practice between the tube and tubesheet bore in order to freely assemble the components prior to rolling. In the case of pressure tubes and calandria tubes, the initial clearances are sufficient to allow for free assembly of joints on both sides of the reactor core (~ 6 m apart). The line contact intrinsic to the roll expansion technique, as discussed in Section 2.1, is ignored from this model. The decidedly anisotropic behaviour of the hexagonally-close-packed (HCP) crystal structure of the zirconium alloys bring into question the simplifications of material behavior resultant from the fourth, fifth, and sixth assumptions. However, the model produces some predictions that help in understanding of the joint forming process.

### 2.7.2 Results and Predictions of the Nadai model

This model allows for a prediction of contact pressure as a function of wall reduction. The limitations of the model, as mentioned in Section 2.7.1, lead to an expectation of experimental results deviating significantly from the prediction. The prediction shown in Figure 2-9 is for the application of this model to the geometry studied in this thesis. However, two particular features seem to fit qualitatively with past experience with joint forming: a steep increase in interface pressure for low wall reductions, and a relatively rapid transition to very little increase in interface pressure resulting from further wall reduction.

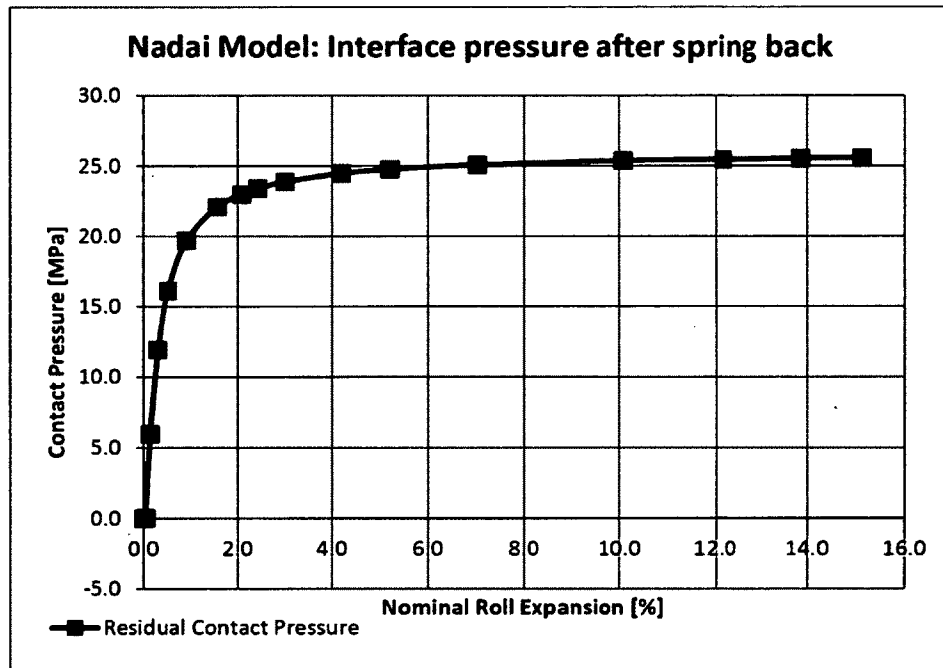


Figure 2-9: Interface pressure vs. wall reduction

### Chapter 3 Calculation of Residual Stresses

Residual stresses are internal elastic stresses that remain within a part after the part has been plastically deformed. Since these residual stresses cannot be measured directly, they are calculated from the strains measured on the release of these stresses. The methodologies used to calculate the stresses from the measured strains in this body of work are adapted from established methods.

Described in this section are the three methods used to calculate stresses in the rolled joint based on the strain measurements described in Section 5.6.

1. The stresses on the surfaces of the tube were calculated directly from the strain gauge measurements. This calculation was performed for the joint disassembly and for the cutting of the freed tube.
2. The interface pressure between the tube and tubesheet plate was calculated based on the strain measured during joint disassembly.
3. The distribution of residual hoop stresses in the tube was calculated for the freed tube using the strains measured during slitting of the freed tube.

These calculations are detailed in the following subsections.

#### 3.1 Surface Stresses on Disassembly of Joint

The change in the stress state of the tube surface can be calculated from the measured strain by the generalized Hooke's law (Equations 3-1 through 3-3) since the tube surface is, by definition, in plane stress [28].

$$\sigma_{zz} = \frac{E}{1 - \nu^2} (\epsilon_{zz} + \nu \cdot \epsilon_{\theta\theta}) \quad (3-1)$$

$$\sigma_{\theta\theta} = \frac{E}{1 - \nu^2} (\epsilon_{\theta\theta} + \nu \cdot \epsilon_{zz}) \quad (3-2)$$

$$\sigma_{\theta z} = G \cdot \epsilon_{\theta z} \quad (3-3)$$

where:  $\sigma_j$  is the stress acting in the  $j$ -direction on the face normal to the  $i$  direction, and

$\epsilon_{ij}$  is the strain in the  $j$  direction of the face normal to the  $i$  direction,

$i$  and  $j$  as placeholders for the  $z$  and  $\theta$  directions above.

$E$  is the Young's Modulus,  $G$  is the shear modulus, and  $\nu$  is the Poisson ratio.

### 3.2 Approximation of Tube / Tubesheet Interface Pressure

The pressure at the interface between the tube and tubesheet of the rolled joint is responsible for the leak tightness of the joint, and as a result it is particularly relevant to joint performance. The interface pressure in this work was calculated by superimposing a pressure on the OD of the tube to produce a strain equivalent to the expansion observed on joint disassembly. The pressure ( $p$ ) required to reverse the diametral expansion was calculated using an analytical relation described in [29]. The formulation is based on thin wall theory, which requires a ratio of tube wall thickness to radius of 10 or more. In the case of the 10mm and 6mm tubes the  $r/t$  ratios are 8.5 and 14, respectively, which introduces a source of error. The relationship is given as Equation 3-4:

$$y = y_A \cdot F_1 + \frac{\psi_A}{2\lambda} F_2 + LT_y \quad (3-4)$$

Here the general geometry is given as Figure 3-1,  $y$  is defined as radial deflection of the tube at location  $x$ , and the following is true:

$$y_A = \frac{-p}{4D\lambda^4} \cdot \frac{2C_2 \cdot C_{a3} - C_4 \cdot C_{a2}}{C_{11}}$$

$$\psi_A = \frac{p}{2D\lambda^3} \left( \frac{C_2 \cdot C_{a3} - C_3 \cdot C_{a2}}{C_{11}} \right)$$

$$LT_y = \frac{-p}{4D\lambda^4} F_{a5}$$

And

$$\lambda = \left[ \frac{3(1-\nu^2)}{r^2 t^2} \right]^{1/4}$$

$$D = \frac{E \cdot t^3}{12(1-\nu^2)}$$

$a$ ,  $l$ ,  $r$ , and  $x$  are geometric parameter defined in Figure 3-1,

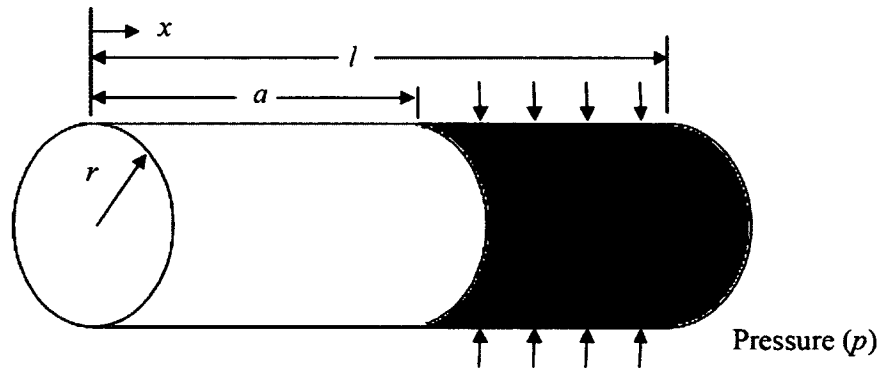


Figure 3-1: Geometry of interface pressure relation

Substituting these into Equation 3-4 gives Equation 3-5:

$$y = \frac{-p}{4D\lambda^4} \frac{(2C_2 \cdot C_{a3} - C_4 \cdot C_{a2})}{C_{11}} F_1 + \frac{p}{2D \cdot \lambda^3 \cdot 2\lambda} \frac{(C_2 \cdot C_{a3} - C_3 \cdot C_{a2})}{C_{11}} F_2 + \frac{-p}{4D\lambda^4} F_{a5} \quad (3-5)$$

where

$$F_{a5} = (x - a)^0 - F_{a1}, \text{ and}$$

$$F_{a1} = (x - a)^0 \cosh \lambda(x - a) \cos \lambda(x - a)$$

Evaluating at locations of  $x$  greater than  $a$  results in

$$F_{a5} = 1 - F_{a1}, \text{ and}$$

$$F_{a1} = \cosh \lambda(x - a) \cdot \cos \lambda(x - a)$$

This substitution into Equation 3-5 gives Equation 3-6:

$$y = \frac{p}{4D\lambda^4} \left( \frac{(C_2 \cdot C_{a3} - C_3 \cdot C_{a2})}{C_{11}} F_2 - \frac{(2C_2 \cdot C_{a3} - C_4 \cdot C_{a2})}{C_{11}} F_1 - (1 - F_{a1}) \right) \quad (3-6)$$

Rewriting Equation 3-6 gives Equation 3-7:

$$y = \frac{p}{4D\lambda^4} \left( \frac{1}{C_{11}} \right) \left( (C_2 \cdot C_{a3} - C_3 \cdot C_{a2}) F_2 - (2C_2 \cdot C_{a3} - C_4 \cdot C_{a2}) F_1 - C_{11} \cdot (1 - F_{a1}) \right) \quad (3-7)$$

where:

$$C_2 = \cosh \lambda(l - a) \cdot \sin \lambda l + \sinh \lambda l \cdot \cos \lambda l$$

$$C_{a3} = \sinh \lambda(l - a) \cdot \sin \lambda(l - a)$$

$$C_4 = \cosh \lambda l \cdot \sin \lambda l - \sinh \lambda l \cdot \cos \lambda l$$

$$C_{a2} = \cosh \lambda(l - a) \cdot \sin \lambda(l - a) + \sinh \lambda(l - a) \cdot \cos \lambda(l - a)$$

$$C_3 = \sinh \lambda l \cdot \sin \lambda l$$

$$C_{11} = (\sinh \lambda l)^2 - (\sin \lambda l)^2$$

$$F_1 = \cosh \lambda x \cdot \cos \lambda x$$

$$F_2 = \cosh \lambda x \cdot \sin \lambda x + \sinh \lambda x \cdot \cos \lambda x$$

Expanding Equation 3-7 gives Equation 3-8:

$$\begin{aligned}
y = \frac{p}{4D\lambda^4} & ((\sinh \lambda l)^2 - (\sin \lambda l)^2)^{-1} \\
& \cdot \left( (\cosh \lambda(l-a) \cdot \sin \lambda l + \sinh \lambda l \cdot \cos \lambda l) \right. \\
& \cdot (\sinh \lambda(l-a) \cdot \sin \lambda(l-a)) - (\sinh \lambda l \cdot \sin \lambda l) \\
& \cdot (\cosh \lambda(l-a) \cdot \sin \lambda(l-a) \\
& + \sinh \lambda(l-a) \cdot \cos \lambda(l-a)) \\
& \cdot (\cosh \lambda x \cdot \sin \lambda x + \sinh \lambda x \cdot \cos \lambda x) \\
& - (2 \cdot (\cosh \lambda(l-a) \cdot \sin \lambda l + \sinh \lambda l \cdot \cos \lambda l) \\
& \cdot (\sinh \lambda(l-a) \cdot \sin \lambda(l-a)) \\
& - (\cosh \lambda l \cdot \sin \lambda l \\
& - \sinh \lambda l \cdot \cos \lambda l)(\cosh \lambda(l-a) \cdot \sin \lambda(l-a) \\
& + \sinh \lambda(l-a) \cdot \cos \lambda(l-a)) \cosh \lambda x \cdot \cos \lambda x \\
& - ((\sinh \lambda l)^2 - (\sin \lambda l)^2) \\
& \left. \cdot (1 - \cosh \lambda(x-a) \cdot \cos \lambda(x-a)) \right) \tag{3-8}
\end{aligned}$$

Grouping the trigonometric terms in Equation 3-7 together as the term " $b^{-1}$ " gives Equation 3-9:

$$y = \frac{p}{4D\lambda^4} b^{-1} \tag{3-9}$$

Expanding Equation 3-9 gives Equation 3-10:

$$y = \frac{p}{4 \frac{Et^3}{12(1-\nu^2)} \left[ \frac{3(1-\nu^2)}{r^2 t^2} \right] b} \tag{3-10}$$

which can be simplified to Equation 3-11 and rewritten as Equation 3-12:

$$y = \frac{p \cdot r^2}{E \cdot t \cdot b} \quad (3-11)$$

$$p = \frac{y \cdot t}{r^2} \cdot b \quad (3-12)$$

As a first approximation, Equation 3-12 reveals that the interface pressure ( $p$ ) is proportional to the radial deflection of the tube ( $y$ ) and the tube wall thickness ( $t$ ), and inversely proportional to the square of the tube radius ( $r$ ).

It should be noted that this relation assumes the interface pressure ( $p$ ) is uniform over the entire interface area. Since the interface pressure along the length is not necessarily uniform in this case, this prediction is considered to be only an approximation of the interface pressure. The calculation of interface pressure was performed using an Excel<sup>®</sup> spreadsheet, solving numerically for interface pressure using the GoalSeek function in Microsoft Excel<sup>®9</sup> (see Appendix B for more details). This calculation was performed using the hoop strain measured at the A1 and B2 locations of the tube (see Figure 5-12).

### 3.3 Calculation of the Average Stresses from Cutting

The change in stress at the tube surface resulting from cutting through the tube can be calculated using the generalized Hooke's Law described in Section 3.1. These average stresses are useful to consider in combination with the stress distributions calculated by the crack compliance method (discussed in Section 3.4) because the stresses in the near surface regions of the tube are inaccurately described by the crack compliance method.

---

<sup>9</sup> GoalSeek is a numerical solver function built-in to Microsoft Excel 2007.

### 3.4 Calculation of the Stress Distribution: The Crack Compliance Method

The technique used in this work to determine the distribution of residual hoop stresses through the tube wall thickness is the crack compliance method. The method was first introduced by Vaidyanathan and Finnie in 1971, and has subsequently been improved upon and applied to many geometries [11].

The crack compliance method of determining these stresses is based on the principle of elastic superposition (illustrated in Figure 3-2). It is assumed that the process of releasing the elastic stresses in any one area does not cause further plastic deformation in another area. Considering a body with a distribution of residual stresses, if a cut is introduced into the body such that residual stresses are released, then the body will deform. By the principle of superposition, a theoretical pressure applied to the cut face that exactly reverses this measured deformation is equivalent to the stresses released on introduction of the cut. This phenomenon is only true if the stresses remain elastic everywhere during the stress release and subsequent reversal of the deformation.

An equivalent framing of the superposition principle is to consider two bodies, say bodies A and B, that are identical except that A has residual stresses, while B does not. On cutting of body A, it deforms in some way due to the residual stresses. Since no residual stresses are present in body B, no deformation occurs when it is cut. However, there exists a pressure distribution that if applied to the cut face of body B will result in an identical deformation to that observed in body A. This pressure is exactly the opposite of the stresses released in cutting body A.

To determine this pressure, and hence the residual stress, it is assumed that the stress distribution can be represented as a linear combination of polynomials (Equation 3-13).

$$\sigma_{xx}(y) = \sum_{i=0}^n A_i P_i(y) = \bar{P}\bar{A} \quad (3-13)$$

where  $n$  is an integer,  $n+1$  is the total number of polynomials used in the summation,  $\bar{P}$  is the vector of  $n+1$  polynomials,  $P_i(y)$  is the  $i$ th polynomial,  $\sigma_{xx}(y)$  is the function of stresses acting in the  $x$ -direction on the cut face normal to the  $x$ -direction. This function is assumed to be continuous in the  $y$ -direction (cut depth direction); and  $A_j$  is the coefficient of the  $j$ th polynomial in the linear combination, and  $\bar{A}$  is the vector of  $n+1$  coefficients. In the set of functions used,  $j$  denotes the order of the polynomial.

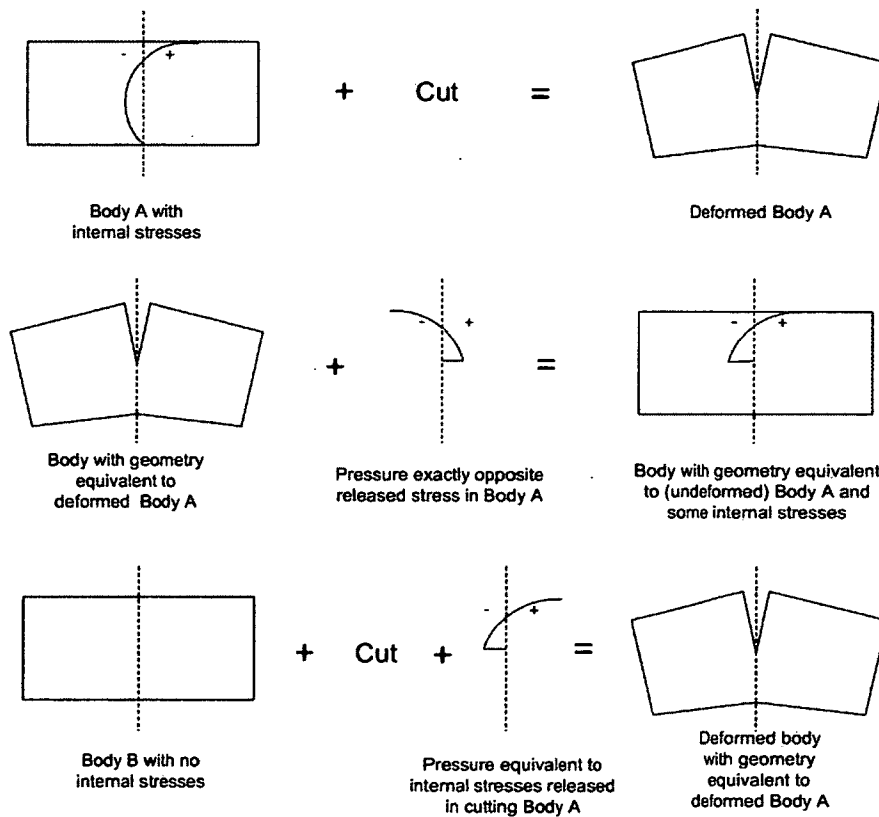


Figure 3-2: Illustration of the principle of superposition<sup>10</sup>

<sup>10</sup>Adapted from Figure 3 in [11].

The crack compliance method is implemented through the following steps:

1. Quantification of the deformation via strain measurements on cutting of a part with residual stresses (i.e., body A).
2. Determination of the deformation of an identical unstressed body (i.e., body B) under a series of known load distributions, i.e., the shifted Legendre polynomials. This step is known as the forward solution.
3. Calculating the best-fit for a linear combination of the deformations under the known loads from step 2 to the deformation of body A quantified in step 1. This step is achieved through a least squares fit solved via matrix inversion and is known as the inverse solution.

These steps are described in more detail in the following subsections.

### 3.4.1 The Forward Solution for the Crack Compliance Technique

The intention of the forward solution is to determine the “compliance” of the structure, or the relation between known applied loads on the cut face and the deformation of the body. The deformation of the body is quantified by the strain as measured in a specific direction and at a specific location. The compliance of the structure is defined by the compliance matrix ( $\bar{C}$ ) as a representation of the response of the body to each of the polynomials, at each successive cut depth. The compliance matrix is populated by rows of the strain response at specific cut depths and columns of different load functions, as shown in Equation 3-14.

$$\bar{C} = \begin{bmatrix} c_{11} & \cdots & c_{1n+1} \\ \vdots & \ddots & \vdots \\ c_{i1} & \cdots & c_{in+1} \end{bmatrix} \quad (3-14)$$

Where  $i$  is the number of cuts through the tube thickness; and  $n+1$  is the number of polynomials to be used in fitting.

With the stress in the part defined as a linear combination of polynomials up to order  $n$  (by Equation 3-13), the strain resulting from the progression of the cut is a linear combination of the compliances, as shown in Equation 3-15.

$$\varepsilon_x(y) = \sum_{i=1}^n A_i C_i(y) = \bar{C} \bar{A} \quad (3-15)$$

where:

- $\varepsilon_x$  is the strain in the part as measured in the x-direction for a given cut depth,  $y$ .
- $\bar{C}$  is the compliance matrix (Equation 3-14), and
- $\bar{A}$  is the same set of coefficients used in Equation 3-13.

The response of the part to each of the loading cases making up the compliance matrix can be determined with a variety of methods [11]. In this study, a 2D finite element analysis (FEA) was used to determine the strain response.

The shifted Legendre polynomials were chosen as the set of functions to fit to the stress distribution because they have been used successfully in other applications of the technique [11] [12]. This set of polynomials has the property that the 1<sup>st</sup> order and higher polynomials satisfy force equilibrium conditions and the 2<sup>nd</sup> order and higher polynomials satisfy moment equilibrium conditions [11]. Depending on the geometry, the 0<sup>th</sup> and 1<sup>st</sup> order polynomials are sometimes omitted. In the case of the ring geometry, the force equilibrium must be satisfied because of symmetry, meaning the 0<sup>th</sup> order polynomial could be omitted. In contrast, the moment equilibrium is not necessarily satisfied, meaning that the 1<sup>st</sup> order polynomial must be included. For the forward solution, both the 0<sup>th</sup> and 1<sup>st</sup> order terms were included. Including the 0<sup>th</sup> term serves as a means to identify errors with the fit since this term should be (close to) zero in the final solution. The first 11 polynomials (0<sup>th</sup> through 10<sup>th</sup> order) are shown in Figure 3-3 with cut depth normalized to the part thickness. Typically 3 to 9 polynomial terms are used with this technique to fit a distribution [11] [30] [31]. Since fits up to 10<sup>th</sup> order were

generated, the optimal fit is expected to be within this set . It is assumed that the actual stress distribution can be expressed as a linear combination of the chosen polynomials.

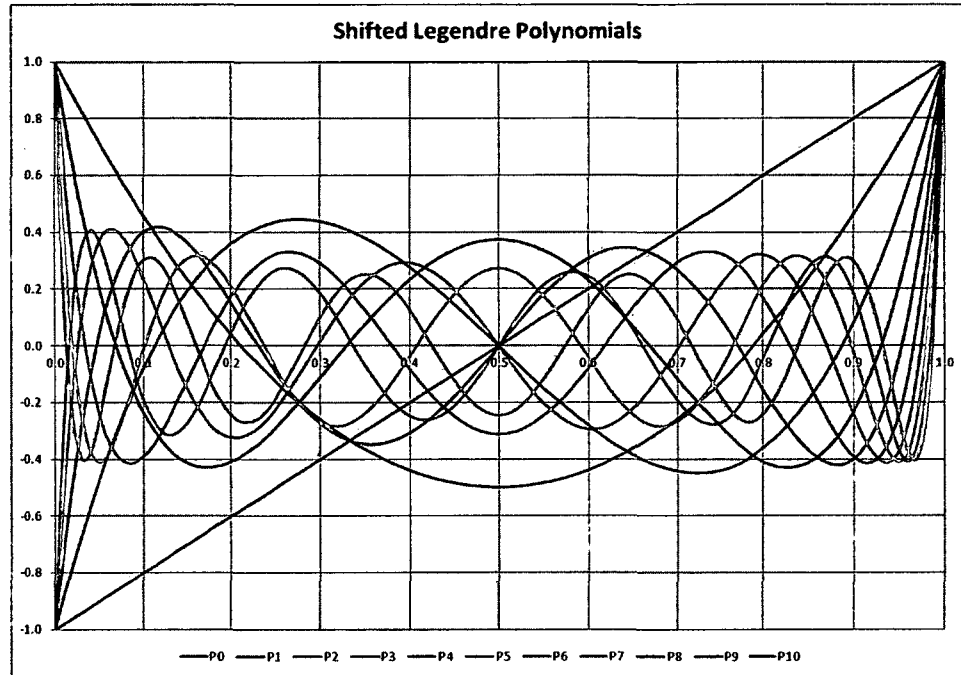


Figure 3-3: The shifted Legendre polynomials

### 3.4.2 The Inverse Solution for the Crack Compliance Technique

The inverse solution is the determination of the coefficients defining the contribution of each load function to the linear combination (i.e., the  $\bar{A}$  vector defined in Equation 3-13). Once the coefficients are known, the equation corresponding to that stress distribution is generated by summing the functions in the solution set, each scaled by their respective coefficient (Equation 3-13).

The  $\bar{A}$  vector is determined in the following manner. The strain at any cut depth ( $y$ ) is approximated by expansion of the series in Equation 3-15. A least-squares fit is obtained, minimizing the square of the offset between the measured and approximated strains at each of the cut depths where strain was measured. The matrix notation of the solution for the  $\bar{A}$  vector is shown in Equation 3-16.

$$\bar{A} = (\bar{C}^T \bar{C})^{-1} \bar{C}^T \bar{\epsilon}_{measured} \quad (3-16)$$

where  $\bar{C}$  is the compliance matrix, T denotes the transpose of the matrix, and

$\bar{\epsilon}_{measured}$  is the vector of strains measured on cutting of the specimen (discussed in more detail in Section 5.6.2).

## Chapter 4 Implementation of the Crack Compliance Technique

The following subsections detail the implementation of the crack compliance technique for calculation of residual stresses discussed in Chapter 3.

### 4.1 Computing the Forward Solution: Finite Element Analysis

Chapter 3 introduced the concept of the compliance matrix in which each of the entries in the compliance matrix (Equation 3-14) represents the strain response to one of a set of polynomials (see Section 3.4.1). In this thesis, the strain response was determined by simulating each case using finite element analysis (FEA), evaluated using ANSYS<sup>®11</sup>. The FEA is based on a 2D plane strain model of the tube section at the particular axial location where the strain gauge is located. The simplification of this 3D geometry as with a 2D model introduces a source of error. The plane strain simplification was chosen over plane stress because the tube is long relative to the wall thickness and previous work has assumed that the deformation remains in-plane, (i.e., plane strain) [20]. However, experimental measurements of the axial strain (see Section 6.3.1) indicate that this simplification may be an oversimplification and result in error in the calculated stress distribution.

The FEA model used to compute the compliance of the tubes was simplified to include only half of the tube section to take advantage of symmetry, as shown in Figure 4-1. The model was constrained using symmetric restraint to displacement normal to the surfaces that represent the plane of symmetry. The polynomials in Figure 3-3 were discretized and the load was applied to the cut face; the ANSYS<sup>®</sup> software interpolated between the discrete values. To minimize error resulting from the discretization, 15,000 points were used. The slot was approximated as a square bottomed slot. This approximation overestimates the strain slightly for a given pressure on the cut face, as compared to a round

---

<sup>11</sup>ANSYS Release 6.1SP, licensed to AECL, is a commercially available FEA software package.

bottom slot [32]. Since this overestimate is expected to be small, it was ignored in this thesis.

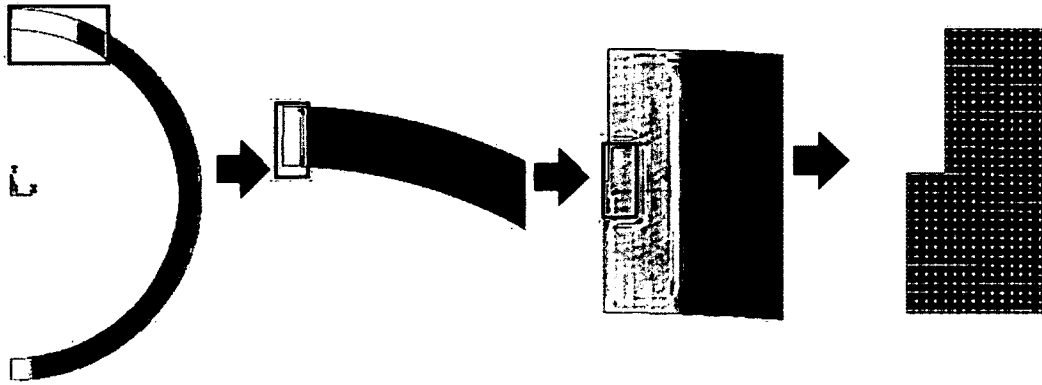


**Figure 4-1: Meshed geometry shown with a cut midway through the wall thickness**

The strain on the tube surface is a function of position<sup>12</sup>. As a result, the compliance of the tube is specific to a particular distance from edge of the cut. Experimentally, the distance from each gauge to the cut edge was measured following cutting of the tube<sup>13</sup> and is summarized in Appendix C. The compliance corresponding to each gauge location and each tube (post-release) wall thickness was generated. As an example, the compliances corresponding to the outside and inside diameter gauges at the bore midpoint for tube 10mm-8.3%WR<sup>14</sup> are shown in Figure 4-2 and Figure 4-3, respectively.

---

<sup>12</sup> Strain gauge placement is discussed in more detail in Section 4.3.

<sup>13</sup> Cutting of the tubes is discussed in more detail in Section 5.6.2.

<sup>14</sup> Tubes are designated with a label of the format: XXmm-Y.Y%WR indicating the tube wall thickness (XX mm), and the percent wall reduction (Y.Y%WR).

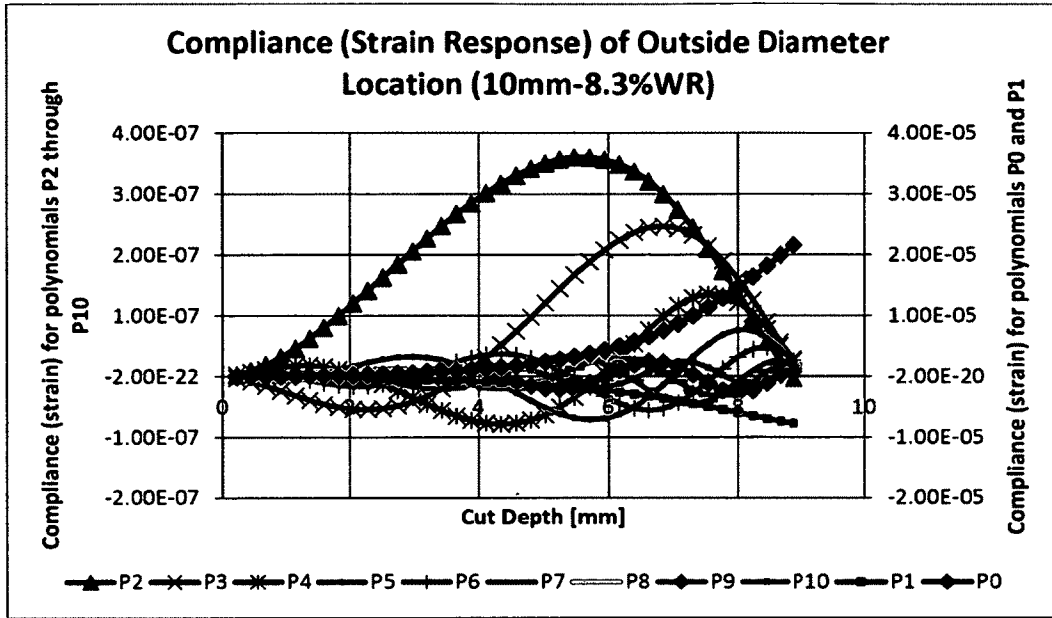


Figure 4-2: Example of compliance of outside diameter gauge

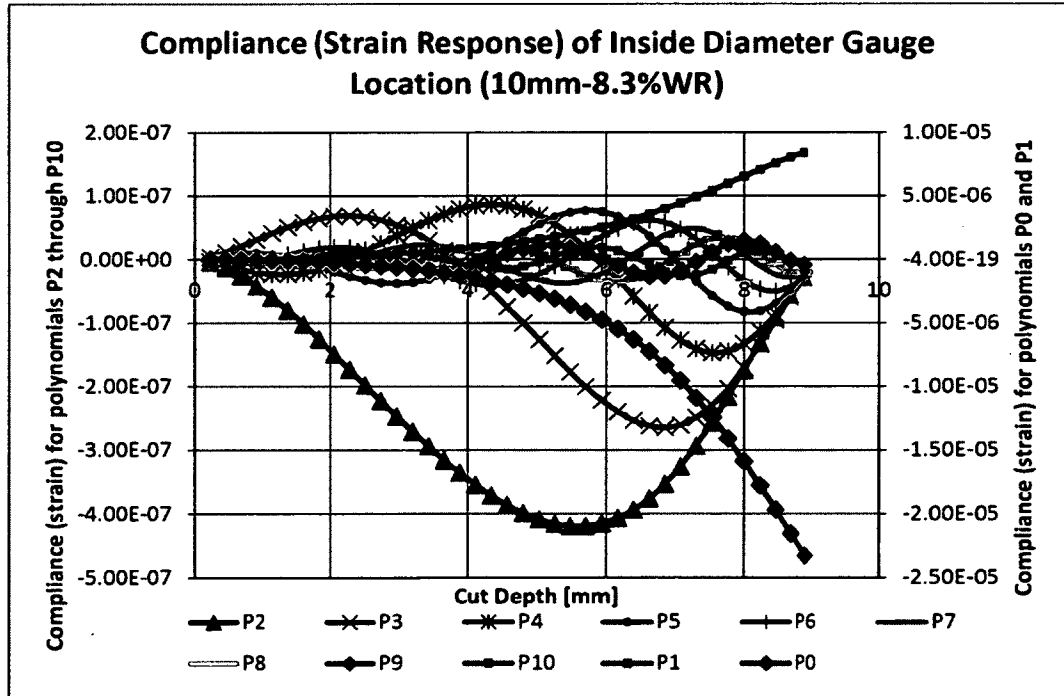


Figure 4-3: Example of inside diameter gauge compliance

#### 4.1.1 Automation of Compliances Computation

Since a large number of separate analyses were required to populate the compliance matrices (10 functions times up to 40 cuts = up to 400 simulations per geometry), a program was written using ANSYS® Parametric Design Language (APDL) to generate the geometries of each successive cut depth and to apply each of the 11 functions (0<sup>th</sup> through 10<sup>th</sup> order) to the cut face. The program was written to define the geometry parametrically to allow for it to be scaled. The final dimensions of each tube were used. Eight node quadrilateral elements and six node triangular elements were used to mesh the geometry. The mesh density was scaled with the finest mesh at the cut face and symmetry boundaries. The element size at these locations was about 0.13 mm.

#### 4.2 Implementation of the Inverse Solution

The matrix operations required to evaluate Equation (3-16) were performed in MATLAB® using a program prepared by Prime at the Los Alamos National Laboratory [31] [33]. The program reads in one input file containing the compliances (the C matrix), a second input file containing a list of corresponding cut depths, and a third input file containing the “measured”<sup>15</sup> strains. The tube wall thickness and Young’s modulus are entered along with the range of the orders of polynomials used to generate the input compliance matrix (i.e. inclusion of 0<sup>th</sup> and 1<sup>st</sup> order terms, and the maximum order used). Execution of the program calculates the  $\bar{A}$  vector (the coefficients for the summation of the Legendre polynomials) corresponding to the best-fit to the measured strain data, and corresponding stress at each cut depth by Equation 3-13. The output is a matrix of the calculated stress with columns representing the stress (i.e.  $\sigma_{xx}(y)$ ) for

---

<sup>15</sup> For the purpose of validation discussed in Section 4.4.2, the “measured” strains were replaced with strains from simulated deformation.

increasing order of polynomials included in the fit, and rows representing each discrete cut depth ( $y$  in Figure 4-4).

### 4.3 Strain Measurements

At the core of the crack compliance technique are the measured hoop strains. The details of the strain gauging are presented in Section 5.6. As the cut through the wall progresses, the two cut faces produced are normal to the circumferential direction. Three stresses are released on the cut face: normal stress in the hoop ( $\theta$ ) direction, shear stress in the axial ( $z$ ) direction, and shear stress in the radial ( $r$ ) direction. Strain is measured experimentally in three directions at two axial locations. The gauges oriented in the hoop direction measure total strain in the hoop direction, i.e. the sum of the strain in the hoop direction resultant from released stresses in the hoop direction as well as the strain resultant from the shear stresses released. The strain measurements in the axial and 45 degree directions were not used in the crack compliance technique.

The number of cuts taken through the tube wall thickness determines the upper limit on the spatial resolution of the stress distribution. The cut increment was chosen to produce approximately 40 cuts (0.229 mm and 0.152 mm in the case of the 10 mm and 6 mm tube walls, respectively). While the WEDM is capable of much smaller cut increments, the change in strain must be measurable and significant [11]. The strain measurements showed very little change in very shallow cuts (shown in Figure 4-2 and Figure 4-3. As a result, the first 4 cuts ( $\sim 1$  mm) of wall thickness were grouped into a single cut for calculation purposes.

### 4.4 Validation of the Implementation of the Crack Compliance Technique

The two main approaches to develop confidence in the results obtained through the crack compliance technique are validating the forward solution, and validating the complete computation. To validate the complete computation the deformation of the tube

geometry was simulated under the application of an arbitrary pressure on the cut face using the FEA model used for the forward solution, described in Section 4.1. The resultant deformation, as quantified by the strain at the location of the strain gauges was used in place of experimentally obtained strains. Since the input function should exactly match with the predicted stress distribution obtained with the crack compliance method the overall implementation can be checked. This check was performed for two trigonometric functions. The limits of the technique were also explored by using two particularly severe “arbitrary” input functions: a step function and a square wave. The validation steps and testing of the limits of the method are discussed in the subsections that follow.

#### 4.4.1 Validation of the Forward Solution

Confidence in the forward solution was developed through incremental development of the FEA model. First, the implementation of the forward solution was checked for the case of a simple rectangular beam, illustrated in Figure 4-4, for which published data was available [34].

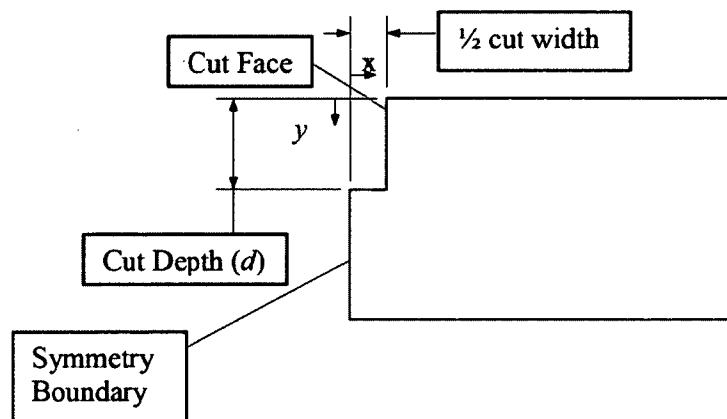
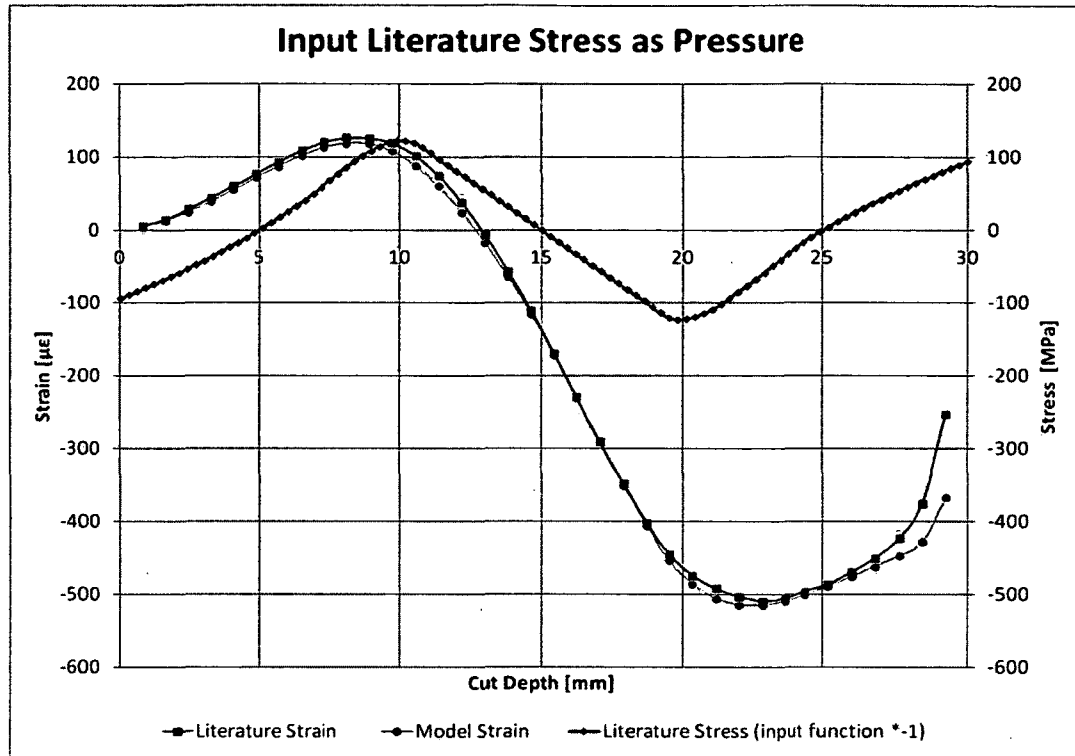


Figure 4-4: Geometry of beam model

This informal checking was invaluable in quickly identifying errors in the code during development. One particular point highlighted at this stage was with regard to the sign of the calculated pressure. Since the applied load is a pressure and the applied result is a stress, the sign of the calculated stress must be reversed because a pressure (positive in sign) applied to the cut face is equivalent to imposing a compressive stress (negative in sign). The final output of this method is therefore, the residual stress in the part and not the stress released.

The published data [33] provided a test case for which both the residual stress released and the measured strain corresponding to the deformation are known. The behaviour of the model was confirmed by inputting the known stress as a pressure (with the sign reversed), and comparing the strains calculated by the model against the published strains, as shown in Figure 4-5. The comparison reveals that the model behaves similarly to the published experimental data for most cut depths, but begins to deviate at the deepest cut depths beyond a cut depth of about 27 mm (of the total 30 mm section depth). This deviation is thought to be of little significance since the remaining ligament is very small; however, it indicates a limitation of this method of computing the forward solution.



**Figure 4-5: Simulated strain as compared published values for a rectangular beam [34]**

The model geometry was then changed to the ring geometry, similar to Figure 4-1, and representative of the tube used in the experiment. A mesh sensitivity analysis was performed to confirm that the results obtained were independent of the meshing scheme used. The symmetry boundaries and the cut face boundary were assumed to be the regions requiring the finest meshing. The meshing of the model was such that the mesh sizing was scaled by a single (arbitrary) parameter. The meshes were compared to one another using the 10<sup>th</sup> order Legendre polynomial (see Figure 3-3) and by looking at the deep cuts into the ring (four cut depths ranging from 4.5 to 7.7 mm deep). The quantity referred to as the “mesh size” is the size of the elements in the finest meshed area. The mesh independence was confirmed by comparing the strains predicted by successively finer meshed models loaded with the same load. As shown in Figure 4-6, the strains

appear to converge as the mesh size is decreased. A mesh size <sup>16</sup> of 0.25 was chosen because little change is evident in refining the mesh beyond that mesh size, as well as considerations for computation time to evaluate all test cases<sup>17</sup>.

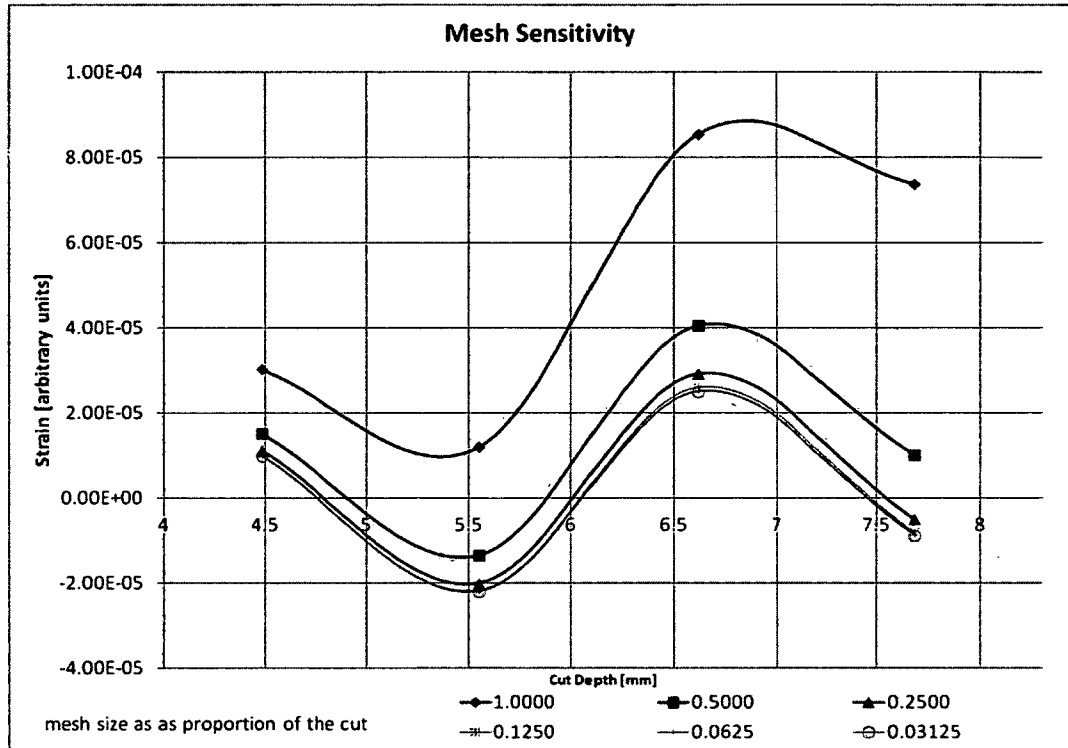


**Figure 4-6: Variation in strain response of the FEA model to various mesh densities**

<sup>16</sup> The mesh size is defined in units of the modeled cut width (half of the actual cut width). A mesh size of 0.25 corresponds to 4 elements per half cut width, or 8 elements per cut width.

<sup>17</sup> To generate the compliance matrices the finite element model had to be evaluated once for each polynomial at each cut depth for each tube (approx.  $11 \cdot 40 \cdot 4 = 1760$  times).

#### 4.4.2 Validation of the Implementation of the Crack Compliance Method

The second validation step was developed to confirm that the overall method, including the forward solution using the ring geometry and the inverse solution, was correctly implemented. First, the forward solution was evaluated to generate the compliance matrix. Second, an arbitrary function was defined, referred to as the “input function”. The forward solution model, described in detail in Section 4.1, was used to simulate the deformation of the ring geometry, as quantified by the strain, under the loading of the input function. Using the simulated strains in place of measured strains, the inverse solution was then evaluated to predict the stress released. Since the calculated stress should exactly match the input function, the implementation of the technique can be verified.

The results of the two input functions ( $\sin(y)$  and  $\cos(y)$ ) used to validate the application of the computation are plotted in Figure 4-7 and Figure 4-8. Each series shown represents the best fit polynomial to the data and is a linear combination of the Legendre polynomials, with terms up to the 5<sup>th</sup> order. In both cases, the stress prediction improves with increasing order of the polynomial. The predicted stress closely matches the input function using 5<sup>th</sup> order and higher polynomials. Since both ANSYS<sup>®</sup> and MATLAB<sup>®</sup> handle the calculations without units, this validation also confirms that the units of the two validation steps (the scaling in ANSYS<sup>®</sup>, and the scaling in MATLAB<sup>®</sup>) are self-consistent.

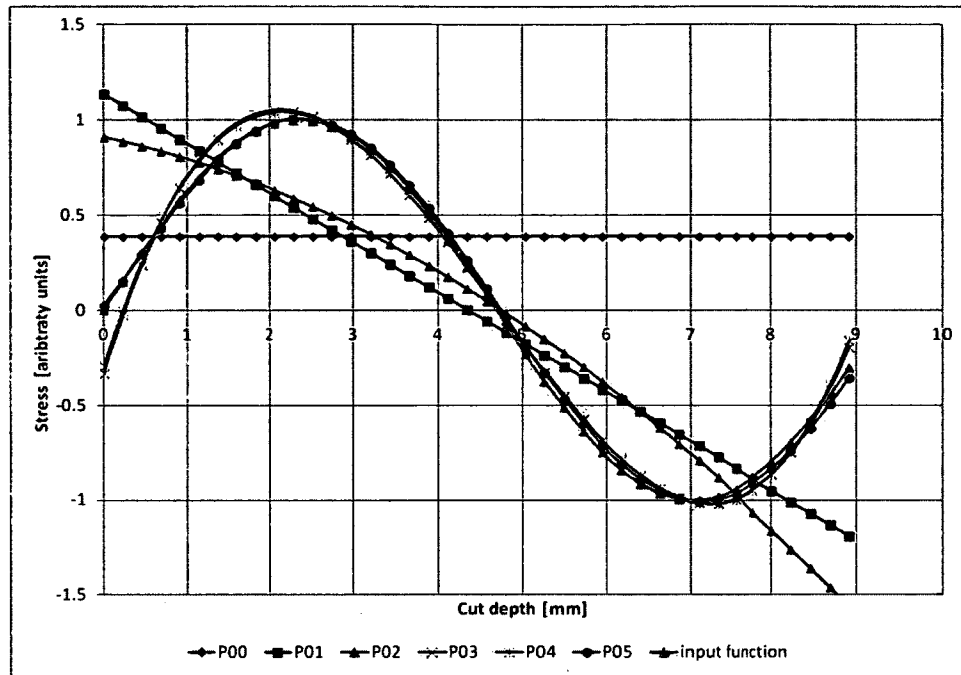


**Figure 4-7: Function  $\sin(y)$  validating the implementation of the crack compliance technique**

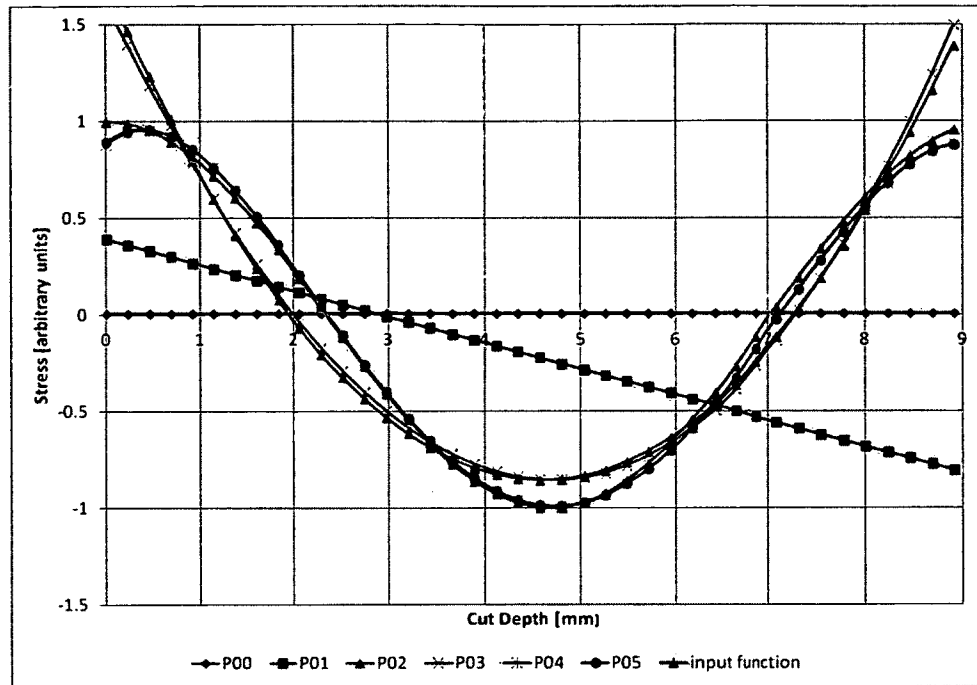


**Figure 4-8: Function  $\cos(y)$  validating the implementation of the crack compliance technique**

#### 4.4.3 Testing the Limits of the Crack Compliance Technique

As previously mentioned, the accuracy of the stress predicted with the crack compliance technique is limited by how accurately the function can be represented by a linear combination of, in this case, the Legendre polynomials used. Using the technique discussed in Section 4.4.2, several “arbitrary” functions were tested to provide insight into the accuracy of the technique for each order of polynomial. The functions represented distributions ill-suited to fitting with a series of continuous polynomials. The response to a step function is plotted in Figure 4-9 for all orders of polynomial and with an alternate presentation in Figure 4-10. The general trend of the prediction is visible for polynomials above the 3<sup>rd</sup> order and, as expected, the accuracy of the prediction improves with increasing order of the polynomial. The deviation from the input function is largest

near the surfaces and near the locations of steepest change. Within about 1 mm from the starting surface, and about 0.5 mm from completing the through cut, the predictions are generally inaccurate.

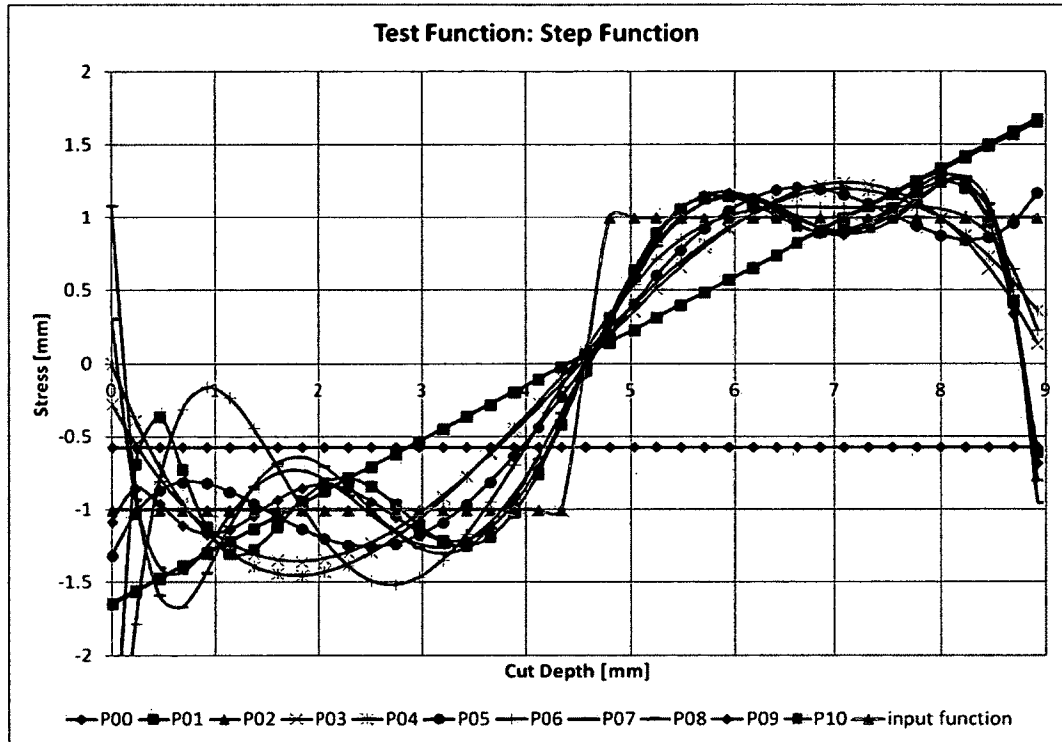


Figure 4-9: Polynomial fits to step function input

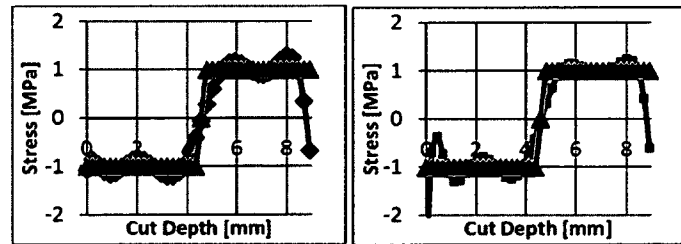
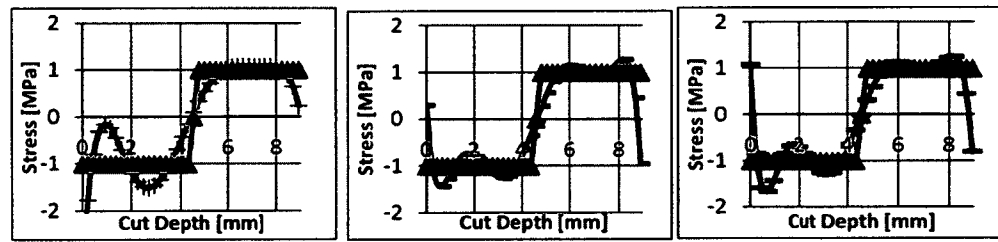
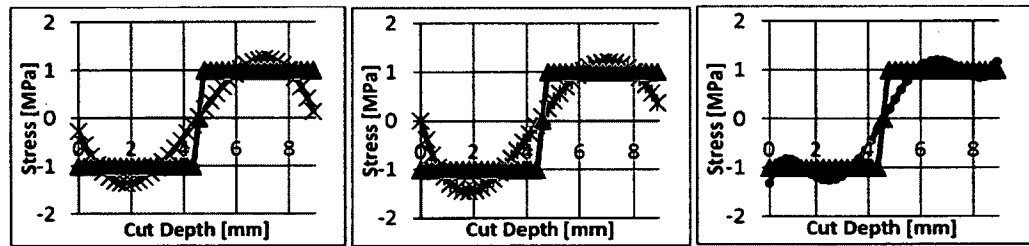
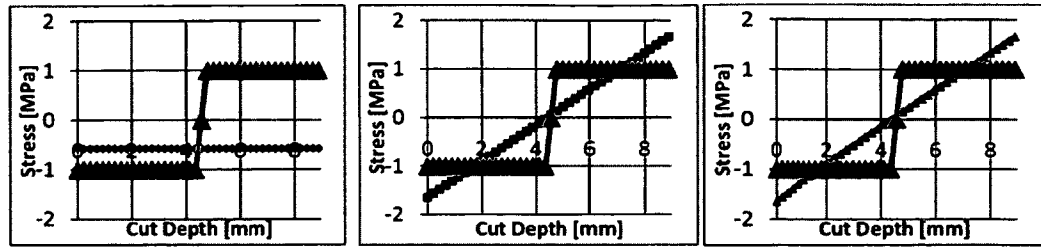


Figure 4-10: Individual polynomial fits to step function input (Alternate presentation to Figure 4-9)

A square wave input function was tested, as shown in Figure 4-11 and with an alternate presentation in Figure 4-12. The predictions are largely inaccurate near both surfaces. There are 7 inflection points<sup>18</sup> in the input function, and the polynomial of tenth order shows reasonable agreement at points between about 1.5 mm from the surface of the cut, and about 0.8 mm from completing the through cut. The inaccuracies near the surfaces suggest that the stress predictions near the surface should be excluded from the analysis. Additionally, relatively sharp changes in the predicted stress are indicative of locations of higher uncertainty in the predicted stress. The appropriate order of fit cannot be directly extrapolated from the case of the square wave since the nature of the distribution of the experimental data in the present work is unknown. However, the continuous nature of the geometry and loading makes it unlikely that the stress distribution in the present experimental work contains changes as drastic as the step functions.

---

<sup>18</sup> Technically the input function does not have inflection points because the derivative is discontinuous. However, a polynomial equivalent would have 7 or more inflection points.

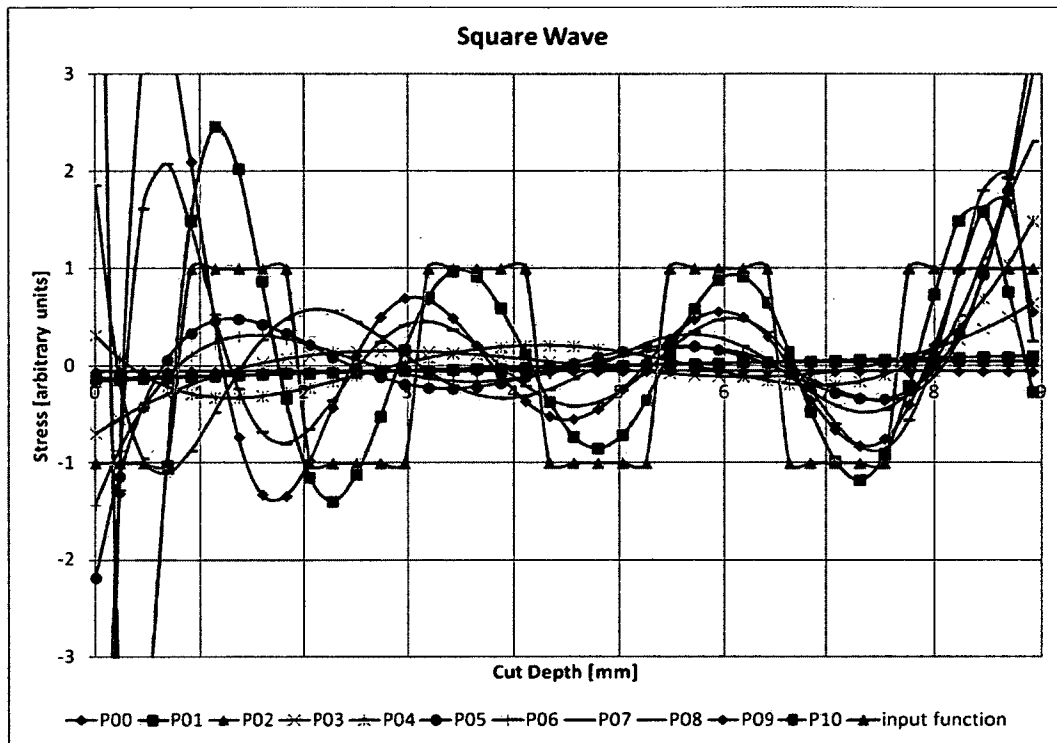


Figure 4-11: Polynomial fits to square wave input

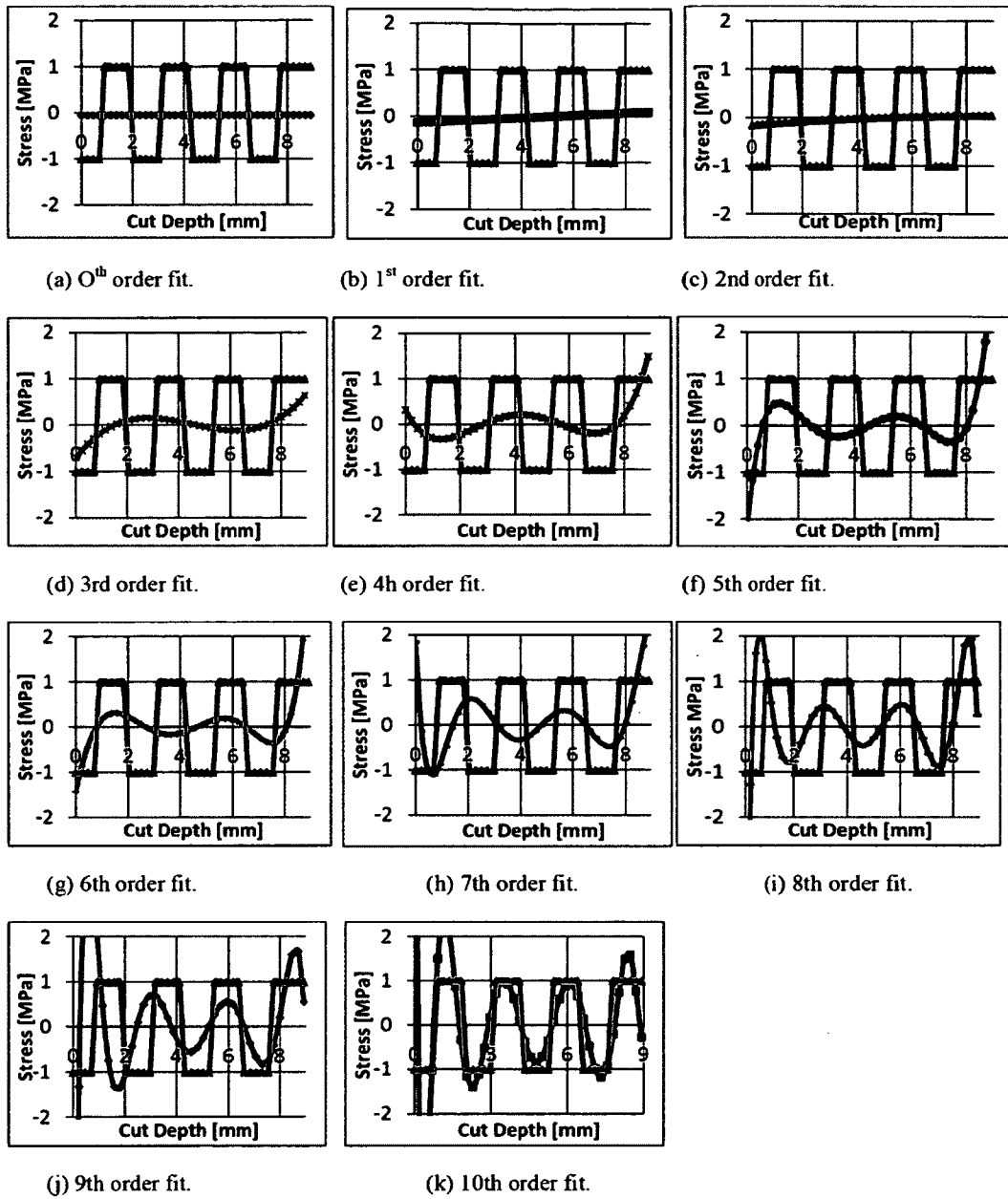


Figure 4-12: Individual polynomial fits to square wave input (Alternate presentation of Figure 4-11)

#### **4.4.4 Summary of the Validation**

In summary, the application of the crack compliance technique to tubes formed into rolled joints has been implemented. The two validation steps described above performed provide confidence that the calculation has been implemented correctly.

#### **4.4.5 Limitations of the Crack Compliance Method**

The crack compliance technique can be used to provide useful information about the stress state of the tube in a rolled joint. However, it is subject to several limitations. Firstly, the compliance is calculated for the introduction of a single slot in the tube. It is assumed that the stress distribution in the tube is perfectly axisymmetric, making the circumferential location of this slot irrelevant. However, previous experimental work on rolling has demonstrated that the stress at the tube surface is non-uniform around the circumference [35]. Secondly, the use of a 2D finite element model, as described in Section 4.1, to determine the compliances (Equation 3-12) implies that 3D effects, such as the release of shear stresses, are ignored. Thirdly, the technique requires the deformations on incremental extension of the slit must remain elastic everywhere.

## **Chapter 5 Experimental Setup and Procedure**

Within this chapter is an explanation of the experimental setup and procedure. The setup and procedure for forming the roll-expanded joints is largely based on previous rolled joint work [36]. The joint disassembly is novel as is the setup and procedure for tube cutting and collection of strain data.

### **5.1 Experimental Procedure**

The experimental work consisted of forming and testing tube to tubesheet rolled joints similar in geometry to proposed concepts for Gen-IV fuel channels. The large diameter (155 mm inside diameter) tubes allowed for the use of existing joint forming equipment including a roll expansion tool. Strain gauges were installed on the tube inside diameter. The joint was disassembled and the strains corresponding to the release of the restraint of the tubesheet plate were measured. Additional gauges were then applied to the outside of the tube. The tube was cut with a wire electrical discharge machining (WEDM) operation, with the axis of the wire parallel to the axis of the tube resulting in an axial cut that progressed from the outside diameter inwards. The cut was made in small increments at which strain measurements were taken.

### **5.2 Experimental Setup**

The following subsections detail the components of the test pieces as well as the equipment and fixturing used.

#### **5.2.1 Test Pieces**

The test pieces were designed to simulate a tube rolled into a calandria tubesheet plate. The joint consists of a split tubesheet plate and a corresponding tube. In the case of calandria tubes, the tubesheet plate represents the calandria tubesheet; in the case of pressure tubes, this tubesheet plate represents the end fitting. These components are described in the following subsections.

### 5.2.2 Specifications of Tube Specimens

The tubes used were of two geometries differing in wall thickness (10 mm and 6 mm), both with an inside diameter of 153 mm and an overall length of 90 mm. The details of the two tube geometries are shown in Figure 5-1 and Figure 5-2. The tubes were fabricated from Ampco<sup>®</sup> 18, an aluminium bronze, and were stress relieved prior to finish machining<sup>19</sup>. Ampco<sup>®</sup> 18 was chosen for the tube material because the Young's modulus and yield strength are similar to those of zircaloy alloys used in CANDU<sup>®</sup> reactors (and Gen-IV concepts), and the material was readily available. The basic mechanical properties of Ampco<sup>®</sup> 18 and 304 stainless steel, the material used for the tubesheet, are presented in Table 5-1. However, the anisotropy of the zirconium alloys resultant from the HCP crystal structure is a distinct difference between the tubes tested and those used in CANDU<sup>®</sup> reactors. The orientation of the HCP structure in zircaloy tubes is aligned in the tubes such that both the yield strength and Young's modulus are higher in the transverse direction, as compared to the longitudinal direction [4]. Based on previous experience with roll expansion of Ampco<sup>®</sup> 18 and zircaloy tubes, this thesis assumes that the results obtained are applicable to zirconium alloys regardless of these differences. The thick-walled tubes (10 mm and 6 mm) were chosen as good candidates for application of the crack compliance technique because they allow for a large number of cuts (>30) through the tube wall. The resolution of the stress prediction improves with increased number of cuts, and the accuracy improves with increasing cut increment.

---

<sup>19</sup> The tubes were stress relieved by heating at 400°F for 4 hours. They were air cooled prior to finish machining. The residual stresses resulting from the finish machining operation are assumed to be small relative to the stresses imparted in the nip-up operation of rolling.

**Table 5-1: Mechanical material properties of tubes and tubesheet plates**

Material	Young's Modulus [GPa]	Yield Strength (min) [MPa]	Poisson's Ratio
Ampco® 18	110	205	0.316
304 stainless steel	193	240	0.28

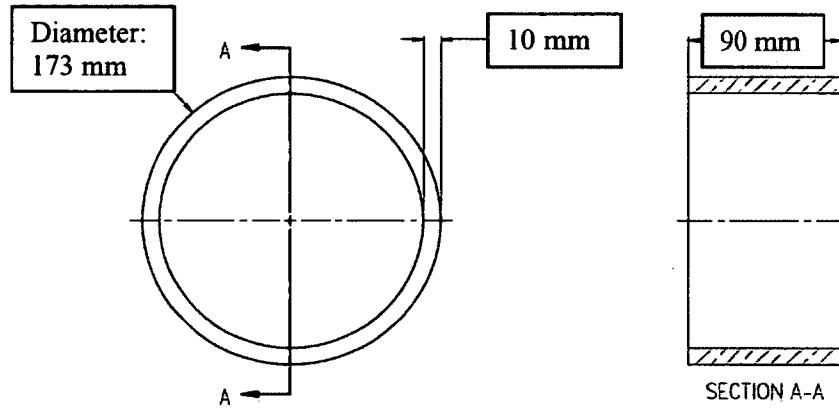


**Figure 5-1: Tube details (10 mm wall)**

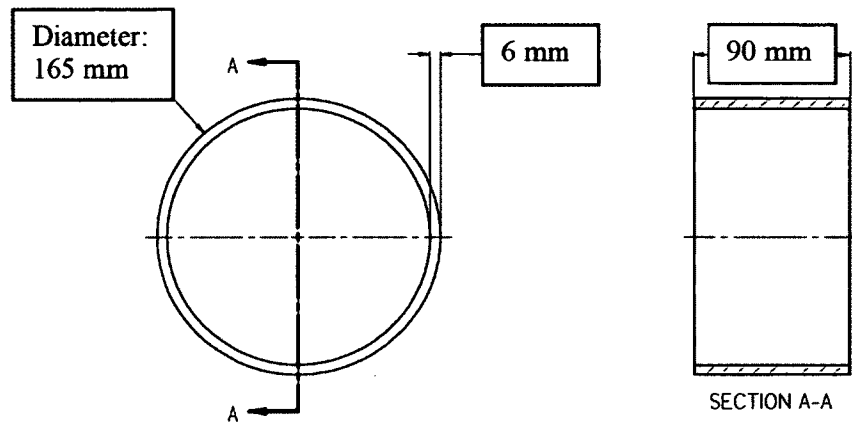


Figure 5-2: Tube details (6 mm wall)

### 5.2.3 Specification of Tubesheet Plate Specimens

The tubesheet plate was designed as a three piece assembly (shown in Figure 5-3). A simplified geometry was made using a smooth bore (i.e. without grooves) for the purpose of minimizing the effect of the interaction between the axial extrusion of the tube and the grooves present in the CANDU<sup>®</sup> design. The tubesheet plate design allowed the tube to be removed from the tubesheet by unbolting the tubesheet halves and, additionally, it made use of a re-useable adapter plate (reducing the material used by about half). The tubesheet plates were fabricated from 304 stainless steel, as per the design of calandria tube in the CANDU<sup>®</sup> design, and were not stress relieved following machining.

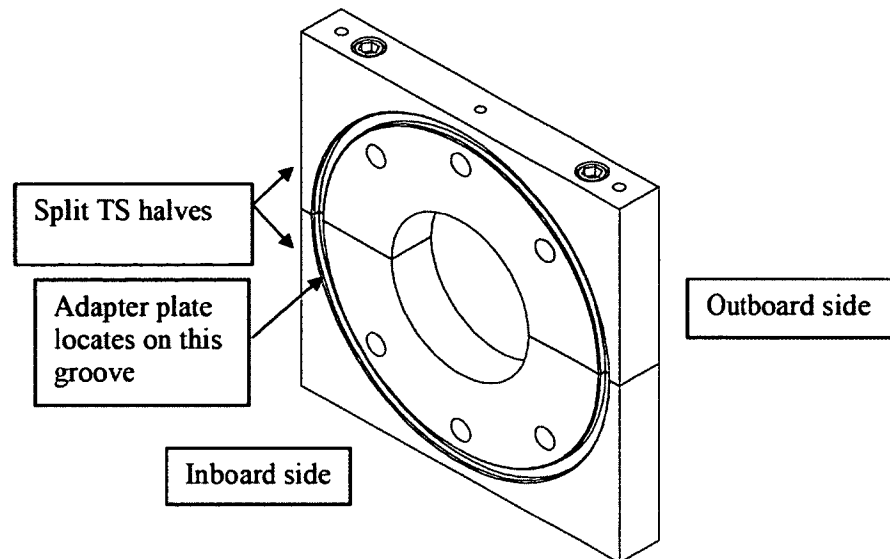


Figure 5-3: Split tubesheet plate

The bottom face of the tubesheet features two  $\frac{1}{2}$ "-13 tapped holes used to secure the tubesheet plate to the rolling table during assembly. The purpose of this connection is to resist the rolling torque imparted by the expansion tool.

### 5.3 Rolling Equipment and Fixturing

The primary forming tool is a Commonwealth #60 (shown in Figure 5-4), 5-roller roll expander. An air motor is used to drive the rotation of the tapered mandrel, which rotates the rollers. The mandrel is self-feeding, meaning that the axes of the rollers are skewed relative to the axis of the mandrel such that the rollers tend to roll into the tube. This result has the effect of drawing the mandrel in and forcing the rollers out. The tilt of the roller causes it to trace out a slight hourglass shape, illustrated in Figure 5-5. The mandrel cage holds the rollers at a fixed axial position centered relative to the tubesheet bore, while the mandrel is drawn forward, extending the rollers in the radial direction, as illustrated in Figure 5-6. The maximum radial extension of the expansion tool is adjustable via the stop collar. The stop collar bears against the threads on the mandrel to

limit the axial travel of the mandrel by contact with the expander extension. An internal thrust bearing allows the mandrel to continue to rotate while the stop collar is bearing against the expander extension. The mandrel is tapered at 0.0322 mm / mm (radial over axial), the rollers (shown in Figure 5-7) are tapered at 0.0136 mm / mm with an effective length of 50 mm and a nominal diameter of 51.6 mm.

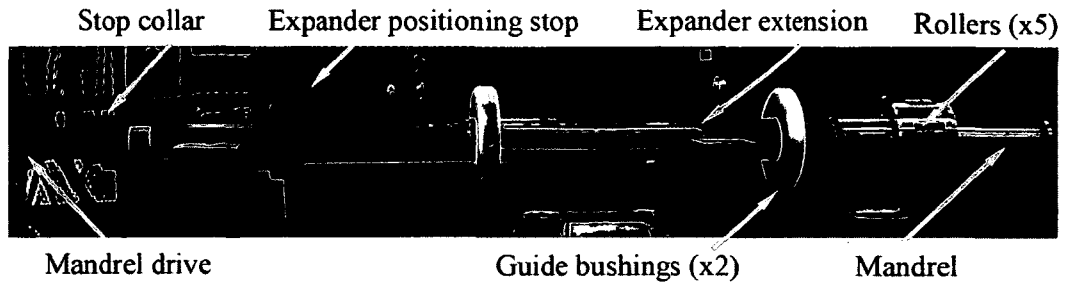


Figure 5-4: Commonwealth # 60 rolling tool

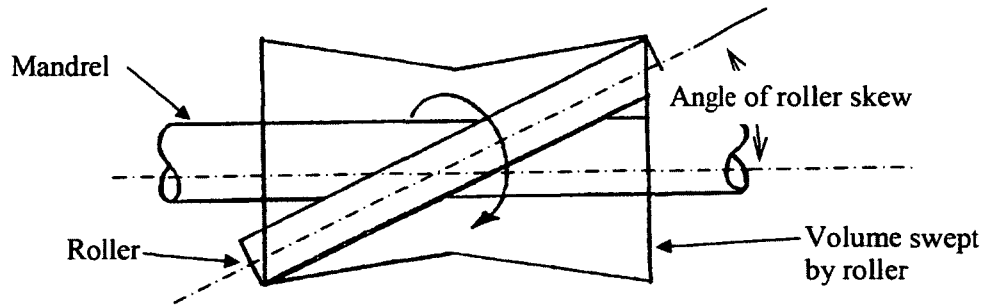


Figure 5-5: Sweep of skewed rollers<sup>8</sup>

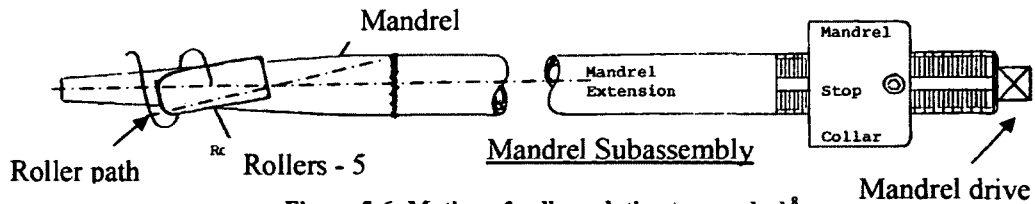


Figure 5-6: Motion of roller relative to mandrel<sup>8</sup>

Initially the expansion is set by placing a ring gauge over the expansion tool and gently advancing the mandrel by hand until all five rollers contact the ring gauge. The stop collar is then adjusted until it contacts the expander extension (see Figure 5-4), and then backed off to the nearest half turn<sup>20</sup>; a set screw is inserted to prevent inadvertent adjustment of the stop collar. Further adjustments to the maximum expansion are made with a prescribed number of turns out or in (to increase or decrease the diameter, respectively), knowing the thread pitch and mandrel taper.

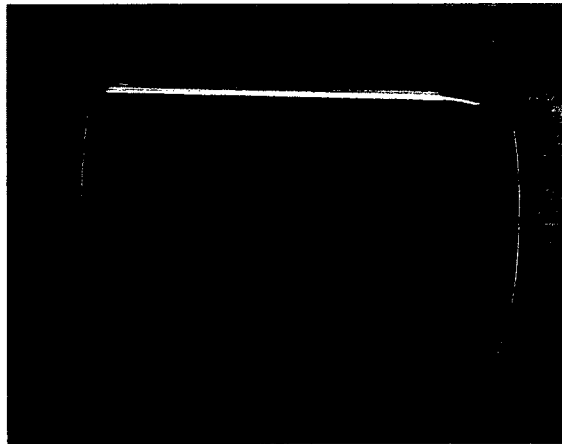


Figure 5-7: Photo of one individual roller

The axial position of the tube in the tubesheet is maintained by the tube restraint collar (see Figure 5-8). The tube restraint collar is clamped to the tube at an axial position such that the tube is flush with the outboard face of the tubesheet plate with the collar bearing face in contact with the inboard face of the tubesheet plate. Three clearance holes are drilled in the tube to allow for 9.5 mm (3/8") diameter hardened steel die pins to be inserted through the collar and tube. The tube restraint collar prevents the tube from

---

<sup>20</sup> The mandrel thread has two flats such that the threads on the mandrel are not damaged by turning in the set screw.

being drawn into the bore before the friction with the TS bore is sufficient to restrain the tube. A clamp, referred to as the nip-up clamp, is used to hold the tube and tube restraint collar in place with the tube axis parallel with the bore axis until the nip-up step (step 1 in Section 2.1) is complete, at which point the clamp is removed.

The mandrel is positioned using a guide tube, as shown in Figure 5-9. The mandrel remains centered relative to the guide tube by the two guide bushings shown in Figure 5-4. The guide tube serves three functions: it supports the rolling tool, it provides mechanical restraint to the self-advancing motion of the expander, and it guides the rollers into the tube bore when the mandrel is inserted into the tube. A pipe stand is placed beneath the guide tube to minimize the bending moment applied to the tubesheet plate from the weight of the rolling mandrel.

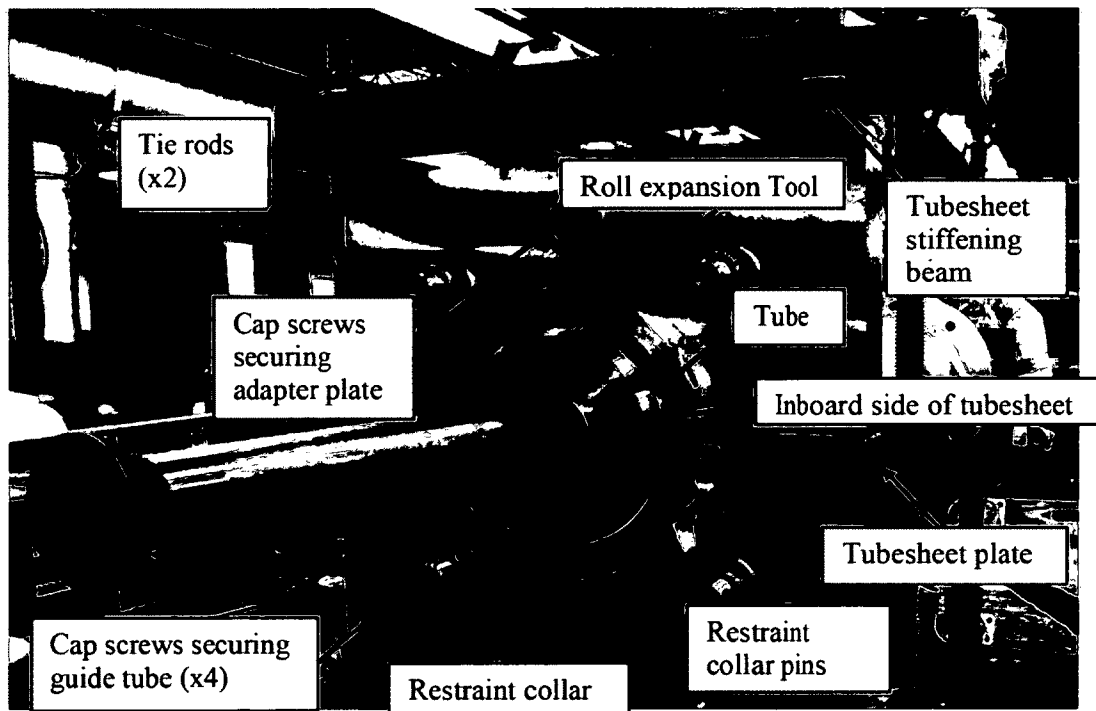


Figure 5-8: Rolling setup viewed from inboard side, nip-up clamp removed

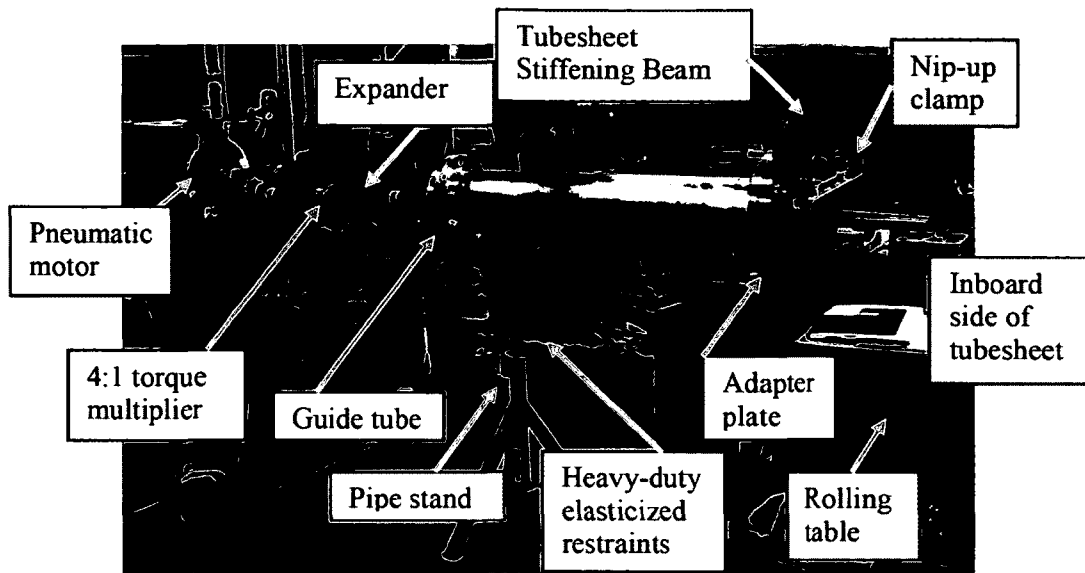


Figure 5-9: Roll-expansion setup

The rolling torque is applied via a pneumatic motor coupled to a 4:1 torque multiplier. The motor is positioned on a rolling stand and is held in contact with the mandrel by heavy-duty elasticized restraints, as shown in Figure 5-9.

## 5.4 Joint Assembly

### 5.4.1 Setup

The two halves of a tubesheet plate are assembled together with two alignment pins and two M20 cap screws holding the tubesheet halves together, each with a pre-tension of 203 N-m (150 ft-lb). The assembled tubesheet plate is then fixed to the rolling table by two ½"-13 cap screws.

A stiffening beam (50 mm square, carbon steel) is positioned over the top of the tubesheet plate, as shown in Figure 5-8. The beam is secured to the rolling table by two tie rods (¾" carbon steel threaded rods). The beam preload is set by a torque of 203 N-m (150 ft-lb) on each tie rod. Since the rolling process acts to bend the plate open (illustrated in Figure 5-10), the load of the beam is transferred to the plate by two steel standoffs each with a contact area of 50 mm x 25 mm, located at the outer edge of the tubesheet plate, as shown in Figure 5-8.

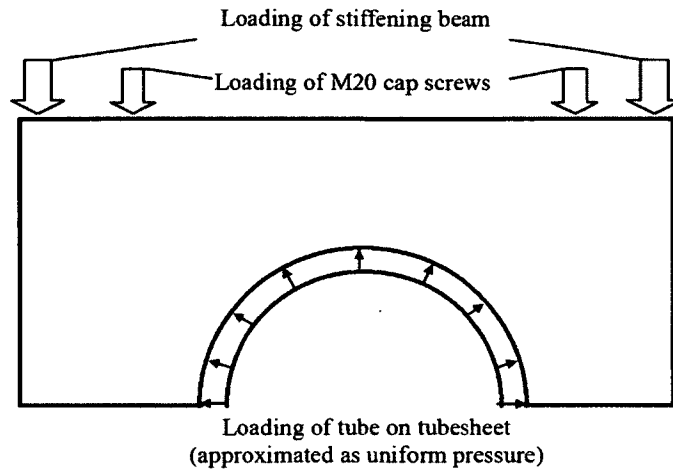


**Figure 5-10: Illustration of loading of upper tubesheet plate**

Once the beam position is secured, the adapter plate is then installed on the tubesheet plate. The adapter plate self-locates by a boss on its inboard face that mates with a groove on the outboard face of the tubesheet plate. The adapter plate is secured to the TS by two socket head cap screws inserted from the outboard side.

The guide tube is the final component to be installed. The guide tube locates on the adapter plate, and is secured to the assembly of the tubesheet and adapter plate by four socket head cap screws that pass through the guide tube flange, adapter plate, and tubesheet plate.

The rolling tool maximum expansion is set by adjustment of the stop collar. The rolling tool is then inserted into the guide tube and is slid forward until the mandrel positioning stop bears against the outboard flange on the guide tube.

#### **5.4.2 Wall Reduction**

The amount of deformation imparted in forming of a rolled joint is quantified by the nominal wall reduction. Measurement of the wall reduction is the most common measure of the amount of deformation imparted on the joint [13]. The wall reduction is calculated by measurement of the tube final diameter, assuming a perfectly rigid tubesheet plate, i.e.

that the entire increase in tube inside diameter is the result of reduction in the tube wall, and is presented as a percent of the unrolled wall thickness. Plastic flow rules dictate that volume is unchanged under plastic deformation. Since the tube is constrained in the hoop direction by symmetry, a decrease in tube wall thickness is accompanied by a corresponding axial extrusion.

The specified nominal wall reduction must be converted into a target expanded tube diameter to set up for the rolling of a particular joint. The target expanded diameter of the joint equivalent to the prescribed percent wall reduction is calculated prior to rolling. For a chosen nominal wall reduction, the target tube inside diameter is defined as Equation 5-1:

$$D_{RI} = D_{TS} - 2 \cdot t(1 - WR) \quad (5-1)$$

where  $D_{RI}$  is the rolled-in tube diameter,  $D_{TS}$  is the as-machined tubesheet inner diameter,  $t$  is the tube wall thickness, and  $WR$  is the nominal wall reduction, often expressed as a percent of the wall thickness.

The final expanded diameter of the tube is a function of the maximum roller extension (i.e. the maximum diameter to which the rollers are extended), and the amount of spring-back in the joint (measured in mm of diameter). A joint is rolled to a target “rolled-in” diameter, which is simply the inside diameter of the tube after being rolled into the tubesheet. This diameter is equal to the diameter to which the mandrel is allowed to expand during rolling, set by adjusting the position of the mandrel stop, less the spring-back of the joint on removal of the mandrel from the joint. This spring-back is typically empirically determined. Changes to rolling parameters such as target diameter, tube wall thickness, or tube material, may change the amount of spring-back. In practice, the roller extension required to achieve a given rolled joint diameter is calculated using the empirically nominal spring-back value. However, since the tube geometries and material combination in the present work have not been previously used, the spring-back could only be estimated based on previous joints rolled [36].

### 5.4.3 The Joint Rolling Process

The mandrel is rolled to “nip-up”, meaning the nominal gap between the calandria tube and tubesheet is taken up (step 1 of Section 2.1). The amount of rolling corresponding to nip-up is measured in axial advancement of the drive shaft and is a function of the shaft taper and the initial clearance between the tube and tubesheet bore. Rolling is temporarily suspended at this point and the nip-up clamp is removed from the restraint collar.

With the nip-up clamp removed, the rolling action is resumed. As the mandrel is rotated, it is drawn into the expander, extending the rollers radially outward. The expansion continues (step 2 of Section 2.1) until the mandrel stop contacts the expander extension. At this point, the rollers have achieved their maximum extension. The rolling continues for another 1.5 turns of the mandrel. This rolling with constant roller extension is termed “iron-out” and is intended to smooth out the tube surface (step 3 of Section 2.1). The nominal wall reduction is now achieved. Once the iron-out is complete, rolling is stopped and the direction of rotation of the air motor is reversed. The mandrel is driven out, relaxing the radial force on the rollers (step 4 of Section 2.1). The spring-back of the tube and tubesheet occur during this phase of rolling.

The expander is removed from the joint, and the inside diameter of the tube is measured using an inside micrometer. If the rolled-in diameter achieved is less than the target, the joint can be re-rolled by adjusting out the mandrel stop, reinserting the expander, and further expanding the joint. The difference between once-rolled and re-rolled joints is assumed to have no effect on the final joint quality. For this body of work all joints are once-rolled.

### 5.4.4 Joints Assembled

The details of the joints assembled as part of the present work are summarized in Table 5-2.

Table 5-2: Summary of joint specimens

Joint	Nominal tube wall thickness [mm]	Nominal wall reduction [%]	CT restraint mechanism	Wire EDM data collection**	Maximum roller expansion [mm]
J1***	10	3	Collar with friction only	Not cut	155.5*
10mm-8.3%WR	10	8.3	Collar with pins	Man	156.02
10mm-6.8%WR	10	6.8	Collar with pins	DAq	155.73
10mm-5.0%WR	10	5	Collar with pins	DAq	155.42
6mm-7.9%WR	6	7.9	Collar with pins	DAq	155.29
<p>* maximum roller expansion approximate because rolling was terminated prematurely.</p> <p>** "DAq" indicates that a data acquisition setup was used to collect the data. "Man" indicates that the values were manually recorded from the gauge indicator display.</p> <p>*** Incomplete rolling</p>					

The test pieces consisted of tubes rolled into tubesheet plates fabricated at AECL according to AECL drawings.

### 5.5 Release of Stresses in Rolled Joints

Stresses were released in two major steps: joint disassembly (state A to state B in Figure 5-11) and tube slitting (state B to state C in Figure 5-11).

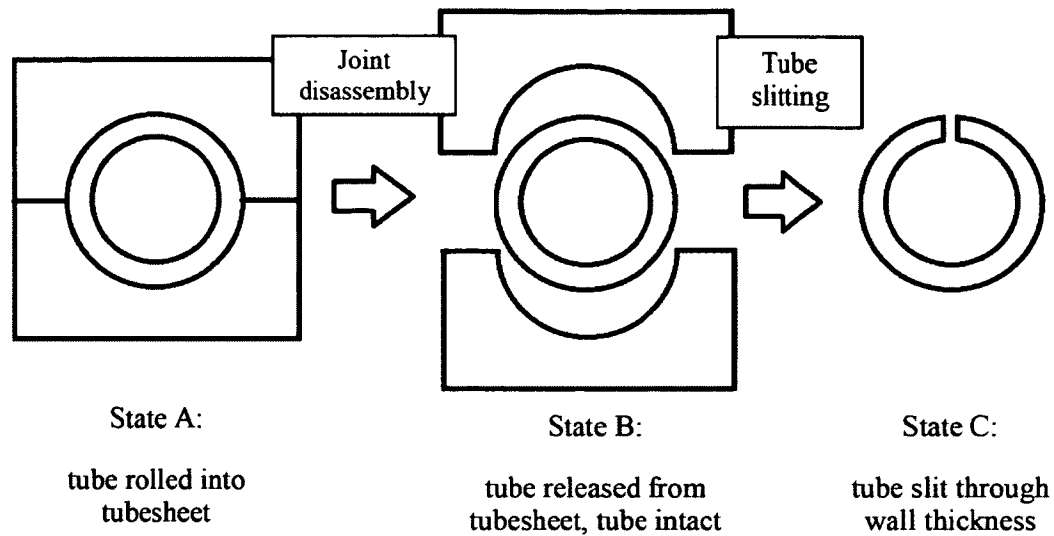


Figure 5-11: Steps in releasing stresses in tubes

## 5.6 Measurement of Strains

Strains were measured using strain gauges applied to the tube inside diameter after rolling (Figure 5-12), and to the outside diameter following joint disassembly. The selected locations for the strain gauges were the results of balancing theoretical and practical considerations. Theoretically, the gauge should be placed to maximize the response to each of the incremental cuts. In general, as the gauge location is increasingly more distant from the cut, the strain response will be smaller in magnitude [11]. Gauges on the top surface, i.e. the outside diameter in the case of cutting from the outside-in, are affected by cut depths up to about 1 to 1.2 times the distance from the edge of the cut to the center of the gauge [11]. Practically, however, the gauges had to be sufficiently separated to allow for proper installation according to the manufacturer's installation guide. The closest gauges were located approximately 12 mm from the edge of the cut. Reference lines were scribed in the tubes to act as guides to aid in ensuring the alignment of the gauges on installation. The potential for errors resulting from misalignment exists.

The magnitude of this error is minimized as the measured direction approaches the direction of the principal stresses [37].

General purpose encapsulated strain gauges (type CEA-13-062UW-350), manufactured by Vishay Micro Measurements were used. Each strain gauge is traceable to the manufactures lot, as detailed in Appendix C. The strain in the hoop direction measured by each particular gauge is the average of the hoop strains over the gauge width (3.05 mm) and the gauge length (1.57 mm). These gauges have a nominal resistance of 350 Ohm and are temperature compensated for Aluminium and Tin (the main constituents of Ampco® 18). The gauges were applied to the surface using M-Bond 200<sup>21</sup>, with a protective coating of M-Coat A<sup>21</sup>, followed by W-1 Wax<sup>21</sup> overlay. Since large strains were anticipated, the gauges were connected to bondable terminals via jumper wires. Three-conductor twisted cable leads, 2.5 m in length and 26 gauge diameter, were soldered to bondable terminals. Each gauge was assigned a unique label. The label consisted of two characters indicating the axial position, two characters indicating the inside or outside of the tube, and two characters indicating the orientation of the gauge. In cases where more than one gauge corresponded to a given ID code, a serial digit was added. The interpretation of this label is summarized in Table 5-3. The details of the gauges applied to each of the specimens are tabulated in Appendix C. Annotated photographs for each specimen can be found in Appendix D.

---

<sup>21</sup> Commercially available products from Vishay Micro-Measurements.

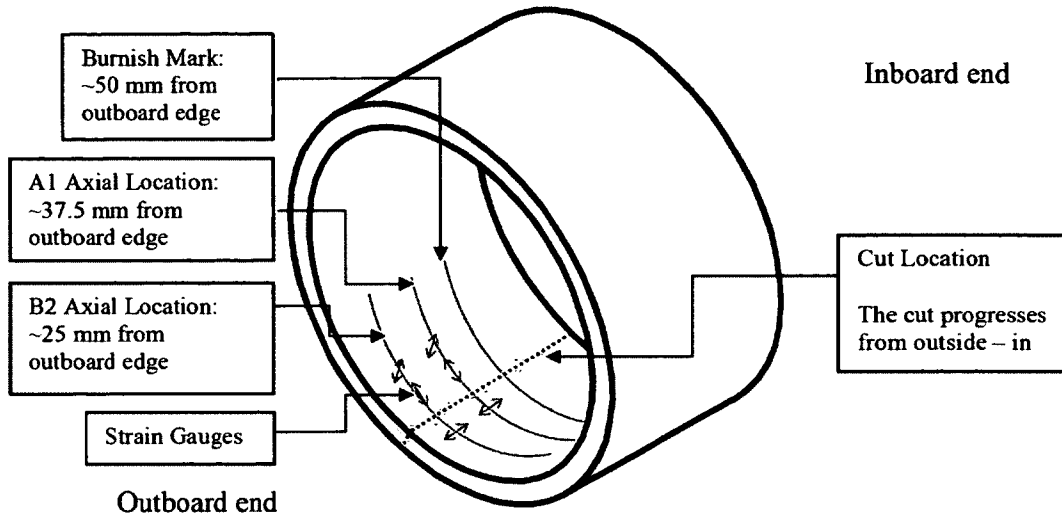


Figure 5-12: Illustration of strain gauge locations on tube inside diameter

Table 5-3: Identification key for strain gauges

Example: A1-ID-ho-001					
Axial Location		Inside or Outside		Gauge Direction	
digits used	Nominal distance from outboard	digits used	meaning	digits used	meaning
A1	38 mm	ID	inside	ho	hoop
B2	25 mm	OD	outside	ax	axial
C3	Other*			45	45° to hoop

\*Location specific to individual sample.

The method used to collect the strain data was improved after cutting the first sample. In the case of the first tube cut, the strain was collected semi-manually using a four channel Vishay P3 strain indicator with internal quarter-bridge completion modules, and the strain readings manually recorded. Since more than four channels were to be measured at each cut depth, four-point contact gold plated push-post connectors were used to ensure repeatable connections between measurements. A precision 350 Ohm resistor was used

as a reference to mitigate the risk of drift in the indicator. The absolute strain readings were recorded, and the net strain was calculated.

The data acquisition setup was improved for the cutting of subsequent tubes; the data were collected using quarter-bridge completion modules connected to a data acquisition module which, in turn, communicated with a computer running a National Instruments LabVIEW® script. Ten data points were recorded for each cut depth, the average of which is reported as the measured value. The setup allowed for up to 16 channels. The collection of data was manually triggered using a LabVIEW® graphical user interface.

### 5.6.1 Strain on Joint Disassembly

The disassembly of the joint is defined in this study as the removal of the constraint of the tubesheet plate from the tube. This disassembly releases the stress at the interface between the tube and tubesheet. The tube deformation resulting from the release of the stress is quantified by the measurement of strain on the tube inside diameter and the measurement of the tube inside diameter. Gauges installed on the inside diameter of the tube were used to measure the strain in the tube. The strain was also calculated from the measured change in diameter at the midpoint of the rolled-in section. This calculation does not account for the Poisson effect and assumes the deformation is perfectly axisymmetric (uniform around the circumference). The measured and calculated strain results are presented in Section 6.2.1. Although the uncertainty in the measurements of the tube inside is large in comparison to the uncertainty in the strain measurement, the comparison provides confidence in the strains measured. The diametral expansion is related to the measured hoop strain by Equation 5-2:

$$\Delta D = D \cdot \varepsilon_h \quad (5-2)$$

where  $\Delta D$  is the diametral expansion of the inside tube diameter,  $D$  is the original tube inner diameter, and  $\varepsilon_h$  is the strain in the hoop direction

### 5.6.2 Strain on Cutting of the Freed Tube

After joint disassembly (State A to State B in Figure 5-11), residual stresses are present in the tube. Cutting the tube (State B to State C in Figure 5-11) releases some of these stresses, resulting in further deformation of the tube, which can be quantified by measured strain. Additional strain gauges were placed on the tube outside diameter to measure these strains. The specimen was cut by placing it in the WEDM with the tube edge opposite the cut being fixed relative to the WEDM coordinate system (shown in Figure 5-13). Since the unrolled end of the tube was the surface with the least deformation, it was used to locate the tube on the WEDM stage to keep the tube axis as parallel to the cutting wire as possible.



Figure 5-13: Tube 10mm-8.3%WR in WEDM prior to cutting

The wire is touched to the surface of the tube to set the zero position, i.e. the surface of the tube. The cut is controlled by advancing the wire in specified increments of 0.2286 mm (0.009") or 0.1524 mm (0.006") in the case of 10 mm and 6 mm wall tubes, respectively. Strain measurements were taken at each cut increment in the coordinate system of the WEDM. Deformation of the tube introduces error in the cut depth measurement since the analysis is performed in the coordinates using the surface of the tube as the zero. This error is proportional to the change in diameter of the tube as in Equation 5-3

$$X_w = X_{edm} + D_0 \cdot \varepsilon_h \quad (5-3)$$

where  $X_w$  is the cut depth in wall coordinates,  $X_{edm}$  is the cut depth in coordinates of the WEDM,  $D_0$  is the original outside diameter of the tube, and  $\varepsilon_h$  is the measured strain in the hoop direction. The stresses induced in the tube through cutting the tube with the WEDM process are negligible [32].

The data was collected using a data acquisition setup that recorded 10 data points for every cut depth; the data points were then averaged. The strain measurements showed very little change in very shallow cuts. As a result, the first 4 cuts (~ 0.9 mm and 0.6 mm of wall thickness) were grouped into a single cut.

The cut introduced into the tube produces two cut faces normal to the circumferential direction. The stresses released as this cut progresses are the normal stress in the hoop ( $\theta$ ) direction, shearing in the  $z$ -direction, and shearing in the radial direction.

### 5.7 Hardness Measurement

The hardness of the tubes were measured after the tubes had been rolled, the joints released, and the slot cut. Measurements were taken using the Rockwell B scale at points along the axial length of the tube, both on the inside and outside surface. Since cold work of material increased the hardness, the intention of the hardness measurements was to provide insight into the areas where plastic deformation had occurred.

## Chapter 6 Results and Discussion

The tubes that are the subject of this thesis have been subjected to a series of operations which are expected to change the stress state. The tubes were roll-expanded into tubesheet plates using a 5-roller expansion tool. The rolling load was then released by reversing the direction of the mandrel drive and retracting the rollers. The joints were then disassembled, releasing the interface forces between the tube and tubesheet. The freed tubes were then slit incrementally. Presented in this chapter are the key results divided as follows:

- Roll expansion of the joint
- Joint disassembly
  - Measured strains
  - Residual stresses
  - Calculated tube-to-tubesheet interface pressure
- Joint slitting
  - Stress on the tube surface
  - Through thickness stress distribution
- Tube and tubesheet surface hardness

### 6.1 Roll Expansion of Tubes into Tubesheets

The parameter most commonly used to specify the amount of deformation imparted to a rolled joint is percent wall reduction (defined in Section 5.4.2) [13]. However, this parameter is determined by measuring the diameter of the completed joint, thus it is not directly useful in controlling the rolling process. Instead, the final (rolled-in) diameter is controlled by setting the maximum roller extension. The relation between maximum roller extension and percent wall reduction requires additional information about the spring-back of the joint on retraction of the expander. This is typically empirically obtained. The rolling parameters for the joints formed in this work, including the

resultant spring-back observed, are listed in Table 6-1. The tubes are designated in the format of “XXmm-YY%WR” where “XX” represents the nominal tube wall thickness in millimeters, and “Y.Y” is the nominal wall reduction to which the tube was rolled. The actual tube wall reduction has been calculated based on the measured tube wall thickness from a rolled and released joint. The deviation of the actual wall reduction from the nominal wall reduction appears to be proportional to the nominal wall reduction for a given nominal wall thickness, as shown in Figure 6-1. This suggests that nominal wall reduction is a suitable parameter to differentiate between joints with tubes of given wall thickness varying in tube deformation. However, the deviation of the actual wall reduction from the nominal wall reduction varies between tubes of different wall thicknesses rolled to the same nominal wall reduction. This indicates that nominal wall reduction is not a good measure for quantifying the degree of rolling between tubes of different wall thicknesses.

**Table 6-1: Joint rolling parameters**

Label <sup>22</sup>	Wall Thickness	Maximum Roller Expansion	Diameter Achieved	Resultant Spring-back	% Wall Reduction	
	[mm]	[mm]	[mm]	[mm]	nominal [%]	actual [%]
10mm-8.3%WR	10	156.02	155.14	0.88	8.3	5.3
10mm-6.8%WR	10	155.73	154.8	0.93	6.8	4.5
10mm-5.0%WR	10	155.42	154.51	0.91	5	3.5
6mm-7.9%WR	6	155.29	154.51	0.78	7.9	4.7

---

<sup>22</sup> The tube is referenced by this label in the remainder of this thesis.

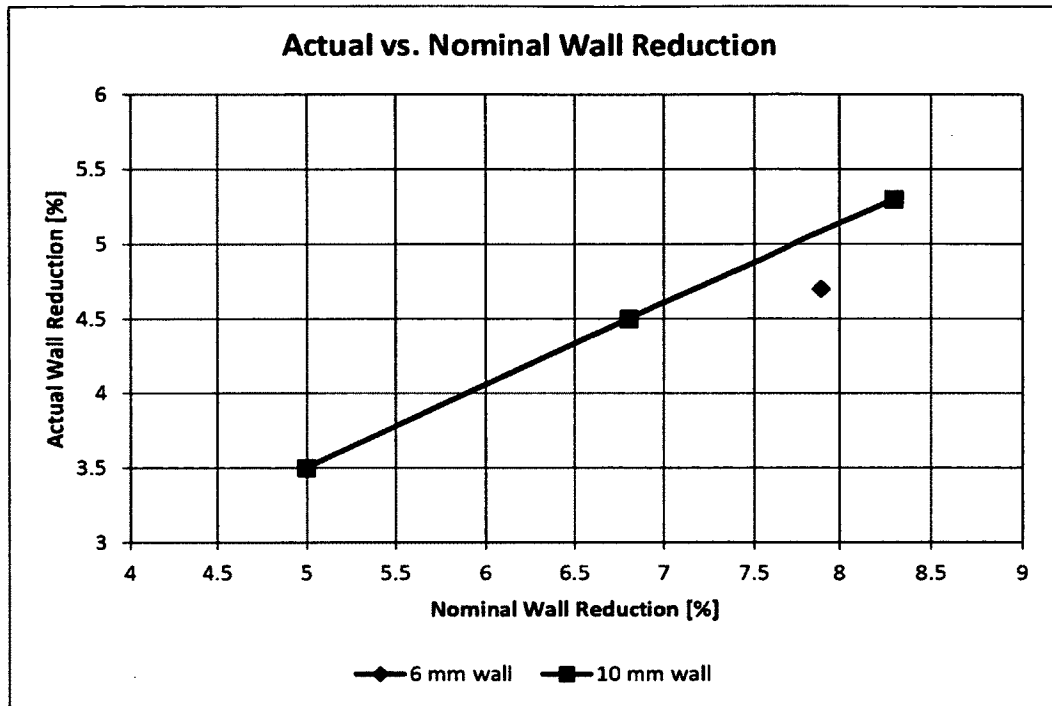


Figure 6-1: Deviation of actual wall reduction from nominal wall reduction

The spring-back in the case of the 10 mm tubes is in the range of  $0.91 \text{ mm} \pm 0.03 \text{ mm}$  on diameter, and  $0.78 \text{ mm}$  for the 6 mm tube<sup>23</sup>. We can attribute the difference to the tube wall thickness since all of these joints had the same pre-rolled inside diameter and clearance with the tubesheet plate prior to rolling. In the case of two tubes with the same inside diameter, differing only in wall thickness, equivalent pressures on the outside surface are expected to result in a smaller reduction in diameter for the thicker walled tube. The observation that the thicker-walled tube exhibited more spring-back (greater reduction in diameter) than the thinner-walled tube suggests that more pressure is relaxed at the tube/tubesheet interface on release of the rolling force (step 7 in Section 2.2). This is consistent with the lower interface pressure observed (shown in Figure 6-6).

<sup>23</sup> No variation is reported in the case of the 6mm tube since only one tube was rolled.

## 6.2 Joint Disassembly

The results obtained on disassembly of the joint are presented in this sub-section. These results include strains measured on the inside diameter of the tube, calculation of the surface stresses, and calculation of the interface pressure between the tube and tubesheet plate.

### 6.2.1 Strains Measured on Joint Disassembly

The strains were measured on disassembly at two axial locations: the A1 location is approximately at the midpoint of the bore, and the B2 axial location is farther outboard, approximately midway between the A1 location and the outboard face, as described in Section 5.6 and detailed in Appendix D. The measured strains are summarized in Table 6-2 and represented graphically in Figure 6-2 along with the strain calculated from measurements of the diameter in Table 6-3. These strains are all measured on the inside surface of the tubes for obvious reasons.

**Table 6-2: Measured strain on joint disassembly**

Joint #	Strain gauge measurement [microstrain]					
	A1-ID-Hoop	B2-ID-Hoop	A1-ID-Axial	B2-ID-Axial	A1-ID-45°	B2-ID-45°
10mm-8.3%WR	2072	2496	-1484	-1152	-	-
10mm-6.8%WR	2155	2558	-1177	-933	745	875
10mm-5.0%WR	2033	2256	-1026	-410	470	1427
6mm-7.9%WR	2665	3226	-1806	-2000	-	-

**Table 6-3: Change in diameter on joint disassembly<sup>24</sup>**

Joint ID	Increase in tube diameter		
	[mm]	[microstrain]	±
10mm-8.3%WR	0.27	1727	580
10mm-6.8%WR	0.52	3360	580
10mm-5.0%WR	0.68	4401	580
6mm-7.9%WR	0.69	4440	580

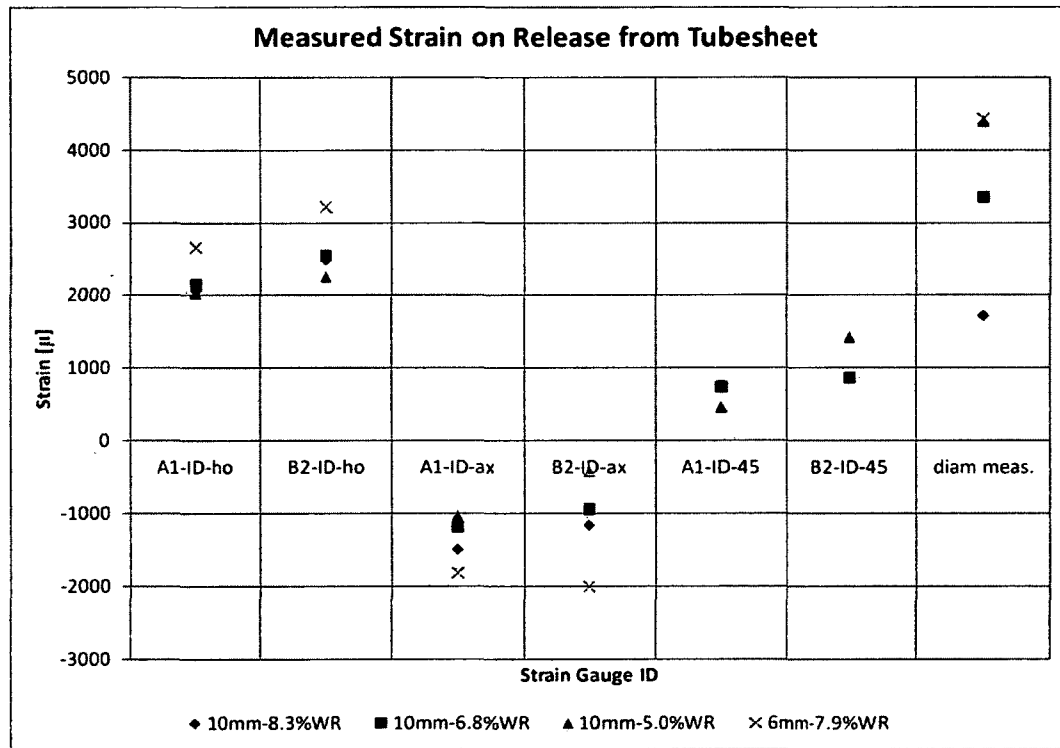


**Figure 6-2: Strain on release of tube from joint**

<sup>24</sup> The uncertainty estimate attempts to account for instrument accuracy plus variation around the circumference in the tube bore, as well as operator deviation from being perfectly perpendicular to the tube axis.

In all cases the hoop strains and diametral increases are positive and the axial strain negative. The positive hoop strain is consistent with the measured net increase in the tube diameter, which is an intuitive result of the release of a restraining pressure on the outside surface. Absent of other effects, a net compressive strain in the axial direction is expected with a magnitude of approximately one third of the magnitude of the hoop strain by the Poisson effect. A second effect that would result in a net axial compression on joint disassembly is a net residual axial tension in the tube section as it is restrained from contraction in the assembled joint by friction at the tube/tubesheet interface. A third effect that would result in strain on the inside surface of the tube is axial bending of the tube, i.e. the tube end flaring open. This would result in a positive strain on the inside surface of the tube, and a negative strain on the outside surface. The expected result of these effects is summarized in Table 6-4.

**Table 6-4: Strains on the inside tube surface resulting from diametral expansion, axial contraction, and axial bending effects**

<b>Effect Direction</b>	<b>Diametral Expansion</b>	<b>Axial Contraction</b>	<b>Axial Bending (open)</b>
<b>Hoop strain</b>	Tension	Tension (~1/3 axial)	Tension
<b>Axial strain</b>	Compression (~1/3 hoop)	Compression	Tension (on inside surface)

The ratio of axial strain to hoop strain, as presented in Figure 6-4, indicates that the axial strain cannot be wholly explained by the Poisson effect. The measured axial compressive strains are larger in magnitude (more compressive strain) than one third of the hoop strain. The contribution of axial contraction as a result of frictional restraint of the tube can be estimated through an upper limit calculation.

To generate an upper limit estimate, a uniform pressure along the tube bore equal to 5 MPa<sup>25</sup> is assumed, with the direction changing at the bore midpoint, as shown qualitatively in Figure 6-3 and Equation 6-1.

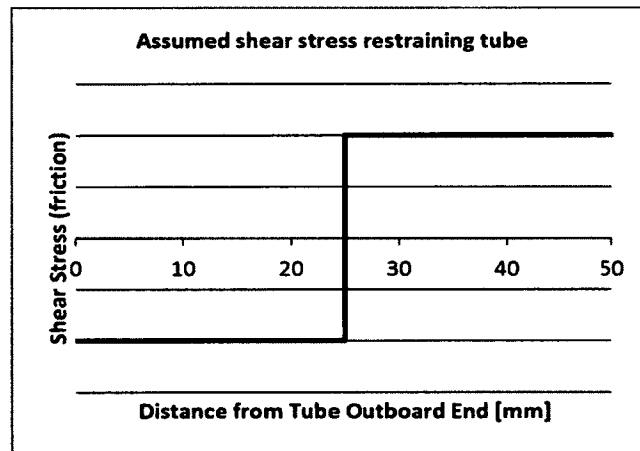


Figure 6-3: Assumed shear stress acting to restrain axial contraction

$$\tau = \mu \cdot p \cdot \left( -1 + 2 \cdot \left( x - \frac{l}{2} \right)^0 \right) \quad (6-1)$$

Where  $\tau$  is the shear stress between the tubesheet plate and the tube acting in the axial direction,

$\mu$  is the coefficient of static friction between the 304 Stainless steel tubesheet plate and the Ampco<sup>®</sup> 18 tube (assumed to be 0.45),  $p$  is the interface pressure,  $l$  is the length of the

<sup>25</sup> See Section 6.2.3 for details of the relevance of this assumption.

interface (50 mm), and the bracketed term  $(\ )$  is a singularity function indicating that the direction of the shear force reverses direction at the bore midpoint  $(x = \frac{l}{2})$ .

The resultant axial force ( $F$ ) acting at the tube at the midpoint of the bore through the tube cross section can be calculated by evaluating Equation 6-2 over the one half of the tube / tubesheet interface,

$$F = \int \tau dA \quad (6-2)$$

which can be rewritten as

$$F = \int_0^{2\pi} \int_0^{\frac{l}{2}} \tau dz r_o d\theta \quad (6-3)$$

where  $\theta$  is the circumferential direction,  $z$  is the axial direction,  $r_o$  is the tube outside radius (nominally 87.5 mm), and  $l$  is the bore length (nominally 50 mm).

Substituting Equation 6-1 for  $\tau$  in Equation 6-3 gives Equation 6-4

$$F = \int_0^{2\pi} \int_0^{\frac{l}{2}} -\mu p dz r d\theta \quad (6-4)$$

which, under the assumption of uniform interface pressure, gives Equation 6-5.

$$F = \mu p 2\pi r \frac{l}{2} \quad (6-5)$$

Evaluating the force for this case, with  $\mu$  equal to 0.45, gives a force of 27.4 kN.

The resultant strain of this stress acting over the tube cross section is given by combining Equations 6-6, 6-7, and 6-8 to give Equation 6-9.

$$\sigma = \frac{F}{A} \quad (6-6)$$

$$\epsilon = \frac{\sigma}{E} \quad (6-7)$$

$$A = \pi(r_o^2 - r_i^2) \quad (6-8)$$

where  $r_i$  is the inner radius of the tube.

$$\epsilon = \frac{l\mu Pr_o}{E(r_o^2 - r_i^2)} \quad (6-9)$$

Evaluating for this case gives 50 microstrain, which suggests that the effect of the frictional axial restraint does not significantly contribute to the deformation on disassembly. The bending open of the tube end is thus the most likely explanation of the deviations from the prediction of the Poisson effect alone. There is a larger difference between the ratio of the axial to hoop stress at the two axial locations measured in the case of the 10 mm walled tube, than between those axial locations in the 6 mm walled tube. This suggests that the difference in the stress state with axial position is greatly affected by the stiffness of the tube wall.

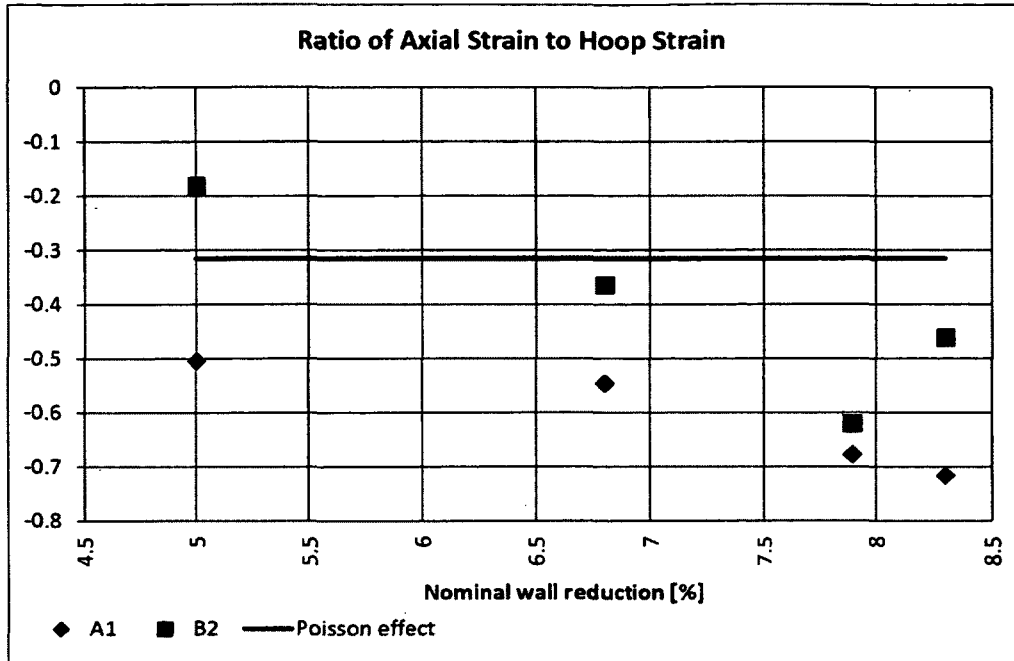


Figure 6-4: Ratio of axial strain to hoop strain

A comparison of the strains on disassembly between the 6 mm and 10 mm wall tubes reveals larger magnitude of both hoop and axial strain for the 6 mm wall tubes. Two factors suspected of contributing to this effect are the larger interface pressure in the case of the thinner tube wall (discussed in Section 6.2.3), and the axial compressive force acting over a smaller tube cross section. Both of these effects suggest a larger axial spring-back for the thinner-walled tube.

Comparing the hoop strains at the bore axial midpoint (A1 location in Figure 5-12) to those farther outboard (B2 location in Figure 5-12) reveals more hoop strain farther outboard. This is consistent with the unrolled section of tube restraining the diametral expansion of the tube, and thus the diametral expansion varying with proximity to the unrolled tube section (i.e. inboard side).

### 6.2.2 Residual Stresses Released on Joint Disassembly

On disassembly of the joints (state A to state B in Figure 5-11) the tube deforms as the interface pressure between the tube and tubesheet is released. From the strains measured on disassembly, the stresses on the surface of the tubes can be calculated directly as described in Section 3.1 since the free surface is, by definition, in plane stress. The principal stresses could be calculated based on measurements in three directions. However in this case the hoop and, to a lesser extent, axial stresses are of interest; the principal stresses were not calculated. The stresses in the hoop and axial directions at the tube surface are tabulated in Table 6-5, and shown graphically in Figure 6-5. Since these stresses are the change in the surface stress during disassembly, the residual stress in the tube before disassembly has the opposite magnitude. For example, an element on the surface of the inside diameter of the 10mm-8.3%WR tube is stressed in tension in the hoop direction and compression in the axial direction on disassembly indicating that the element in the assembled joint is in residual compression in the hoop direction and residual tension in the axial direction.

Table 6-5: Surface stresses on joint disassembly

Tube ID	A1	A1	B2	B2
	Hoop	Axial	Hoop	Axial
	[MPa]	[MPa]	[MPa]	[MPa]
10mm-8.3%WR	196	-101	305	-44
10mm-6.8%WR	218	-61	313	-15
10mm-5.0%WR	209	-47	276	37
6mm-7.9%WR	256	-118	394	-120

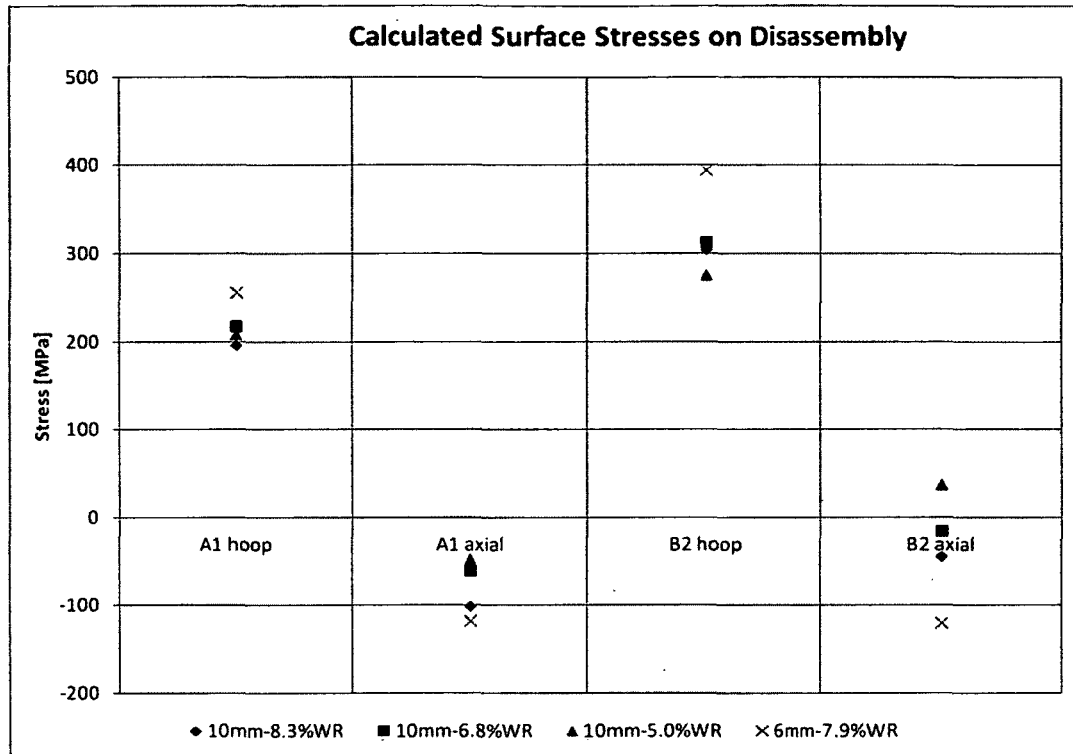


**Figure 6-5: Surface stresses on joint disassembly**

In all four tubes the change in hoop stress on release from the tubesheet is positive at both axial locations, but is larger further outboard. The hoop stresses released in the 10 mm tubes are clustered together. In the case of the 10 mm walled samples, the stresses released at the A1 and B2 axial locations span ranges of only 22 MPa and 37 MPa respectively, indicating that the hoop stresses are relatively insensitive to the amount of roll expansion over the range of deformations, as quantified by wall reduction, imparted to the tubes. This is consistent with the majority of the axial extrusion occurring after the hoop stresses are nearly fully developed (discussed in step 5 of Section 2.2). However, more hoop stress is released in the thinner tube; the hoop stresses in the 6 mm wall are larger by 38 MPa and 81 MPa at the A1 and B2 locations respectively, as compared to the 10 mm walled tube rolled with similar wall reduction. This suggests that the wall thickness (6 mm or 10 mm) has a larger effect on the hoop stress on the inside diameter of the tube resultant from the restraint of the tubesheet than does nominal wall reduction

on rolling. This suggests that the tube wall thickness is the more important design parameter rather than the amount of deformation imparted.

There is no meaningful difference between the axial stress released at the two axial locations in the case of the 6 mm tube. This is consistent with the Poisson effect being the dominant cause of the difference in measured strains between the two axial locations. By contrast, in the case of the 10 mm wall tube, less axial stress is released at the axial location farther outboard (the B2 location). This is consistent with a net axial contraction by the Poisson effect superimposed with a bending open of the tube end, as suggested in Section 6.2.1.

In the case of the 10mm-5%WR tube, i.e. the tube with the least deformation tested, the axial stress is tensile at the axial location further outboard. This is different from the other tubes, suggesting a different stress state from the other tubes. This suggestion is reconciled with the observation that the hoop stresses are relatively insensitive to the degree of deformation applied by invoking the somewhat sequential nature of the hoop and axial plastic deformation in the theory of joint rolling discussed in Section 2.2. The hoop stresses may be fully developed in step 4, but the reduced axial extrusion in step 5 results in a different axial stress state.

In all cases, the hoop stresses at both axial locations on the surface are near or well beyond the uniaxial yield strength of the material suggesting the occurrence of plastic deformation on release from the tubesheet plate. However, the high stresses under the roller have imparted some degree of cold work (confirmed with hardness measurements, presented in Section 6.4) which may have increased the yield strength.

### **6.2.3 Tube-to-Tubesheet Interface Pressure**

The interface pressure between the tube and tubesheet plate was approximated using Equation 3-4 based on the measured strain during disassembly, as discussed in Section 3.2. The interface pressure is approximated as the uniform pressure applied to the outside diameter of the tube resulting in strain equivalent to that measured on joint

disassembly<sup>26</sup>. The uniform pressure was related to the diametral expansion of the tube via an analytical relationship [29]. Two estimates of the interface pressure were obtained for each joint: one using the strain at the axial midpoint (the A1 location), and the other using the strain farther outboard (the B2 location). The calculated interface pressures are tabulated in Table 6-6, and are presented as a function of the nominal wall reduction in Figure 6-6.

**Table 6-6: Calculated interface pressure**

	Nominal Wall Reduction	Interface Pressure Bore Midpoint (A1)	Interface Pressure Outboard (B2)	Difference (B2-A1)
Tube ID	[%]	[MPa]	[MPa]	[MPa]
10mm-8.3%WR	8.3	2.2	5.2	3.0
10mm-6.8%WR	6.8	2.3	5.3	3.0
10mm-5.0%WR	5.0	2.2	4.7	2.5
6mm-7.9%WR	7.9	2.8	6.7	3.9

---

<sup>26</sup> The appropriate sign of the pressure is evident because the tube / TS interface is incapable of transmitting tension.

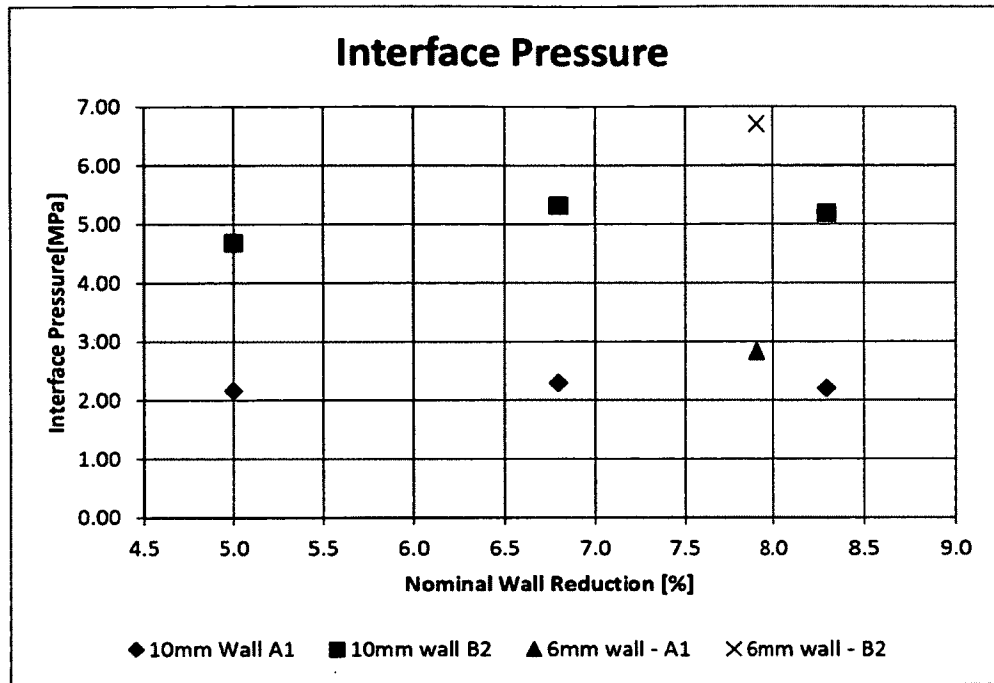


Figure 6-6: Interface pressure as function of wall reduction

There is a significant difference between the estimates at two locations of interface pressures, which indicates that the interface pressure is in fact not uniform along the axial direction. The interface pressure predicted at the more outboard location is consistently higher, which is consistent with the inboard end of the rolled joint being restrained from expansion by the unrolled portion of the tube, as discussed in Section 6.2.2. The difference between the predictions at the two locations is larger for the joint with the 6 mm tube than those for the 10 mm tube. This is consistent with the data from the strain on disassembly (discussed in Sections 6.2.1 and 6.2.2), suggesting that the thicker-walled tube provides more stiffness against bending (i.e. flaring open of the tube end).

Similar to the suggestion in Section 6.2.2, the consistency of the interface pressures between the 10 mm wall tubes suggests that for a given tube wall thickness, rolled to between 5.0 % and 8.3 % nominal wall reduction, the interface pressure is insensitive to

the amount of rolling<sup>27</sup>. It also suggests that the distribution of the interface pressure in the axial direction is similar. This is consistent with the prediction of the Nadai model discussed in Section 2.7.1, and indicates that the interface pressure is largely developed before the significant axial extrusion occurs (as in step 5 of Section 2.2)<sup>28</sup>. However, the interface pressure predicted is far less than predicted by the Nadai model (see Section Figure 2-9).

The interface pressure of the 6 mm wall tube is larger than those of the 10 mm wall tubes, consistent with the thinner-walled tube being more flexible. This difference in pressure is explained by a higher proportion of the rolling force being transferred through the tube to the tubesheet. The unloading of the larger load in the tubesheet would then result in more spring-back of the tubesheet on retraction of the expander. The higher interface pressure suggests that the thinner-walled tube should have higher leak tightness and pull-out strength. The calculated interface pressure provides an indication of the magnitude of the interface pressure present. The calculated interface pressure was used to estimate the upper bound on the frictional restraint of tube in the rolled joint discussed in Section 6.2.1.

### 6.3 Determining Residual Stress on Tube Slitting

Slitting of the tubes (state B to state C in Figure 5-11) following joint disassembly is intended to incrementally release the hoop stresses remaining in the tubes following joint disassembly. The purpose is to quantify the deformation of the tube as each increment of stress is released and to use those measurements to calculate the hoop stresses that were released at the tube surface (Section 6.3.2) as well as to calculate the through thickness

---

<sup>27</sup> This should not be surprising since both the hoop stress and interface pressure calculations are based on the same measurements of hoop strain, but the interface pressure calculation does not account for differences in axial strain.

<sup>28</sup> The amount of “significant axial extrusion” is relevant to the performance of rolled joints with grooves, but is not considered in the present work.

stress distribution (Section 6.3.3) using the crack compliance technique explained in Section 3.4.

In addition to the hoop stresses released in the tube slitting, shear stresses in two directions which are not accounted for in the crack compliance technique. Presented in the following subsections are the measured strains and calculated stresses. The cut depths are recorded in the coordinates of the WEDM, as explained in Section 5.6.2. The final cut depth is equal to the distance between the tube outside diameter at the rolled-in section before cutting and the inside diameter of the unrolled portion of the tube at the end of cutting. This value is typically larger than the nominal tube wall thickness.

### **6.3.1 Measured Strains on Slitting of Free Tubes**

The axial strain measured at the bore midpoint (A1 location) during the crack compliance of the tubes with 10 mm wall thickness is presented in Figure 6-7. Considering first the strains on cutting tubes 10mm-8.3%WR and 10mm-6.8%WR, the gauges on the outside diameter are strained in compression while the gauges on the inside diameter are strained in tension. This is consistent with the tube bending open, i.e. flaring open of the tube end. The lesser degree of rolling resulted in strains of larger magnitude. This could be an important consideration since high stress on the tube inside surface is a concern for deuterium uptake [38].

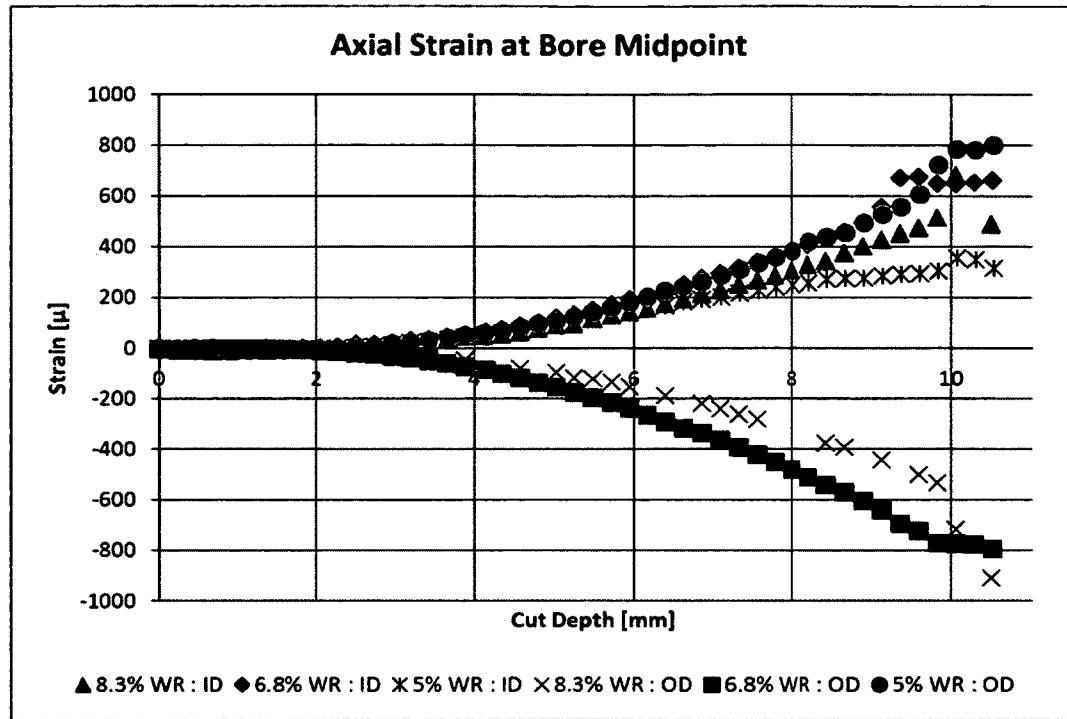


Figure 6-7: Axial strain in 10 mm tubes on slitting

The behavior of tube 10mm-5.0%WR was markedly different than either of tubes 10mm-8.3%WR or 10mm-6.8%WR; the gauges on both the inside and outside diameters were strained in tension. This is indicative of a different stress state than the joints rolled to 6.8 % and 8.3 % wall reduction. An explanation consistent with both surfaces deforming in the same direction is that the Poisson effect of hoop stress released dominates the strain of one or both surfaces. These results clearly suggest that the degree of rolling is not a linear function over the entire range of the amount of deformation imparted to the tube.

The hoop strain at the bore midpoint in the 10 mm tubes are presented in Figure 6-8. In the case of tubes 10mm-8.3%WR and 10mm-6.8%WR, the hoop strain is larger on the

outside diameter as compared to the inside diameter, and this difference is larger for the tube with a lesser amount of wall reduction. The trend in tube 10mm-5.0%WR is vastly different from the joints rolled with more wall reduction. Consistent with the observation of the measured axial strain, tube 10mm-5.0%WR shows a very different hoop strain response from the tubes rolled with more deformation. Because the tube is in static equilibrium at every data point, it is not possible for the release to be a net axial strain. Therefore a possible mechanism for both surfaces reacting by tensile strain is the symmetric restraint manifested by the shear.

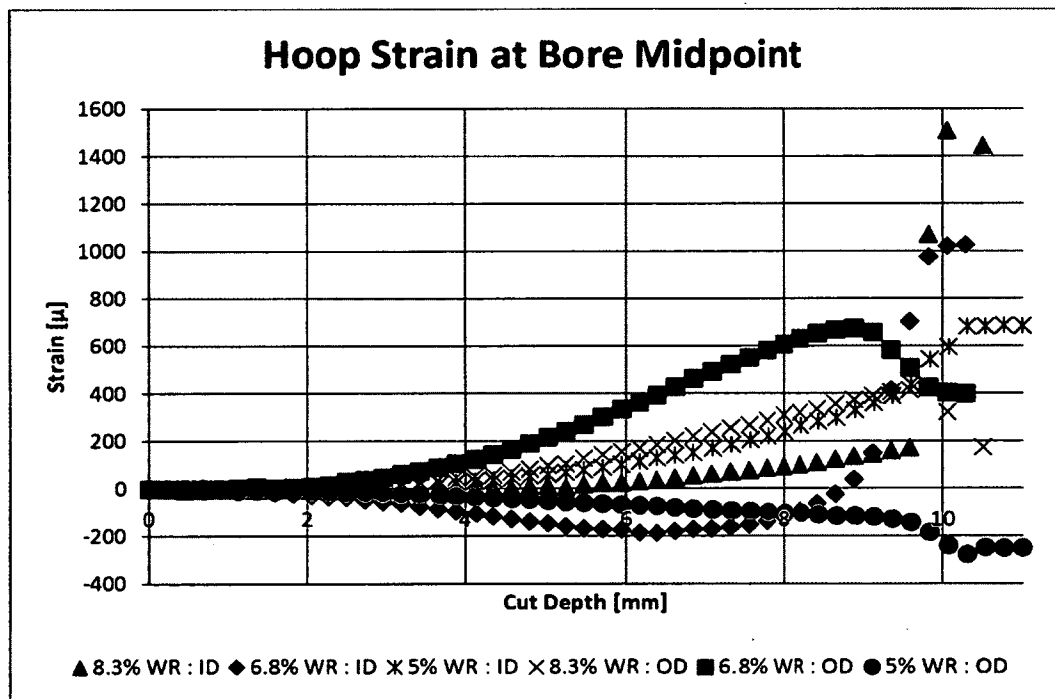


Figure 6-8: Hoop strain in 10 mm tubes at bore midpoint on slitting

The hoop strain and axial strains released on slitting of tube 6mm-7.9%WR, as measured at the bore midpoint, are presented in Figure 6-9. It was observed that on completing the through cut, the tube deformed to close the gap caused by the kerf from the cutting wire. Since some compressive stress could be transferred across the closed cut faces, a second cut was made through the wall thickness at 90°, effectively removing a segment of the

tube circumference, ensuring all hoop stress has been released. The hoop strains on the inside and outside diameter are both tensile while the axial strains are both compressive. This is different from the strains on slitting of the 10 mm tubes. This strain response is consistent with a superposition of the tube simultaneously bending open and the tube decreasing in diameter upon slitting. The tube decreasing in diameter is consistent with the observation that the cut closed on through cutting.

The hoop strain is positive on both the inside and outside diameters. This is consistent with the tube being in residual hoop compression prior to cutting. The strain on the inside diameter was larger in magnitude than on the outside diameter. This is opposite of the trend observed on slitting of the 10 mm tubes with similar wall reduction (tubes 10mm-8.3%WR and 10mm-6.8%WR). The axial strain was compressive on both inside and outside surfaces, which is consistent with the Poisson effect of the strains measured in the hoop direction.

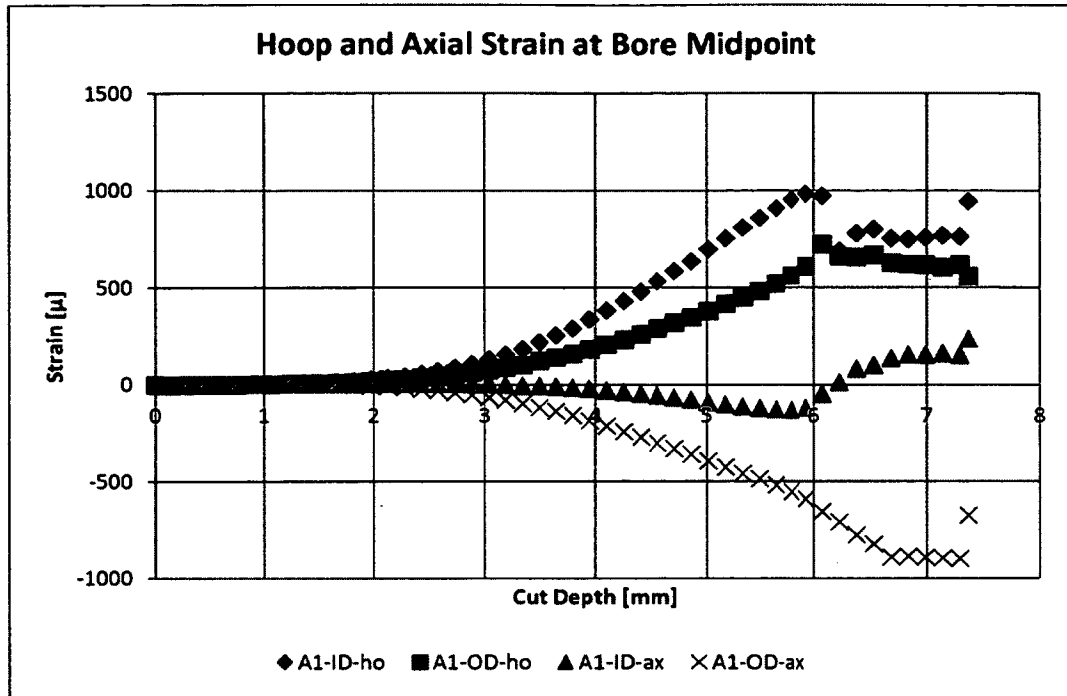


Figure 6-9: Hoop and axial strain in 6 mm tubes at bore midpoint on slitting

### 6.3.2 Residual Stress on the Tube Surface Released in Cutting of the Tubes .

The stress on the tube surface released in slitting the tubes (state B to state C in Figure 5-11) was calculated as described in Section 3.3. These stresses are tabulated in Table 6-7, and shown graphically in Figure 6-10. It is important to note that these stresses are the released stresses and are of the opposite sign to the residual stresses present in the uncut part. As an intuitive check on the sign of the stresses, they can be compared to the strains presented in Section 6.3.1; a measured tensile strain indicates the gauge is elongated, which corresponds to a tensile stress, which in turn indicates that the stress state before cutting was compressive. The hoop stress at the bore midpoint (A1 location) is larger than that further outboard (B2 location).

Table 6-7: Residual stress released on cutting freed tube

Stress [MPa]								
Label	A1-ID-hoop	B2-ID-hoop	A1-OD-hoop	B2-OD-hoop	A1-ID-axial	B2-ID-axial	A1-OD-axial	B2-OD-axial
10mm-8.3%WR	195	74	-14	-23	116	34	-104	-117
10mm-6.8%WR	-3	79	17	10	122	171	-82	-54
10mm-5.0%WR	95	22	1	84	69	-58	89	74
6mm-7.9%WR	125	55	42	25	65	138	-61	-37

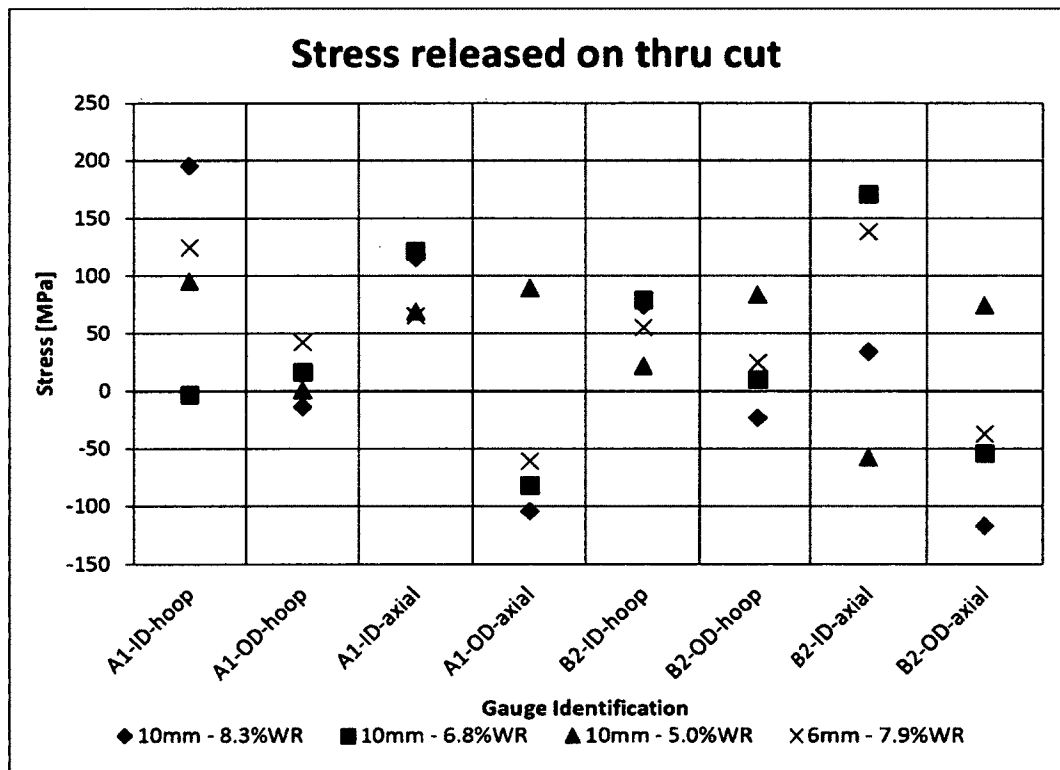


Figure 6-10: Residual stress released in cutting freed tube

The hoop stress results indicate that the magnitude of the hoop stress is larger at the bore midpoint, location A1, as compared to location B2. The axial stress results indicate that the axial strain is slightly larger at axial location A1 as compared to location B2. The sign of the strain indicates compressive strain on the outside diameter and tensile strain on the inside diameter. This indicates a bending moment where the outside surface of the tube is bending such that it is concave in the axial direction.

### 6.3.3 Residual Stress Distribution in the Tubes Post-Disassembly

In Section 6.3.2 the hoop stresses released in slitting the tube were calculated at the locations of strain gauges located on the tube inside and outside surfaces. The hoop stress at internal points is expected to vary continuously from the calculated stress on the inside surface to that calculated on the outside surface. To determine how the stresses vary with position through the wall thickness, the technique of crack compliance, as described in Section 3.4, was used. The results consist of a discrete stress corresponding to the average hoop stress at each cut increment. The predicted stresses near to each surface are ignored because the technique is largely inaccurate in those regions, as discussed in Section 4.4.3. However, the surface stresses calculated directly from the measured strains, as mentioned above, provide information about the end points. Presented in the following subsections are various aspects of the stress predictions. All samples were cut from the surface of the outside diameter inward; a cut depth of zero mm corresponds to the outside surface of the tube, and a cut depth equal to the wall thickness corresponds to the inside surface. In the subsections that follow, the residual stresses at the surface are calculated directly from the measured surface strains<sup>29</sup>.

---

<sup>29</sup> These stresses have a value with the opposite sign of that presented in Table 6-7 because this is the residual stress while Table 6-7 presented the stress released.

### 6.3.3.1 Convergence and Selection of Polynomial Order

As discussed in Section 3.4, an appropriate order of polynomial must be selected in order to apply the crack compliance technique. The stress distributions predicted for the 10mm-6.8%WR tube at the bore midpoint (A1 location in Figure 5-12) based on the gauge on the outside diameter is presented in Figure 6-11. All orders of polynomial are included in each series from 0<sup>th</sup> order up to the order indicated in the legend<sup>30</sup>. Using this data as an example, the stress predicted is somewhat dependant on the number of polynomials included in the fit; however, the predictions converge as the order of polynomial is increased. Convergence was observed for all cases considered in this work, indicating that the set of functions used to fit the distribution is adequate. From the collection of stress predictions, a single “best” fit was determined. The number of polynomials included in the calculation of the predicted stress distribution was 7 since little change was evident in adding higher order polynomials. Selecting the 7<sup>th</sup> order polynomial for the fit is consistent with the orders of polynomial typically used with this technique [11] [30].

---

<sup>30</sup> For example, P03 is the best fit using a linear combination of Legendre polynomials of order, 0, 1, 2, and 3.

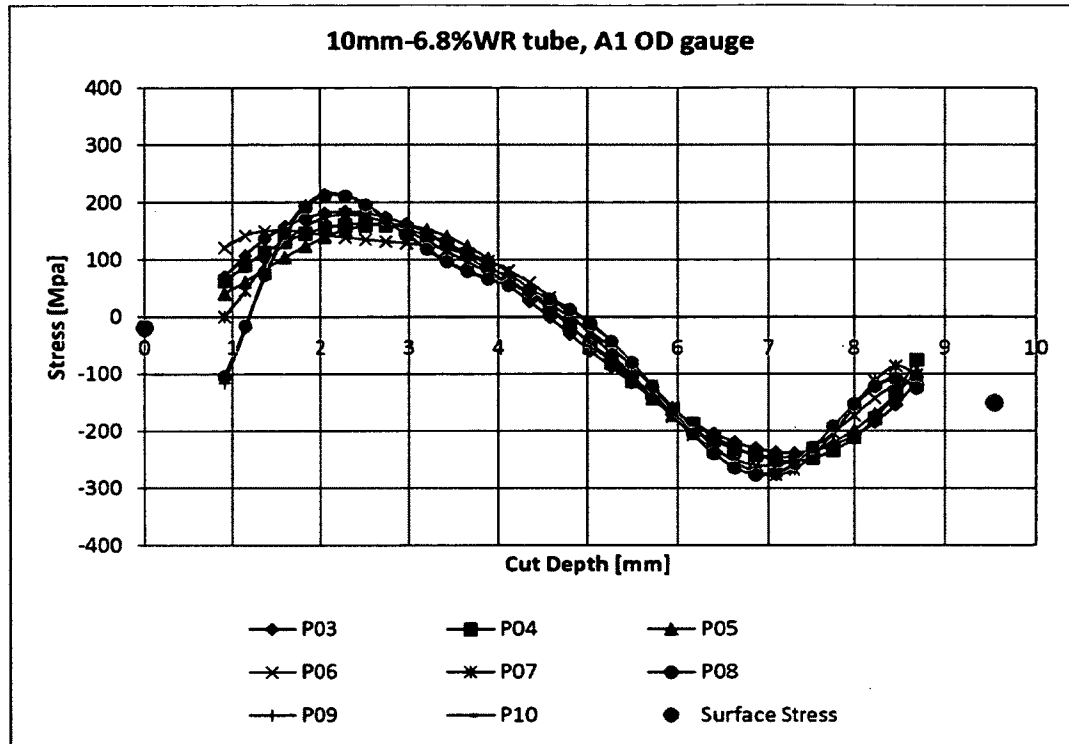


**Figure 6-11: Tube 10mm-6.8%WR through thickness hoop stress distribution at A1 location based on gauge on the outside diameter**

The set of hoop strains measured at each gauge during the slitting process can each be used to calculate the through thickness stress distribution. The relative sensitivity of each of these gauges varies based on the locations as well as with the cut depth. Multiple measurements at the same axial location can each be used to predict the same stress distribution; as a result, the predicted stress distributions should be identical<sup>31</sup>. The predicted stress distribution based on the gauges on the outside and inside diameters for tube 10mm-6.8%WR at the bore axial midpoint (A1 location) are presented in Figure

<sup>31</sup> The term “identical” is used meaning equal within the limits of the uncertainty of the measurements and calculations.

6-12. The distributions show similar general shapes, but the predicted stress at a given point varies considerably between the two predictions. This difference suggests that two assumptions of the technique may be violated to some extent. Firstly, the technique is based on the principle of elastic superposition, which requires that all stresses remain elastic everywhere. If plastic deformation occurs, the stress corresponding to the measured strain deviates from linear, and the magnitude of this deviation increases with increasing plastic deformation, as illustrated in Figure 6-13. The magnitudes of the calculated stresses are close to the uni-axial tensile yield stress of the material (discussed in Section 6.3.2), which suggests that plastic deformation may in fact have occurred. Secondly, the technique attributes all measured strains to the release of hoop stresses; however, based on the observed bending effects discussed in Section 6.3.2, this is not strictly true. Based on these two deviations from the assumed conditions, the kind of information that can be discerned about the rolled joint residual stresses based on the crack compliance technique is drawn into question.

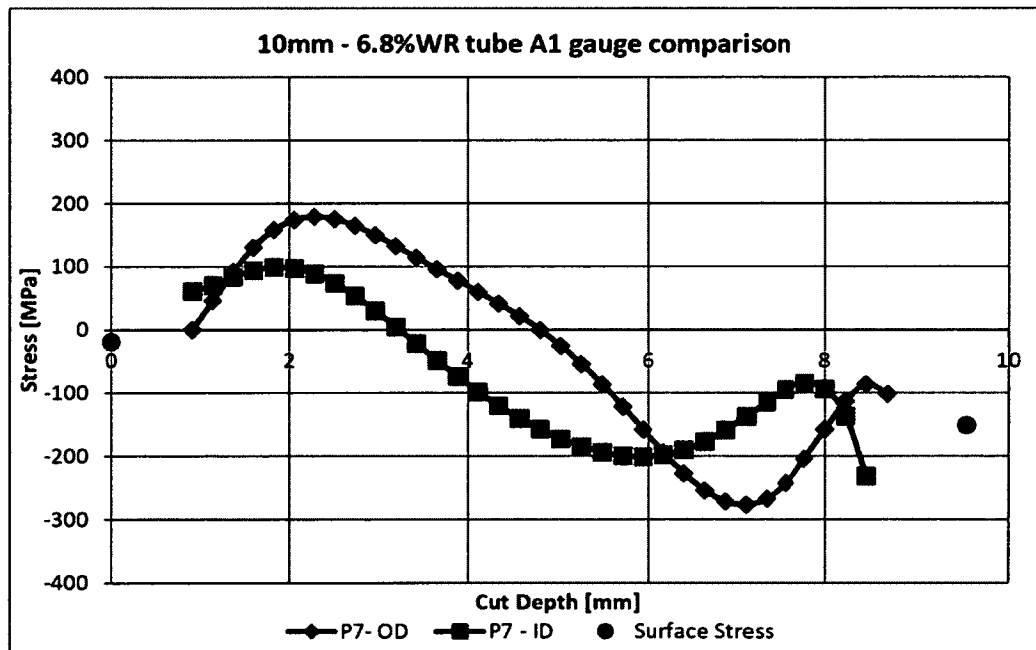
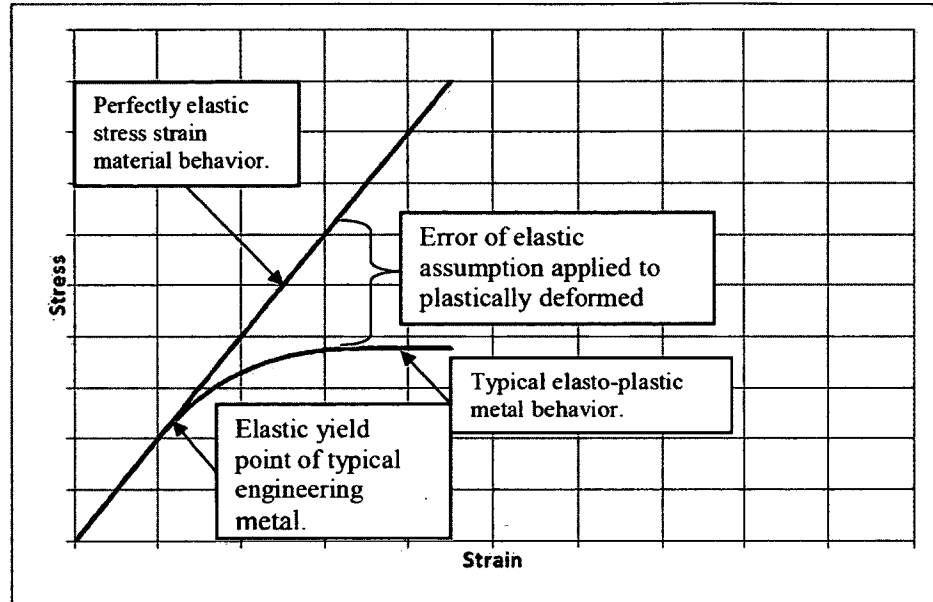


Figure 6-12: Comparison of predictions based on gauges on the inside and outside surfaces



**Figure 6-13: Illustration of error resulting from modeling plastically deformed material as perfectly elastic**

The tube 10mm-8.3%WR, was expanded into the joint and rolled to 8.3 % nominal wall reduction, and consequently the tube was rolled with more axial extrusion than the other tubes tested. The stress distribution calculated at the bore axial midpoint (A1 location) is shown in Figure 6-14. The predicted stresses based on the measurements on the inside and outside diameters do not agree with one another; in several areas through the wall thickness one prediction is of tension while the other compression. The two predictions appear to behave oppositely with an increasing stress in one prediction corresponding with a decreasing stress in the other. The most plausible explanation for such differences is that the measured strain is dominated by the effects of stresses not considered in the model, namely bending and torsional stresses corresponding to shear stresses released on the cut face. The bending effect has the property of opposite stresses on the two surfaces. The closed section of the tube effectively constrains deflection to remain in the plane normal to the  $r$ -direction (i.e. plane strain). The extension of the axial slot releases this

constraint, and results in flaring open of the tube, i.e. axial compressive strain on the outside surface and tensile strain on the inside diameter. The magnitude of the strain resulting from this effect is expected to be highest near the inboard edge of the rolled joint, and lowest at the outboard edge of the tube.

Release of these strains causes the tube to “flare open”. The action of “flaring open” is manifested by an axial contraction of the tube on the outside surface, and an axial expansion on the inside surface. Intuitively, the act of expanding a portion of the tube produces an internal bending moment. There is a residual tension on the outside surface of the tube and a residual compression on the inside surface, which is consistent with the literature [25]. The normal axial stresses are balanced across the tube thickness. The moment equilibrium is balanced by inclusion of shearing.

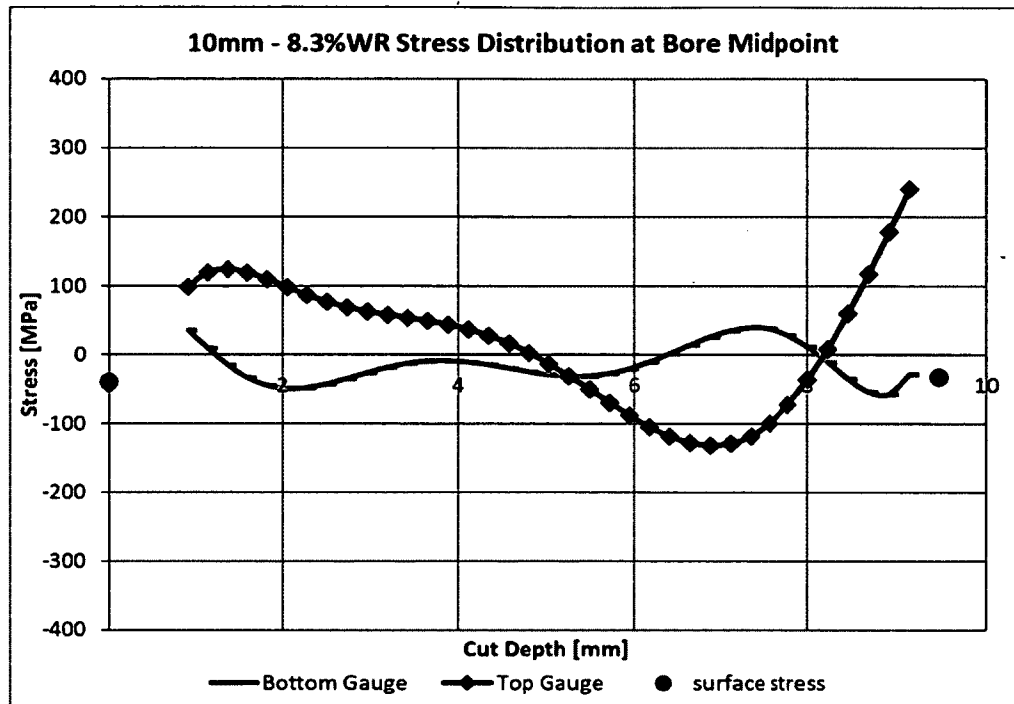
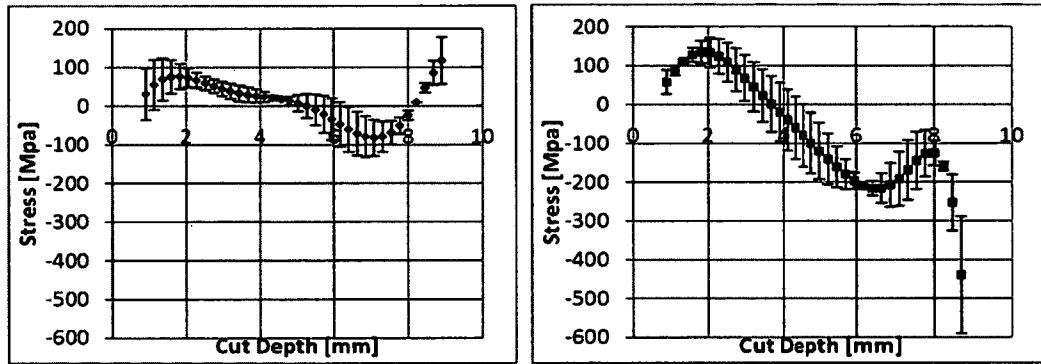


Figure 6-14: Stress distributions at the A1 location for tube 10mm-8.3%WR

The stress distributions predicted at the axial midpoint of the bore are presented in Figure 6-15. To compare the stress distributions between the tubes rolled, the stress is presented as the average of the predictions based on the measurements on the inside and outside surfaces, with error bars spanning the two predictions. Tubes 10mm-8.3%WR and 10mm-6.8%WR are shown in Figure 6-15 a and b, respectively. In both cases, the residual stress is tensile in the outer third and compressive on the inner third of the wall thickness. This is consistent with the inside surface undergoing the most plastic deformation and being compressed by the elastic residual tension near the tube outside diameter. When the tube is expanded and the joint subsequently springs back, it is intuitive that the inside surface is in compression. By disassembling the joint, the restraint holding the outside surface is removed and the outside surface increases in diameter, somewhat releasing residual hoop compression. The prediction of the through thickness distribution suggests that this relaxation is insufficient to overcome the residual compression. The 10 mm tube with the least wall reduction (tube 10mm-5.0%WR is

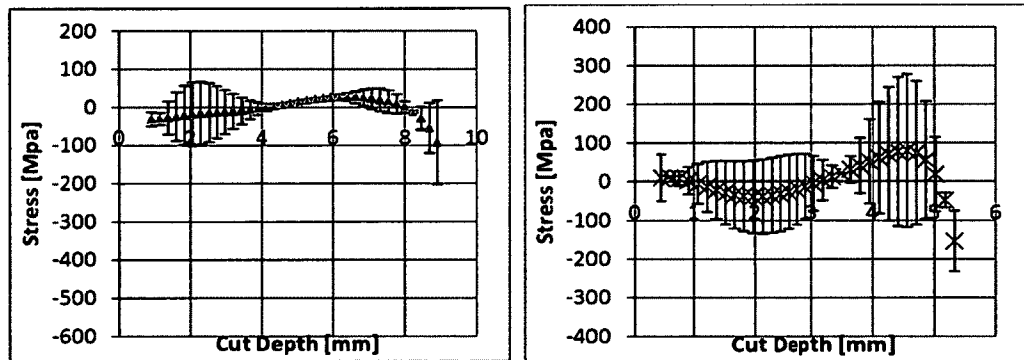
shown in Figure 6-15 c) shows a different distribution with tension near the inside surface and it is unclear if the outside surface is tensile or compressive.

The through thickness stress distribution for tube 6mm-7.9%WR at the axial midpoint of the bore is shown in Figure 6-15 d. Throughout the thickness, the range of predictions includes both positive and negative stresses; as a result it is unclear if the hoop stress is tensile, compressive, or zero.



a) 10mm-8.3%WR

b) 10mm-6.8%WR



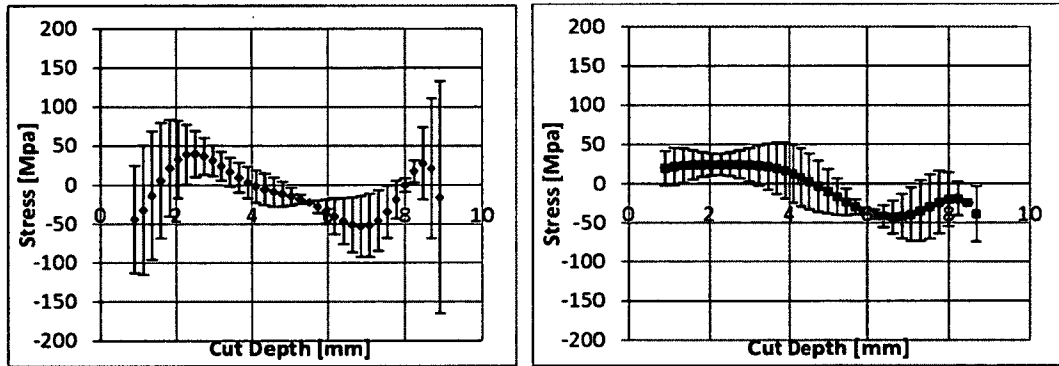
c) 10mm-5.0%WR

d) 6mm-7.9%WR

**Figure 6-15: Through thickness stress distributions at bore midpoint (A1 location)**

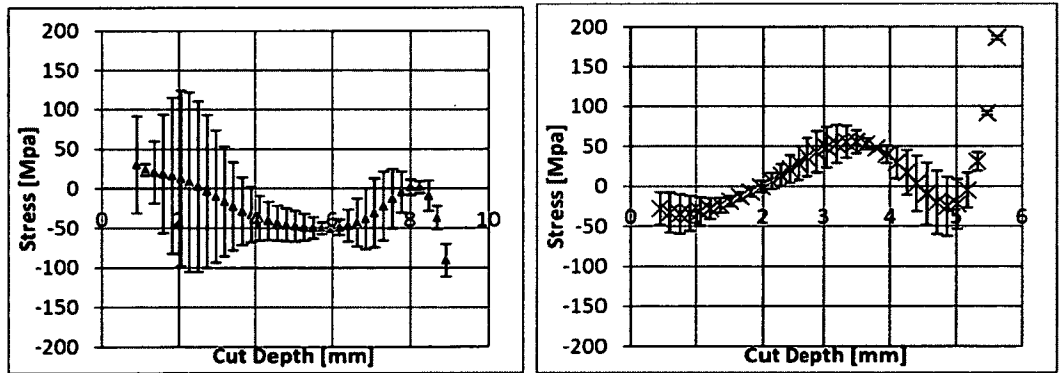
The stress distributions predicted at the axial location midway between the midpoint and the outboard end (i.e. the B2 location) are presented in Figure 6-16. The stress

distribution for tube 10mm-68%WR is similar to that at the bore midpoint, with tension near the outer portion of the tube and compression near the inner diameter. However, the distributions in tube 10mm-8.3%WR and 10mm-5.0%WR wall reductions are unclear because of a large spread in predictions. The calculated strain in tube 6mm-7.9%WR reveals compression near both inner and outer surfaces with tension in the inner segment. This indicates a different stress state than the thicker walled tubes. The difference between the two predictions (inside and outside) is larger for tube 6mm-7.9%WR than for any of the tubes with 10 mm wall thickness, which is consistent with the larger expected axial stress component observed by Van Winssen and Cashen [25].



a) 10mm-8.3%WR

b) 10 mm-6.8%WR



c) 10mm-5.0%WR

d) 6mm-7.9%WR

Figure 6-16: Through thickness stress distribution outboard of bore midpoint (B2 location)

In the case of all eight stress profiles presented, the two predictions intersect between 40 % and 70 % of the distance through the wall thickness. This could correspond with the effective neutral bending axis.

#### 6.4 Surface Hardness

The hardness of each tube was measured at a number of locations along the tube length. The hardness of the inside and outside surfaces are plotted in Figure 6-17 and Figure 6-18. The surface of the tube that is in contact with the roller (between 0 and 50 mm) is harder than the unrolled section, indicating that the rolling imparted plastic deformation in the surface. The hardness is relatively consistent across the rolled-in length on the inside surface. However, on the outside surface, the hardness is not as high in the rolled-in section, as compared to the inside surface in the rolled-in section. This is consistent with the outside tube surface undergoing less plastic deformation.

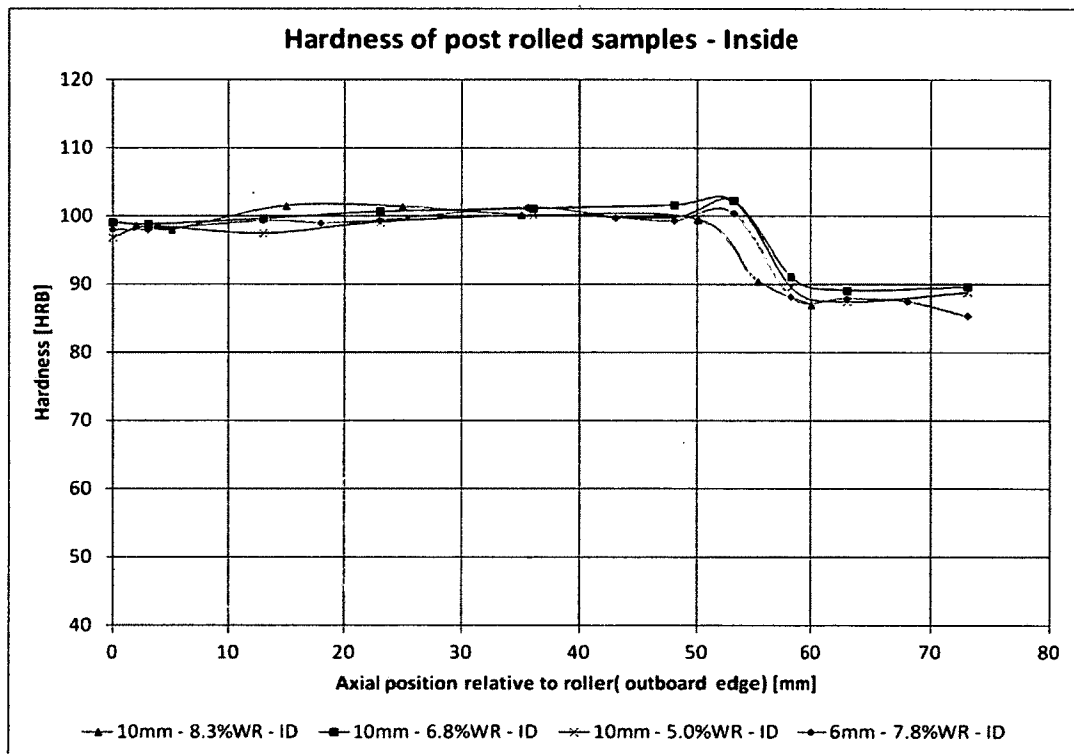


Figure 6-17: Hardness of tube inside surface<sup>32</sup>

<sup>32</sup> Each data point presented is the average of three individual measurements.

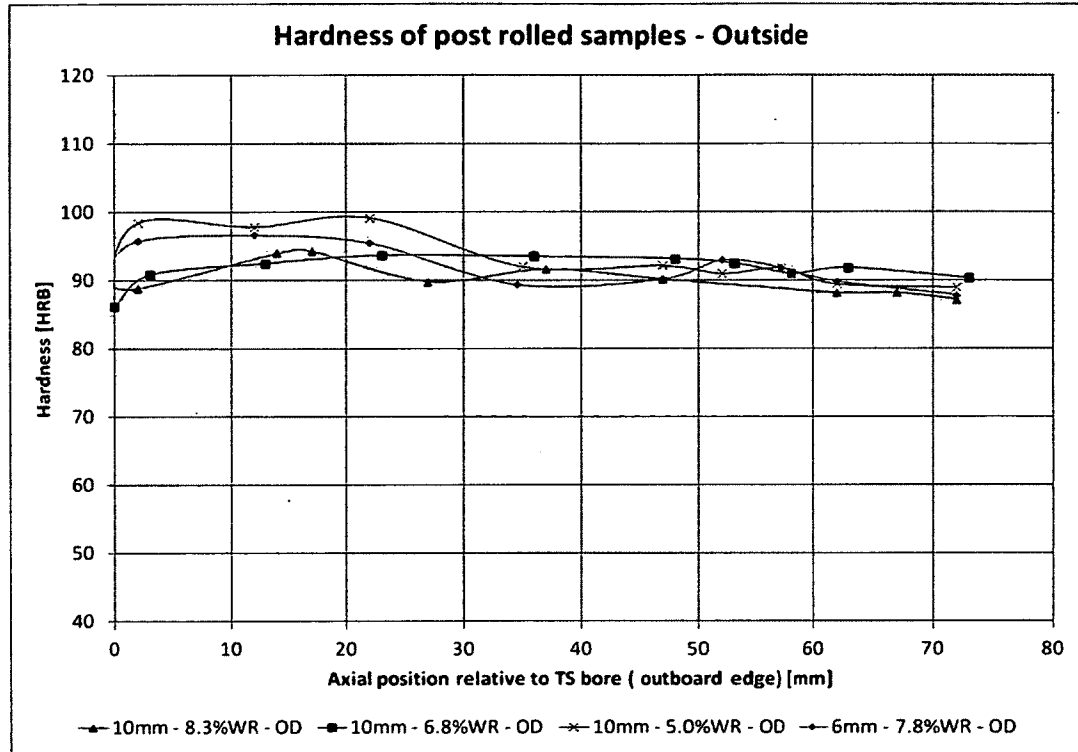


Figure 6-18: Hardness of tube outside surface<sup>32</sup>

## **Chapter 7 Summary & Conclusions and Recommendations**

Summarized in Chapter 7 are the results presented in thesis along with the conclusions that were drawn. Recommendations for further study are also presented.

### **7.1 Summary & Conclusions**

Presented in this thesis is an investigation into the residual stresses present in mechanically roll expanded tube-to-tubesheet joints, as applied to tubes similar in geometry to Gen-IV concept pressure tubes. Four joints were rolled for the purpose of experimentally measuring stresses on disassembly of the joints. The two primary variables investigated were tube wall thickness (10 mm and 6 mm) and degree of rolling, as quantified by percent wall reduction (5 % to 8.3 %). The tubes were rolled into tubesheet plates designed as bolted assemblies, allowing for the joint to be disassembled following rolling. Strain gauges were installed on the tubes to quantify the deformation on release of the tube from the constraint of the tubesheet plate. The strain measured on joint disassembly allowed for the estimation of the interface pressure between the tube and tubesheet plate in the assembled state.

The freed tubes were cut incrementally using a wire electrical discharge machining process to advance a cut radially inward, with each cut increment the deformation of the tube was quantified by strain measurements. The stresses released at each cut increment were calculated using the crack compliance technique based on the compliance of the tube as calculated using a 2D finite element model.

The tubes that are the subject of this thesis have been subjected to a series of operations each of which is expected to change the stress state. The tubes were roll-expanded into tubesheet plates using a 5-roller expansion tool. The rolling load was then released by reversing the direction of the mandrel drive and retracting the rollers. The joints were then disassembled, releasing the interface forces between the tube and tubesheet. The free tubes were then slit incrementally.

The main conclusions drawn from this thesis are as follows:

1. The nominal wall reduction is linearly related to the actual wall reduction for a given tube wall thickness, as discussed in Section 6.1. This indicates that nominal wall reduction is a suitable parameter to differentiate between joints with tubes of given wall thickness varying in tube deformation. However, nominal wall reduction is not a good measure for quantifying the degree of rolling between tubes of different wall thicknesses.
2. The thicker 10 mm walled tube experienced more spring-back on removal of the roll expander, as compared to the 6mm tube.
3. Variation in degree of rolling had little effect on the interface pressure. However the interface pressure in the case of the thinner walled tube was higher.
4. Large stresses are released in joint disassembly. The hoop stresses are larger further outboard than at the bore midpoint. The magnitude of the stress is relatively insensitive to the degree of rolling between 5 % and 8.3 % wall reduction. However, larger stresses are released in the case of the thinner tube. The stresses on the inside surface of the tube approach the material yield strength of the tube.
5. The stress state in the tube under 5 % wall reduction is different than that in the joints with more deformation. This suggests a threshold-type behaviour in the development of the stress state.
6. The validation steps confirmed the successful application of the crack compliance technique to the tube released from a rolled joint.
7. The crack compliance technique is capable of fitting well to functions that vary gently, and fit the general shape of complex stress distributions, but are not accurate where sharp changes in stress exist.

8. Overall the crack compliance technique is effective in predicting the stress distributions, but due to the complexity of implementation method versus the detail of the information provided it is difficult to justify applying this technique to everyday problems.

## 7.2 Recommendations

- Application of a more sophisticated technique for the calculation of the interface pressure allowing for a non-uniform pressure distribution of interface pressure.
- Use neutron diffraction techniques to measure the stress state in the rolled tube.
- Use a 3D model for the compliance matrix. Perhaps there is a way to account for shear stresses in the compliance matrix.
- Increase the stiffness of the tubesheet plate into which the tube is rolled. This could be done by rolling the tube into a complete tubesheet plate and cutting away the tubesheet plate using a WEDM.
- The higher interface pressure for the thinner tube wall, as discussed in Section 6.2.3, suggests that the thinner-walled tube should have higher leak tightness and pull-out strength. A logical extension of this work would be to test this prediction directly.

## References

- [1] W. Diamond, "Fuel Channel Concepts for a Supercritical Water Pressure Tube Reactor Designed with a Tight Lattice Pitch," Report# 153-127200-REPT-001. Atomic Energy of Canada Limited, Mississauga Ontario, 2007. Available upon request from AECL.
- [2] U. A. Abselesalam and M. A. Dokainish, "Tube-To-Tubesheet Joints, A review and Finite Element Analysis," in *International Conference on Expanded and Rolled Joint Technology, Canadian Nuclear Society*, , pp. C73-C96, Toronto, 1993.
- [3] J. Pietralik, "Tube Joint Literature Survey," Report # COG-88-78, Chalk River Nuclear Labs, Chalk River, 1988. Available upon request from AECL.
- [4] R. Maxwell, "Section 5: Materials; Subsection 3: Zirconium Alloys; Part 1: Physical Properties," in *Chalk River Nuclear Laboratories Engineering Manual*, Chalk River ON, Atomic Energy of Canada Limited, 1969. Available upon Request from AECL, pp. DE-13(5.3/1).
- [5] C. Manu, S. Babu, S. Baset and J. Millard, "Initial Development of a Numerical Methodology to Simulate the Roller Expansion Forming Process," in *PVP2005-71011*, Denver Colorado, pp. 1-9, 2005.
- [6] S. R. MacEwen, T. M. Holden, R. R. Hosbons and A. G. Cracknell, "Residual Strains in Rolled Joints," in *Proceedings of ASM's Conference on Residual Stress in Design, Process and Material Selection*, Cincinatti, OH, 1987.
- [7] S. B. Baset and R. Metcalfe, "Axial Rolling Analysis for Pressure Tube Rolled Joints," Report # COG-91-161, Atomic Energy of Canada Limited, Chalk River ON, 1991. Available upon request from AECL.
- [8] T. M. Holden, "Neutron Diffraction Measurements of Axial, Radial and Hoop Strains in a Prototype Rolled Joint," Report # ANDI-1, Atomic Energy of Canada Limited, Chalk River, ON, 1986. Available upon request from AECL.
- [9] S. B. Baset and R. Metcalfe, "Calculation of Stresses in the Elastic Zone of a Pressure Tube Rolled Joint - Axisymmetric Forced Displacement Model," Report # COG-89-216, Atomic Energy of Canada Limited, Chalk River ON, 1989. Available upon request from AECL.
- [10] J. M. Pietralik and R. Metcalfe, "Joint Region Stresses Caused by Forced Radial Displacement One-Dimensional, Axisymmetric, Plane Stress Model," Report # COG-91-70, Atomic Energy of Canada Limited, Chalk River ON, 1991. Available upon request from AECL.
- [11] M. Prime, "Residual Stress Measurement by Successive Extension of a slot: The Crack Compliance Method," *Applied Mechanics Review*, vol. 52, no. 2, pp. 75-96, 1999.
- [12] M. Bach, "Residual Stress: Measurement of Overlap Friction Stir Welded Stringer-to-Skin Joint," [Thesis Proposal], Carleton University, Department of Mechanical and Aerospace Engineering,

Ottawa, 2009.

- [13] S. Yorkell, "Appropriate Correlations for Assessing Expanded Tube-to-Tubesheet Joint Strength," *Journal of Pressure Vessel Technology*, vol. 126, pp. 376-381, 2004.
- [14] J. T. Lund, "Review of Early Development Work on CANDU Pressure Tube Rolled Joints," Atomic Energy of Canada Limited, Report # TDSI-116, Chalk River, ON, 1983. Available upon request from AECL.
- [15] R. Wilson, "The Elastic-Plastic Behaviour of a tube during expansion," in *ASME/CSME Pressure & Piping Conference, 78-PVP-112*, Montreal, 1978.
- [16] D. L. Linning and H. Hatton, "A Theory for Predicting the Interface Pressure of Rolled Joints," TRG Report 850, United Kingdom Atomic Energy Authority, Risley, England, 1964.
- [17] R. Juvinall, *Engineering Considerations of Stress, Strain, and Strength*, New York: McGraw-Hill Book Company, 1967, p. 386.
- [18] T. Harris, *Rolling Bearing Analysis 4e*, New York: John Wiley & Sons inc., 2001.
- [19] B. Sandor, *Fundamentals of Cyclic Stress and Strain*, London, WI: The University of Wisconsin Press, 1972.
- [20] A. Kalnius, D. P. Updike and S. M. Caldwell, "Contact Pressure in Rolled Tube Tubesheet Joints," *Nuclear Engineering and Design*, vol. 130, pp. 229-234, 1991.
- [21] H. M. Sutcliffe and R. C. Hayes, "The Design of Conventional Rolled Joints," Report # CWAED-104, Canadian Westinghouse Company, 1967.
- [22] I. M. Burnie, "Pressure Tube and Calandria Tube Joint Design and Test Programs, Japan, Italy, Canada Information Exchange,," Atomic Energy of Canada, Chalk River, ON, June 13-15 1973. Available upon request from AECL.
- [23] J. Chakrabarty, *Theory of Plasticity*, New York, NY: McGraw-Hill Book Company, 1987, p. 316.
- [24] W. Young, "Residual Stress in Design, Process, and Material Selection," in *Proceedings of ASM's Conference on Residual Stress, Process and Material Selection*, Cincinnati OH, April 1987.
- [25] J. Van Winssen and W. Cashen, "Rolled Joint Theory - Experimental Results and Evaluation," General Electric Company, Atomic Power Department, 1967. Available upon request from AECL.
- [26] A. Nadai, "A Theory of the Expanding of Boiler and Condenser Tube Joints," *Transactions of the ASME*, vol. 65, pp. 865-880, 1943.
- [27] J. Pietralik and R. Metcalf, "Evaluation of Existing Analytical Models of Tube-to-Tubesheet Rolled Joints. Report # COG-91-129," Atomic Energy of Canada, Chalk River, 1989. Available upon request

from AECL.

- [28] R. Rivello, *Theory and Analysis of Flight Structures*, McGraw-Hill, 1969, p. 54.
- [29] W. C. Young and R. G. Budynas, *Roark's Formulas for Stress and Strain 7e*, New York, NY: McGraw-Hill, 2002.
- [30] M. B. Prime and M. R. Hill, "Residual Stress, Stress Relief, and Inhomogeneity in Aluminium Plate," *Scripta Materialia*, vol. 46, no. 1, pp. 77-82, 2002.
- [31] M. B. Prime and M. R. Hill, "Uncertainty, Model Error and Order Selection for Series-Expanded, Residual-Stress Inverse Solutions," *Journal of Engineering Materials and Technology*, vol. 128, 2006.
- [32] W. Cheng, I. Finnie, M. Gremaud and M. B. Prime, "Measurement of Near Surface Residual Stresses Using Electric Discharge Machining," *ASME J. of Eng. Mat. and Tech.*, vol. 116, pp. 1-7, 1994.
- [33] M. Prime, "Sample Files and Calculations for Slitting (Crack Compliance) Method for Measuring Residual Stress," Report # LA-CC-98-0063, Los Alamos National Laboratory, Los Alamos CA, 1998.
- [34] M. B. Prime, P. Rangaswamy, M. R. Daymond and T. G. Abeln, "Several Methods Applied to Measuring Residual Stress in a Known Specimen," in *Proceedings of the SEM Spring Conference on Experimental and Applied Mechanics*, Houston TX, pp. 497-499, 1998.
- [35] M. Boyce, "Photoelastic and Strain Gauge Analysis of Rolled Joints," Report # TR-164, Hawker Siddley Canada, 1976.
- [36] W. Paley, "CANDU 6 Calandria Tube Rolled Joint Testing Phase 1: Replacement Joint Qualification. Report #87RF-31230-TP-001," Atomic Energy of Canada Limited, Chalk River Ontario, 2007. Available upon request from AECL.
- [37] Vishay Micro-Measurements, "Errors Due to Misalignment of Strain Gauges, Tech Note TN-511, Doc # 11061," Vishay Micro-Measurements, Raleigh, NC, 2007.
- [38] R. Dutton, "Hydrogen Embrittlement Effects in Hydride-Forming Metals," Report # AECL-6272, reprinted from *The Metallurgical Society of CIM Annual Volume*, 1978.
- [40] C. Manu, S. Babu, S. Baset and J. Millard, "Initial Development of a Numerical Methodology to Stimulate the Roller Expansion Forming Process," in *Proceedings of PVP2005*, Denver, Colorado USA, 2005.
- [41] P. P. Benham, R. J. Crawford and C. G. Armstrong, *Mechanics of Engineering Materials 2e*, Essex: Addison Wesley Longman Ltd., 1996.
- [42] M. Prime, "Uncertainty, Model Error and Order Selection for Series-Expanded, Residual-Stress Inverse Solutions," *J. of Eng. Mat. and Tech.*, vol. 128, pp. 175-185, 1998.

- [43] P. A. Ross-Ross, "Fuel Channel Development for Canada's Power Reactor," Report # AECL-3126, Engineering Institute of Canada, Halifax, Nova Scotia, 1968.

## **Appendices**

### Appendix A : The Nadai Model

Nadai derived an analytical relationship to model the interface pressure in expanded tube-to-tubesheet joints [26].

This model assumes the following:

- no axial strain,
- the tube is expanded into a hub of infinite radius,
- zero clearance between tube and plate prior to rolling;
- perfectly plastic material behaviour, and
- the von Mises yield criterion defines the elastic-plastic boundary

The predictions presented in the body of this report (see Section 2.7.1) were generated with the method presented in the cited paper [26]. The key steps of the derivation, as applied to the tube geometry in the current work, are reprinted below for the benefit of the reader, but are not intended to be a complete derivation.

#### A.1 Overview of Derivation

Starting with the basic relationship between stress in the tube and external pressures applied to the tube given in Equations A1-1 and A1-2,

$$\sigma_r = -p_1 \cdot \frac{\frac{r_2^2}{r_1^2} - 1}{\frac{r_2^2}{r_1^2} - 1} - p_2 \cdot \frac{1 - \frac{r_1^2}{r_2^2}}{1 - \frac{r_1^2}{r_2^2}} \quad (\text{A1-1})$$

$$\sigma_t = -p_1 \cdot \frac{\frac{r_2^2}{r_1^2} + 1}{\frac{r_2^2}{r_1^2} - 1} - p_2 \cdot \frac{1 + \frac{r_1^2}{r_2^2}}{1 - \frac{r_1^2}{r_2^2}} \quad (\text{A1-2})$$

where the subscripts 1 and 2 indicate the tube inside and outside surfaces, respectively,  $P_1$  and  $P_2$  indicate the internal and external pressures, respectively.

At  $r$  equal to  $r_1$  (i.e. the inside surface of the tube), Equations A1-1 and A1-2 simplify to

$$\sigma_r = -p_1$$

and

$$\sigma_t = \frac{(1 + k^2)p_1 - 2p_2}{1 - k^2}$$

where

$$k = r_1/r_2$$

For  $r=r_2$  (i.e. the outside surface of the tube), Equations A1-1 and A1-2 simplify to:

$$\sigma_r = -p_2$$

and

$$\sigma_t = \frac{2p_1k^2 - (1 + k^2)p_2}{1 - k^2}$$

By equating radial strains and interface pressure between the plate and tube, the equation A1-3 is obtained for the pressures at the tube inside and outside diameter:

$$p_1 = \frac{\left\{2\nu_2 - 1 - 2\nu + \frac{2E}{E'}(1 + \nu')\right\} p_2}{(2\nu_1 - 1)} \quad (\text{A1-3})$$

Take the tangent to the yield ellipse at the point where the tangential stress is equal to zero,.

$$\sigma_{tm} = p_1\nu_1 - p_2\nu_2 = 0 \quad (\text{A1-4})$$

And the tangent that serves as the yield criterion becomes equation A1-5:

$$-v_1 p_2 + v_2 p_1 - 2\sigma_0 = 0 \quad (\text{A1-5})$$

In the case of the 10 mm tube:

$$v_1 = \frac{r_1}{h} = \frac{76.5}{10} = 7.65$$

$$v_2 = \frac{r_2}{h} = \frac{86.5}{10} = 8.65$$

Solving equations A1-4 and A1-5 for  $P_1$  and  $P_2$  will give us the pressure at the inside and interface surfaces at the point where the tube is fully plastic:

$$E=110 \text{ GPa (Ampco}^\circledast \text{ 18)}$$

$$E'=200 \text{ GPa (304 stainless steel)}$$

$$\nu=0.316 \text{ (Ampco}^\circledast \text{ 18)}$$

$$\nu'=0.28 \text{ (304 stainless steel)}$$

$$P_1=0.900 \sigma_0$$

$$P_2=0.7556 \sigma_0$$

The equation of the ratio of the transverse to axial plastic strains is given by equation A1-6

$$\frac{u_1 + u_2}{2(v_1 u_1 - v_2 u_2)} = \frac{(1 + 4v_1)p_1 + (1 - 4v_2)p_2}{(1 - 2v_1)p_1 + (1 + 2v_2)p_2} \quad (\text{A1-6})$$

and the equation for the radial strain at the interface is A1-7

$$u_2 = \frac{(1 + \nu')p_2 r_2}{E'} \quad (\text{A1-7})$$

Introducing the following substitutions

$$u_1 = \frac{(1 + \nu')\sigma_0 r_2}{E'} \cdot y$$

$$p_1 = z\sigma_0$$

$$p_2 = w\sigma_0$$

gives

$$\frac{y + z}{2(\nu_1 y - \nu_2 w)} = \frac{(1 + 4\nu_1)z + (1 - 4\nu_2)w}{(1 - 2\nu_1)z + (1 + 2\nu_2)w} \quad (\text{A1-8})$$

and

$$-\nu_1 w + \nu_2 z - 2 = 0 \quad (\text{A1-9})$$

With these 2 equations  $w$  can be eliminated:

$$y = \frac{1.13873 \cdot (z^2 + 0.139121 \cdot z - 0.033478)}{z - 0.174896} \quad (\text{A1-10})$$

With these relationships the following predictions (Table A-1 and Figure A-1) were made for the relationship between nominal wall reduction and the pressures and expansion on the application of the pressure on the inside diameter.

**Table A-1: Predictions of the Nadai model**

	z	y	Inner Pressure [MPa]	Outer Pressure [MPa]	Inner radial expansion [mm]	Nominal wall reduction* [%]
Elastic	0	0	0	0	0	0
	0.9	0.89	185	154	0.105	1.0
Plastic	0.9	0.89	185	155	0.105	1.0
	1	1.07	205	178	0.126	1.3
	1.12	1.3	226	201	0.153	1.5
	1.17	1.55	240	218	0.183	1.8
	1.23	1.95	252	232	0.229	2.3
	1.27	2.55	260	241	0.3	3.0
	1.3	3.77	267	248	0.443	4.4

\* Assumes zero clearance pre-rolling

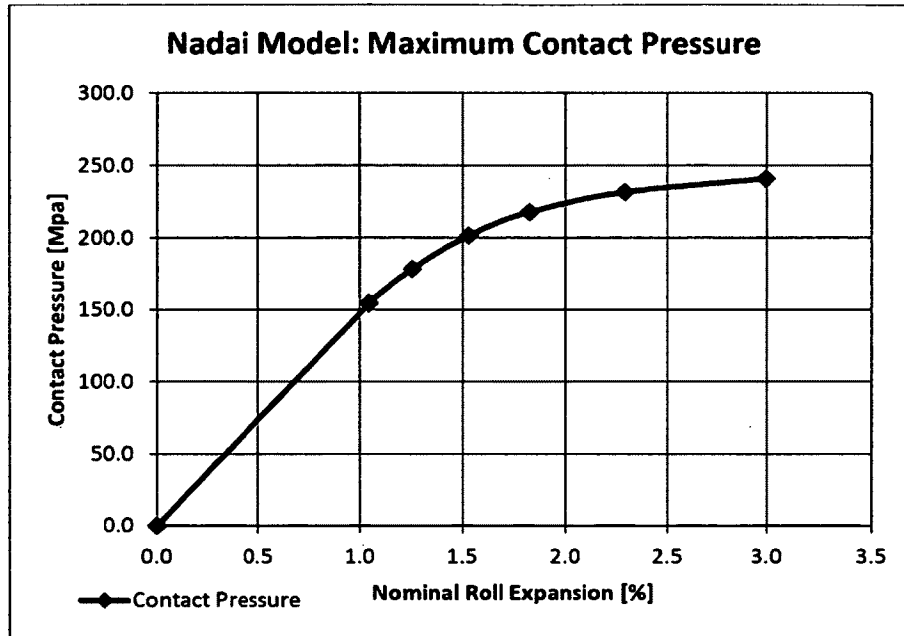


Figure A-1: Predicted contact pressure with pressure applied on inside surface

Using the results from above, the residual contact pressure can be obtained:

The radial stresses at the outer and inner surfaces are related by Equation A1-11,

$$\frac{\sigma_1}{\sigma_2} = \frac{\left\{ 2\nu_2 - 1 - 2\nu + \frac{2E}{E'}(1 + \nu') \right\} p_2}{(2\nu_1 - 1)} \quad (\text{A1-11})$$

And at  $r=r_1$ :

$$\sigma_r = -p_1^* + \sigma_1 = 0$$

And at  $r=r_2$ :

$$\sigma_r = -p_2^* + \sigma_2$$

So: for the values of  $\nu_1, \nu_2, \nu, \nu', E, E'$  used previously,

$$p_{2 \text{ res}} = p_2^* - 0.84p_1^*$$

And subtracting the elastic stress of spring-back gives the interface pressure gives Figure A-2.

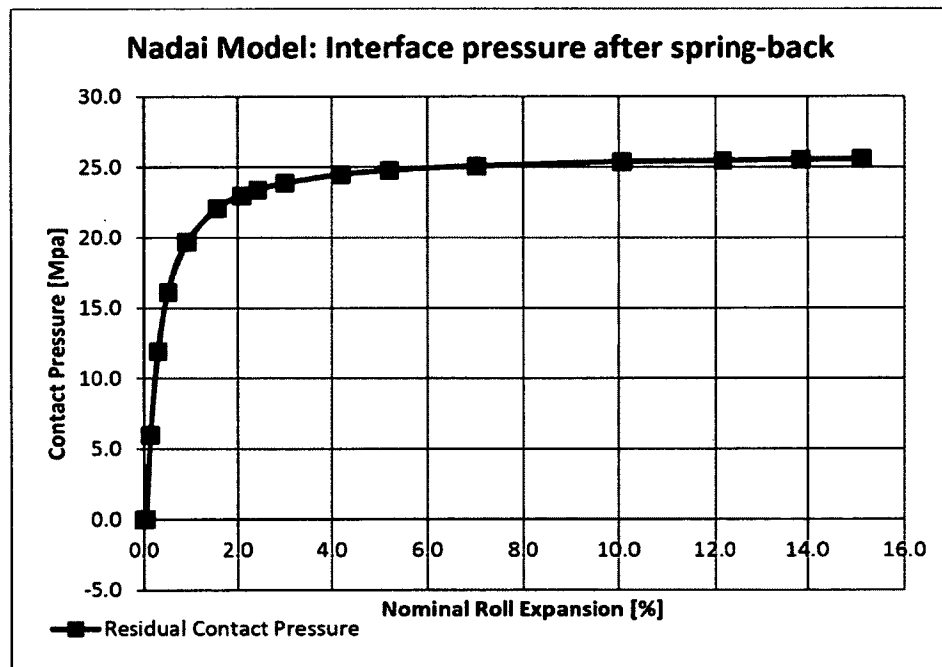


Figure A-2: Interface pressure after spring-back

A particularly interesting feature of the Nadai model is the shape of the function of interface pressure as a function of % wall reduction. More specifically, the model predicts rapidly increasing interface pressure with % wall reduction for low expansions, followed by a transition zone and a flattening curve where very little increase in pressure accompanies increasing wall reduction. This is in agreement with the Yorkell [13] assertion that the maximum interface pressure cannot be increased by further expansion beyond the point where the plastic zone in the tubesheet is equal to 1.75 times the inside

radius of the tube. This is also consistent with phase 5 of rolling, as described in Section 2.1.

### Appendix B : Implementation of Interface Pressure Calculation

An analytical solution to the loading case of a uniform load applied to the outside diameter of a short tube is presented in Table 13.2 Chapter 13 of [2].

The calculation was implemented using the GoalSeek function of Microsoft® Excel® 2007 to numerically solve for the applied pressure. The tables below present the formulas input, and a sample calculation for a given measured deflection.

#### Implementation Formulae

$$y = \frac{qR^2}{tE} \left( \frac{C_4 C_{a2} - C_3 C_{a2} - C_3 C_{a3}}{4C_{11}} - (x-a)^0 + (x-a)^0 \cosh(\lambda(x-a)) \cos(\lambda(x-a)) \right) \quad (\text{B1-1})$$

$$C_4 = \cosh \lambda l \sin \lambda l - \sinh \lambda l \cos \lambda l \quad (\text{B1-2})$$

$$C_{a2} = \cosh \lambda(l-a) \sin \lambda(l-a) - \sinh \lambda(l-a) \cos \lambda(l-a) \quad (\text{B1-2})$$

$$C_3 = \sinh \lambda l \sin \lambda l \quad (\text{B1-2})$$

$$C_{11} = \sinh^2 \lambda l - \sin^2 \lambda l \quad (\text{B1-2})$$

$$\lambda = \left[ \frac{3(1-\nu^2)}{R^2 t^2} \right]^{\frac{1}{4}} \quad (\text{B1-2})$$

where:

- $q$  is the interface pressure
- $R$  is the tube radius
- $T$  is the tube wall thickness
- $x$  is the axial coordinate
- $E$  is the Young's modulus
- $N$  is the Poisson ratio
- $a$  is the length of the segment over which the pressure is applied (see Figure 3-1)

A screenshot of the implementation of the calculation is shown in Figure B-1, and a sample calculation in Figure B-2.

	A	B	C	D	E
1	From: Roark's Formulas to Stress and Strain 7e				
2	Warren C. Young, Richard G Budynas				
3	McGraw Hill 2002				
4	Chapt 13, Table 13.2				
5					
6					
7	a	[mm]	20		
8	l	[mm]	50		
9	q	[Mpa]	=6.70691187879742		
10	R	[mm]	160		mean radius
11	t	[mm]	10		
12	nu		0.16		UNS C85400
13	E	[Mpa]	210000		UNS C85400
14					
15	RA		=D10/D11		
16	D		=D13*D11^3/(12*(1-D12^2))		
17	lambda		=(3*(1-D12^2)/(D10^2*D11^2))^0.25		
18	lambda'		=D17/D8		
19	lambda'*(1-a)		=D17*(D8/D7)		
20					
21	C11		=SINH(D18)^2*SIN(D18)^2		
22	C2		=COSH(D18)*SIN(D18)+SINH(D18)*COS(D18)		
23	C3		=SINH(D18)*SIN(D18)		
24	C4		=COSH(D18)*SIN(D18)-SINH(D18)*COS(D18)		
25	Ca2		=COSH(D18)*SIN(D18)+SINH(D18)*COS(D18)		
26	Ca3		=SINH(D18)*SIN(D18)		
27	PaA		=D9/(2*D16*D17^3)*(D22*D26-D23*D25)/D21		
28	YA		=D9/(4*D16*D17^4)*(2*D23*D26-D24*D25)/D21		
29					
30			A1 location	B2 location	
31	x		=D31*D517		=E31*D517
32	lambda*x		=D31*D517		=E31*D517
33	F1		=COSH(D32)*COS(D32)		=COSH(E32)*COS(E32)
34	F2		=COSH(KF24)*SIN(D32)+SINH(D32)*COS(D32)		=COSH(KG24)*SIN(E32)+SINH(E32)*COS(E32)
35	alpha=0		=IF(D31>D517,1,0)		=IF(E31>D517,1,0)
36	alpha=1		=D35*D31		=E35*E31
37	Fa1		=D35*COSH(D517*D36)*COS(D517*D36)		=E35*COSH(D517*E36)*COS(D517*E36)
38	Fa5		=D35*D37		=E35*E37
39	Lty		=D519/(4*D516*D517^4)*D38		=D519/(4*D516*D517^4)*E38
40	y		=D528*D33+D527/(2*D517)*D34+D39		=D528*E33+D527/(2*D517)*E34+E39
41					
42					
43					
44	for Goalseek				
45	Measured deflection				
46	delta deflection				
47					
48					

Figure B-1: Implementation of interface pressure calculation in Microsoft Excel®

## Sample Calculation

From: Roark's Formulas for Stress and Strain 7e  
 Warren C. Young; Richard G Budynas  
 McGraw Hill 2002  
 Chapt 13. Table 13.2

a	[mm]	40	
l	[mm]	90	
q	[Mpa]	-67069119	
R	[mm]	160	mean radius
t	[mm]	10	
nu		0.316	UNS C95400
E	[Mpa]	1.10E+05	UNS C95400

R/t	16
D	10183555.82
lambda	0.032047807
lambda <sup>1</sup>	2.884302654
lambda*(l-a)	1.602390363

C11	79.45877895
C2	-6.340656535
C3	2.269177822
C4	10.9074577
Ca2	2.506625059
Ca3	2.980547217
Psi A	0.002616665
YA	-0.032485407

	A1 location	B2 location
x	53	65
lambda * x	1.698533785	2.083107472
F1	-0.359806363	-1.998498122
F2	0.655352563	-1.065834285
<x-a> <sup>0</sup>	1	1
<x-a> <sup>1</sup>	53	65
Fa1	-0.359806363	-1.998498122
Fa5	1.359806363	2.998498122
Lty	0.212249634	0.468029968
y	0.25069246	0.489439956

for Goalseek	
Measured deflection	0.25
delta deflection	

Figure B-2: Sample calculation of interface pressure

**Appendix C : Strain Gauge Locations**

## C.1 Tube 10mm-8.3%WR

10mm-8.3%WR									
ID	Gauge #	Direction (nominal)	Angular Orientation	Distance from Outboard Edge	Distance from Cut Edge	Gauge Type [Vishay MM]	Gauge Factor [+0.5%]	Item Code	Code
A1-ID-ax-01	2	axial	90	42.2	9.3	CEA-13-062UW-350	2.17	3101	182011
A1-ID-ho-02	8	hoop	0	42.2	19.7	CEA-13-062UW-350	2.17	3101	182011
A1-ID-ho-03	5	hoop	0	42.2	39.2	CEA-13-062UW-350	2.17	3101	182011
A1-OD-ax-03	15	axial	90	43	11.5	CEA-13-062UW-350	2.17	3101	201620
A1-OD-ho-01	11	hoop	0	43	12.0	CEA-13-062UW-350	2.17	3101	201620
A1-OD-ho-02	12	hoop	0	43	23.1	CEA-13-062UW-350	2.17	3101	201620
B2-ID-ax-02	4	axial	90	28.7	19.7	CEA-13-062UW-350	2.17	3101	182011
B2-ID-ho-01	1	hoop	0	28.7	9.3	CEA-13-062UW-350	2.17	3101	182011
B2-ID-ho-03	6	hoop	0	28.7	39.2	CEA-13-062UW-350	2.17	3101	182011
B2-ID-ho-04	7	hoop	0	28.7	10.8	CEA-13-062UW-350	2.17	3101	182011
B2-OD-ax-03	14	axial	90	28.3	11.5	CEA-13-062UW-350	2.17	3101	182417
B2-OD-ho-01	9	hoop	0	28.3	12.0	CEA-13-062UW-350	2.17	3101	201620
B2-OD-ho-02	10	hoop	0	28.3	23.13	CEA-13-062UW-350	2.17	3101	201620
C3-ID-ax-01	3	axial	90	18.2	9.28	CEA-13-062UW-350	2.17	3101	182011
C3-OD-ax-03	13	axial	90	17.7	11.45	CEA-13-062UW-350	2.17	3101	182417

\* See installation of photos for orientation.

## C.2 Tube 10mm-6.8%WR

10mm-6.8%WR									
ID	Gauge #	Direction (nominal)	Angular Orientation	Distance from Outboard Edge	Distance from Cut Edge	Gauge Type [Vishay MM]	Gauge Factor [+0.5%]	Item Code	Code
A1-ID-45	5	45 deg*	45	37.5	18.4	CEA-13-062UW-350	2.17	3101	202316
A1-ID-ax	4	axial	90	37.5	7.8	CEA-13-062UW-350	2.17	3101	202316
A1-ID-ho	1	hoop	0	37.5	8.8	CEA-13-062UW-350	2.17	3101	202316
A1-OD-45	12	45 deg*	225	37.5	21.4	CEA-13-062UW-350	2.17	3101	201620
A1-OD-ax	11	axial	90	37.5	10.3	CEA-13-062UW-350	2.17	3101	201620
A1-OD-ho	9	hoop	0	37.5	9.7	CEA-13-062UW-350	2.17	3101	203314
B2-ID-45	3	45 deg*	225	25	18.3	CEA-13-062UW-350	2.17	3101	202316
B2-ID-ax	2	axial	90	25	8.8	CEA-13-062UW-350	2.17	3101	202316
B2-ID-ho	6	hoop	0	25	7.8	CEA-13-062UW-350	2.17	3101	203314
B2-OD-45	8	45 deg*	45	25	20.4	CEA-13-062UW-350	2.17	3101	203314
B2-OD-ax	7	axial	90	25	9.7	CEA-13-062UW-350	2.17	3101	203314
B2-OD-ho	10	hoop	0	25	10.3	CEA-13-062UW-350	2.17	3101	203314

\* See installation of photos for orientation.

## C.3 Tube 10mm-5.0%WR

10mm-5.0%WR									
ID	gauge #	Direction (nominal)	Angular Orientation	Distance from Outboard Edge	Distance from Cut Edge	Gauge Type [Vishay MM]	Gauge Factor [+0.5%]	Item Code	Code
A1-ID-45	3	45 deg*	45	36.7	17.4	CEA-13-062UW-	2.17	3101	201620
A1-ID-ax	2	axial	90	36.7	7.7	CEA-13-062UW-	2.17	3101	201620
A1-ID-ho	1	hoop	0	36.7	9.7	CEA-13-062UW-	2.17	3101	201620
A1-OD-45	9	45 deg*	45	37.5	18.8	CEA-13-062UW-	2.17	3101	201620
A1-OD-ax	8	axial	90	37.5	10.1	CEA-13-062UW-	2.17	3101	182415
A1-OD-ho	7	hoop	0	37.5	8.8	CEA-13-062UW-	2.17	3101	182415
B2-ID-45	6	45 deg*	225	24.8	17.4	CEA-13-062UW-	2.17	3101	182415
B2-ID-ax	5	axial	90	24.8	9.7	CEA-13-062UW-	2.17	3101	182415
B2-ID-ho	4	hoop	0	24.8	7.7	CEA-13-062UW-	2.17	3101	182415
B2-OD-45	12	45 deg*	45	24.6	19.2	CEA-13-062UW-	2.17	3101	203717
B2-OD-ax	11	axial	90	24.6	8.8	CEA-13-062UW-	2.17	3101	203717
B2-OD-ho	10	hoop	0	24.6	10.1	CEA-13-062UW-	2.17	3101	203717

\* See installation of photos for orientation.

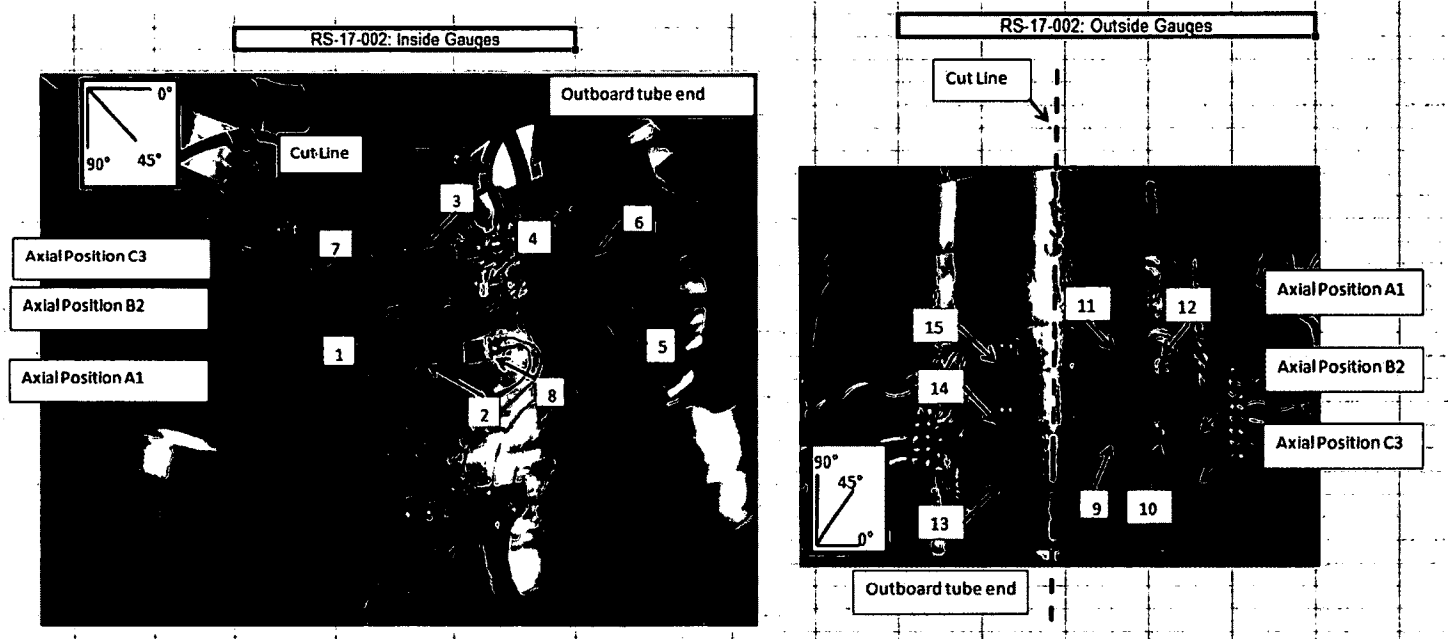
**C.4 Tube 6mm-7.9%WR**

6mm-7.9%WR									
ID	gauge #	Direction (nominal)	Angular Orientation	Distance from Outboard Edge	Distance from Cut Edge	Gauge Type [Vishay MM]	Gauge Factor [+0.5%]	Item Code	Code
A1-ID-45	3	45 deg*	45	38.0	16.6	CEA-13-062UW-350	2.170	3101	203717
A1-ID-ax	2	axial	90	38.0	7.0	CEA-13-062UW-350	2.170	3101	203717
A1-ID-ho	1	hoop	0	38.0	7.0	CEA-13-062UW-350	2.170	3101	203717
A1-OD-45	9	45 deg*	135	37.3	14.2	CEA-13-062UW-350	2.170	3101	203317
A1-OD-ax	8	axial	90	37.3	5.9	CEA-13-062UW-350	2.170	3101	203317
A1-OD-ho	7	hoop	0	37.3	7.1	CEA-13-062UW-350	2.170	3101	203317
B2-ID-45	5	45 deg*	135	25.6	7.0	CEA-13-062UW-350	2.170	3101	203717
B2-ID-ax	6	axial	90	25.6	16.9	CEA-13-062UW-350	2.170	3101	203717
B2-ID-ho	4	hoop	0	25.6	7.0	CEA-13-062UW-350	2.170	3101	203717
B2-OD-45	12	45 deg*	135	25.2	16.6	CEA-13-062UW-350	2.170	3101	203317
B2-OD-ax	11	axial	90	25.2	7.1	CEA-13-062UW-350	2.170	3101	203317
B2-OD-ho	10	hoop	0	25.2	5.9	CEA-13-062UW-350	2.170	3101	203317
C3-OD-ax	13	axial	90	65.16	7.14	CEA-13-062UW-350	2.170	3101	203317

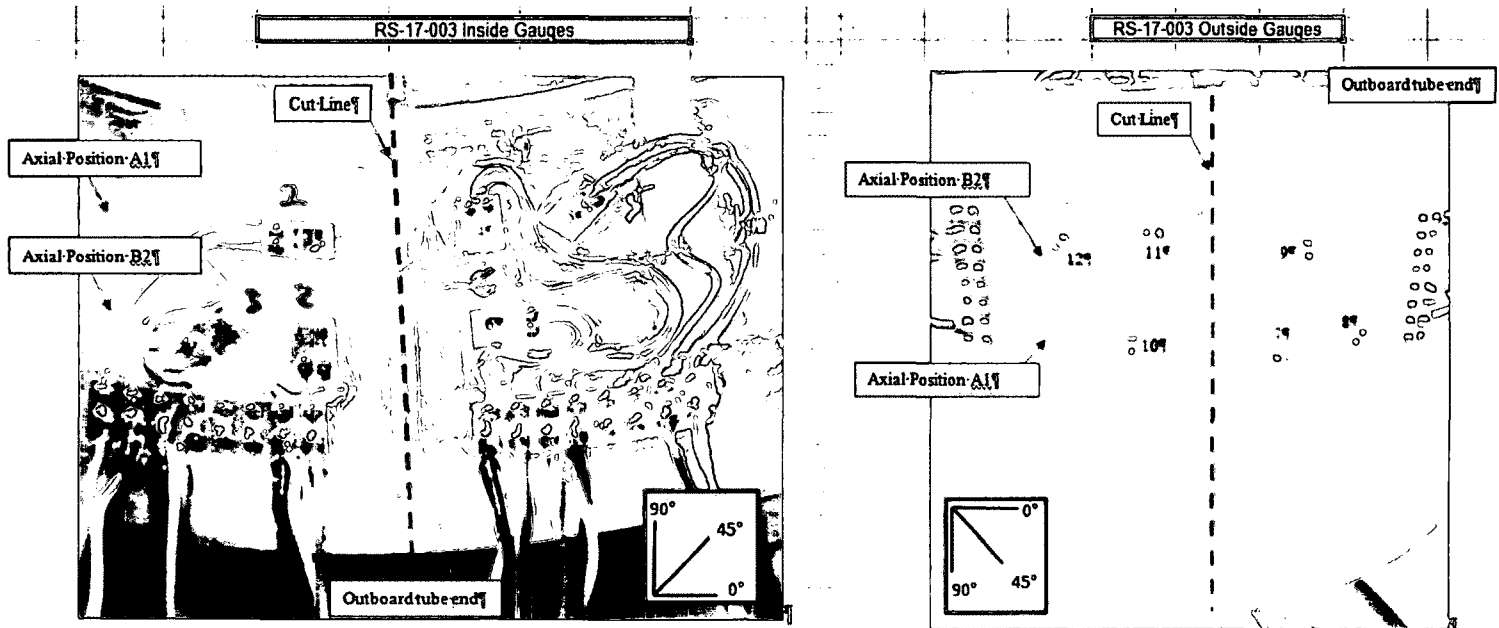
\* See installation of photos for orientation.

**Appendix D : Annotated Strain Gauge Installation Photos**

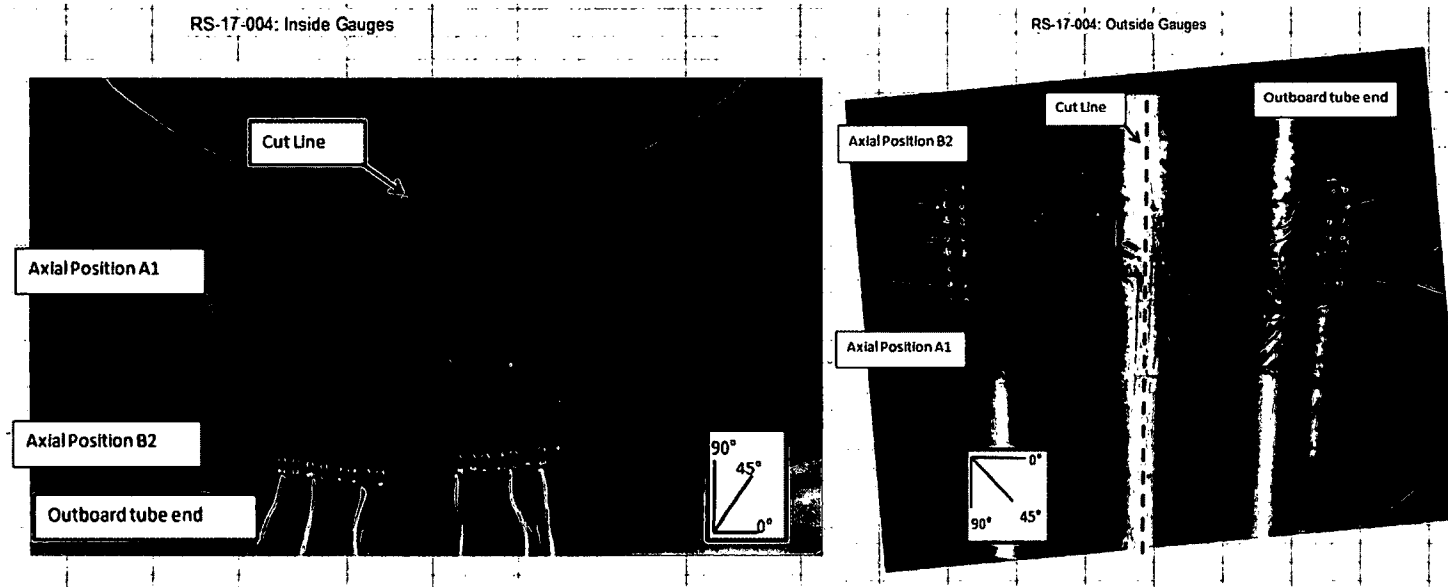
D.1 Tube 10mm-8.3%WR



D.2 Tube 10mm-6.8%WR



### D.3 Tube 10mm-5.0%WR



## D.4 Tube 6mm-7.9%WR

